University of Southampton

Faculty of Engineering and Physical Sciences

Chemistry

Operando Detection of Gas Evolution from Lithium-Ion Batteries

by

Liam Lu

Supervisors – Prof. Nuria Garcia-Araez & Prof. Phillip Bartlett

Thesis for the degree of Doctor of Philosophy

January 2025

University of Southampton

Abstract

Faculty of Engineering and Physical Sciences

Chemistry

Thesis for the degree of Doctor of Philosophy

Operando Detection of Gas Evolution from Lithium-Ion Batteries

by

Liam Lu

The aim of this study was to investigate commercially relevant lithium-ion battery materials, using operando pressure measurements in conjunction with conventional electrochemical analysis techniques. Quantifying gas evolution provides important insights about the reactions taking place during the operation of lithium-ion battery materials; for instance, the reaction of SEI formation on graphite, which is critical to achieve good battery performance, involves gas evolution. This thesis focused on the study of the gas evolution properties of a high-performance graphite anode and the effect of the presence of electrolyte additives and dissolved transition metals.

Electrolyte additives are used in commercial lithium-ion batteries to drastically improve their performance, thus understanding their effect on the gas evolution properties of graphite anodes is important to elucidate their effect on the reactions of SEI formation. Dissolved transition metals are produced as a result of degradation of cathode materials, and understanding their effect on the battery gas evolution properties of the graphite anode is important to unravel crosstalk effects that lead to exacerbated battery degradation.

Firstly, galvanostatic cell cycling was employed to evaluate the electrochemical performance of industry standard electrode materials and electrolyte additives. From these experiments, it was then possible to see the electrochemical impact from varying the cell environment, such as differences in cell capacity and efficiency when changing electrode production methods or the introduction of various electrolyte additives.

Secondly, a highly sensitive operando pressure measurement technique, developed from adapted Swagelok union cell parts, was used to monitor gas evolution events during the electrochemical cycling of cells. This technique, when used in conjunction with Galvanostatic cycling, reveals clear impacts of additives and transition metals on key gassing events within lithium-ion batteries.

The clear impact of electrolyte additives and transition metal dissolution was observed in both the electrochemical performance and gas evolution volume. Transition metal dissolution predictably decreased electrochemical performance whilst increasing gas evolution volume, whilst the presence of commercially relevant electrolyte additives such as Vinylene Carbonate exhibited its clear ability to suppress gassing reactions and improve electrochemical performance.

Table of Contents

Table of Contents ..... **iii**

Research Thesis: Declaration of Authorship ..... **vi**

Acknowledgements ..... **viii**

Abbreviations and Units ..... **ix**

Chapter 1 Introduction **2**

1.1 Brief Look into Lithium-Ion Batteries 2

1.2 Electrode Materials 3

1.2.1 Cathode Materials 3

1.2.1.1 $LiFePO_4$ (LFP) 3

1.2.1.2 $LiCoO_2$ (LCO) and $Li(Ni_xMn_yCo_z)O_2$ (NMC) 5

1.2.2 Anode Materials 7

1.2.2.1 Lithium Metal 7

1.2.2.2 Graphite 8

1.3 Gas Evolution 11

1.3.1 Gas Analysis Methods 11

1.3.2 Gas evolution at Graphite Electrode 12

1.3.3 Effect of Transition Metal Dissolution on Gas Evolution 14

1.4 Improvement Strategies 15

1.4.1 Additives 15

1.4.1.1 Vinylene Carbonate (VC) 16

1.4.1.2 1,3,2-dioxathiolane-2,2-dioxide (DTD) and VC Combination 18

1.4.1.3 $LiPO_2F_2$ (LFO) 18

1.5 Thesis Aims and Objectives 19

Chapter 2 Methodology and Optimisations **21**

2.1 Context 21

2.2 Methodology 21

2.2.1 Baseline Swagelok Assembly 21

2.2.2 Electrolyte Preparation 23
2.2.3 Pressure Measurement Adaptations 24
2.2.4 Electrode Production 24
2.2.5 Electrochemical Cycling and Analysis 26
2.2.5.1 Galvanostatic Cycling with Potential Limitation (GCPL) 26
2.2.5.2 Electrochemical Analysis 29
2.2.6 Additional Pressure Measurement Procedures 33
2.2.6.1 Headspace Volumes 33
2.2.6.2 Normalisation of data 36
2.2.6.3 Leak Testing 38
2.3 Methodology Optimisations and Adaptations 40
2.3.1 Addressing Poor Electrochemical Performance 41
2.3.2 Addressing Slow Gas Transfer 47
2.3.3 Summary of Optimisations and Adaptations 53

Chapter 3 Investigation Into the Effects of Dissolved Transition Metals on Gas Evolution Properties of Graphite Electrodes 54

3.1 Context 54
3.2 Gas Evolution Behaviour in Baseline LP57 Electrolyte 54
3.3 Gas Evolution Behaviour with the Introduction of Nickel Ions 59
3.4 Gas Evolution Behaviour with the Introduction of Manganese Ions 64
3.5 Gas Evolution Behaviour with the Introduction of Cobalt Ions 69
3.6 Comparison of Gas Evolution Behaviour Transition Metals Dissolution 73
3.7 Summary 78

Chapter 4 Investigation Into the Effects of Electrolyte Additives on Gas Evolution Properties of Graphite Electrodes 80

4.1 Context 80
4.2 Gas Evolution Behaviour with the Introduction of VC Additive 80
4.3 Gas Evolution Behaviour with the Introduction of LFO Additive 84
4.4 Gas Evolution Behaviour with the Introduction of DTD Additive 88
4.5 Gas Evolution Behaviour with the Introduction of VC and DTD Additives 91

4.6 Comparison of Gas Evolution Behaviour of the Electrolyte Additives 95
4.7 Summary 100

Chapter 5 Investigation Into the Effects of Electrolyte Additives with the Co-Addition of Manganese Ions on Gas Evolution Properties of Graphite Electrodes ...102

5.1 Context 102
5.2 Gas Evolution Behaviour with the Introduction of VC Additive with the Co-Addition of Manganese Ions 103
5.3 Gas Evolution Behaviour with the Introduction of LFO Additive with the Co-Addition of Manganese Ions 107
5.4 Gas Evolution Behaviour with the Introduction of DTD + VC Additives with the Co-Addition of Manganese Ions 111
5.5 Comparison of Gas Evolution Behaviour of the Electrolyte Additives with the Co-Addition of Manganese Ions 116
5.6 Summary 122

Chapter 6 Project Conclusion and Further Work 124

Appendix 126

Temperature correction of operando pressure measurements 126
Headspace volume calculations 126
Electrolyte formulation 127

Research Thesis: Declaration of Authorship

Print name: Liam Lu

Title of thesis: Operando Detection of Gas Evolution from Lithium-Ion Batteries

I declare that this thesis and the work presented in it are my own and has been generated by me as the result of my own original research.

I confirm that:

1. This work was done wholly or mainly while in candidature for a research degree at this University.
2. Where any part of this thesis has previously been submitted for a degree or any other qualification at this University or any other institution, this has been clearly stated;
3. Where I have consulted the published work of others, this is always clearly attributed;
4. Where I have quoted from the work of others, the source is always given. With the exception of such quotations, this thesis is entirely my own work;
5. I have acknowledged all main sources of help;
6. Where the thesis is based on work done by myself jointly with others, I have made clear exactly what was done by others and what I have contributed myself;
7. None of this work has been published before submission.

Signature: Date: 24/03/2024

Acknowledgements

First and foremost, I would like to express my sincerest gratitude to my academic supervisor, Prof. Nuria Garcia-Araez, for providing unwavering support and guidance throughout my PhD. Conducting research as part of the Garcia-Araez research group has been a phenomenal journey, with many ups and downs, however it has ultimately allowed me to pursue my dream of becoming a scientist, something which I will cherish forever.

Additionally, I would like to thank the numerous members of the Garcia-Araez group, both past and present, for providing a wealth of knowledge in both the scientific field and in the PhD experience. Members that I would like to extend special thanks to are Dr. Niamh Ryall, Dr. Ben Rowden, Dr. Vivek Padmanabhan, Dr. John Lampkin, Dr. Henry Li, Dr. Sara Perez-Rodriguez, Dr. Liam Furness Dr. Sam Fitch, Dr. Min Zhang, Dr. Antonia Kotronia, Dr. Mark Stockham, and Myth Maund, all have which have contributed to enriching my time in Southampton.

Furthermore, I would like to acknowledge the institutions that made this project possible, the University of Southampton, the Engineering and Physical Sciences Research Council (EPSRC), and The Faraday Institution for funding my PhD. I am also grateful to Fran Long for providing exceptional training through the Faraday Training Program, it was an absolute privilege to be part of that experience. Another acknowledgement to my WMG internship supervisors, Prof. Melanie Loveridge, Prof. Louis Piper, Dr. Eleni Fiamegkou, and Dr. Nickil Shah, for giving me a glimpse of cutting-edge industrial research.

I would like to express my gratitude for my friends and family, all of which have helped me make it through the last 8 and a half years. Special thanks to my parents, who have consistently supported me through all the tough times. I am grateful for the University of Southampton Ultimate Frisbee Society, who have provided some of the best memories of my life so far and allowed me to forge lifelong friendships. Being part of the club has undoubtedly made me who I am today.

Finally, I dedicate my greatest thanks to my partner, Bethany Jeffrey, who throughout the course of my PhD, has undoubtedly been my greatest fan, providing me with support at every possible opportunity. I could not have done it without you.

Abbreviations and Units

CE	Counter electrode
DEMS	Differential electrochemical mass spectrometry
DTD	1,3,2-dioxathiolane-2,2-dioxide
EC	Ethylene carbonate
EMC	Ethylene methyl carbonate
GC-MS	Gas chromatography mass spectrometry
GCPL	Galvanostatic cycling with potential limitation
GF-F	Glass fibre separator
LCO	Lithium cobalt oxide
LEDC	Lithium ethylene decarbonate
LFO	$LiPO_2F_2$
LFP	Lithium iron phosphate
LP57	1M LiPF6 in ethylene carbonate (EC) and ethylene methyl carbonate (EMC) with EC: EMC weight ratio of 3:7
LTO	Lithium titanium oxide
NMC	Lithium nickel manganese oxide
NMP	1-Methyl-2-pyrrolidone
OCV	Open circuit voltage
OEMS	Online electrochemical mass spectrometry
PVDF	polyvinylidene fluoride
SEI	Solid interphase layer
SHE	Standard hydrogen electrode
TFSI	bis(trifluoromethanesulfonyl)imide
VC	Vinylene carbonate
WE	Working electrod

Chapter 1 Introduction

1.1 Brief Look into Lithium-Ion Batteries

Lithium-ion batteries, since their commercial debut in the early 1990s[1], have become increasingly integrated into everyday appliances. This technology has become an absolute necessity in numerous applications such as laptops, mobile phones, and electric cars; it is clear that the lithium-ion battery field has great potential for further implementation in society, and thus has garnered interest amongst academic and industrial organisations worldwide.

At the time of writing, lithium-ion battery technology is currently the energy storage choice for many commercial electric vehicles; several attributes have fast tracked lithium-ion batteries popularity when compared to similar energy storage technologies. Properties such as higher energy densities, low self-discharge rate, great cycling ability and high operating voltages all have contributed to its commercial success [2, 3]. These characteristics are especially important when considering their impact in electric vehicles, where they are directly related to key specifications such as driving range, battery lifetime and charging speeds.

Lithium-ion batteries operate through a lithium intercalation mechanism as their electrochemical energy storage reaction; to initiate charging, a positive current is imposed on the battery causing lithium ions to move from the cathode material to the anode material through the electrolyte. And then upon discharging, a spontaneous negative current occurs due to the thermodynamically favoured movement of lithium ions from the anode back to the cathode. An example of the lithium intercalation mechanism can be seen in Figure 1.

Although many cell components govern the overall electrochemical performance of the battery, the key fields of interest lie within the cathode, anode, and electrolyte. For example, the cathode is typically known to be the limiting factor with respect to the specific capacity of the cell when compared to the anode [4-6], thus finding the ideal cathode candidate is imperative to increasing electric vehicle driving ranges. However despite this, the anode choice is still crucial in determining the cells performance such as its long term aging and safety of the cell [7, 8]. Furthermore, the choice of electrolyte is vital when evaluating the safety of the battery as it is the most flammable part of the system [9] and therefore will always be a key consideration when developing a cell. The importance of the electrolyte is further emphasised when considering their significant impact on the electrochemical performance of the electrodes, where the choice of electrolyte can cause various outcomes such as degradation of the active material, unwanted side reactions, or a noticeable increase in stability. Finally, the properties of the electrolyte can be

further enhanced with the use of electrolyte additives [10], making the electrolyte formulation extremely important.

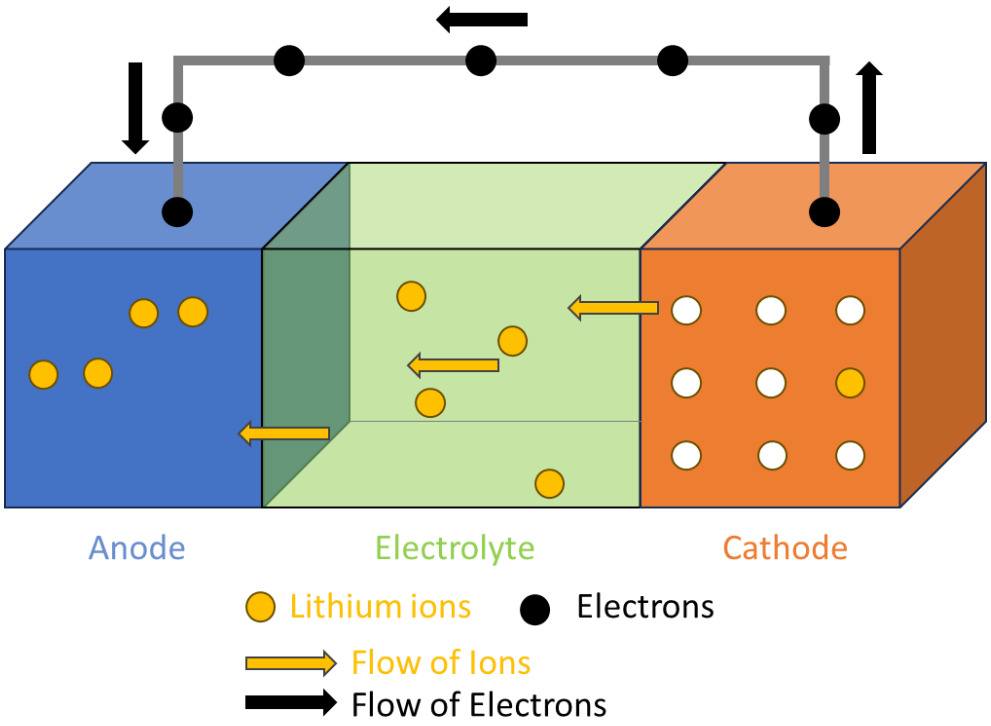

Figure 1 – Schematic showing lithium intercalation mechanism during charging of a lithium-ion battery, where the flow of electrons and lithium ions are from the cathode to the anode.

The complexity of lithium-ion battery systems is not just limited to the individual components themselves; interactions between the cathode, anode and electrolyte can also lead to additional layers of consequences. For example, certain cathodes can degrade over time, causing transition metal dissolution into the electrolyte, which ultimately migrates towards the anode, undergoing further unwanted side reactions and impacting the performance of the cell [11]. Investigating these events can be difficult due to their complex nature, however this chapter will provide a brief overview and explain key factors relevant to the project.

1.2 Electrode Materials

1.2.1 Cathode Materials

1.2.1.1 $LiFePO_4$ (LFP)

$LiFePO_4$ (LFP) was first identified as a viable cathode material by J.B. Goodenough in 1997 [12] and was quickly found to be a promising cathode as the material was cheap, environmentally

friendly and stable. And most importantly, LFP has been frequently described in literature [13-15] as presently one of the safest lithium-ion cathodes, making it highly desirable candidate for energy storage use. As a result of these advantages, the use of LFP can be seen in many applications such as solar energy storage systems, electric vehicles, and uninterrupted power systems.

It is possible for LFP to be cheap and environmentally friendly as iron is a naturally abundant, easy to obtain and significantly less toxic [15] in comparison to other common cathode metals such as cobalt (which has geographical, ethical and extraction issues associated). Furthermore, its robust nature can be attributed to the strong P-O bonds in the structure that allow the material to be durable during cycling, thus improving the safety and stability of the overall battery [15-17]. All this paired with a relatively competitive theoretical specific capacity of 170 $mAhg^{-1}$ make LFP a highly promising cathode material [3, 18].

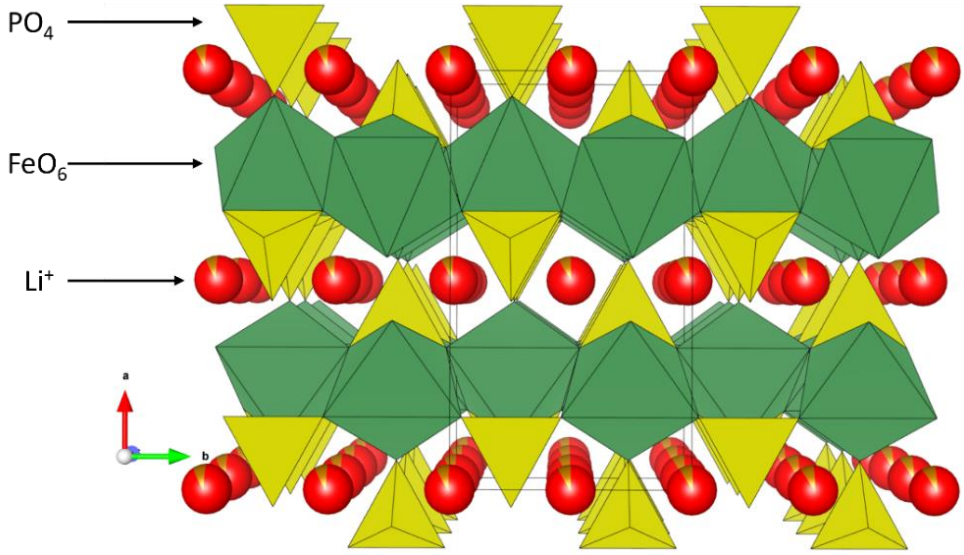

Figure 2 - LFP crystal structure, showing clear one-dimensional channels for lithium ions. Figure was produced using VESTA 3 with the structure obtained from Inorganic Crystal Structure Database (ICSD).

LFP belongs to the olivine family, where its crystal structure is shown in Figure 2. An important attribute to note for LFP is that the lithium-ion transport during charging and discharging occurs only in one-dimensional channels; in the event of structural defects or impurities, these channels can become blocked and therefore impede the movement of the lithium ions which results in slower kinetics during charging and discharging, this leads to LFP possessing poor ionic conductivity qualities in comparison to other materials [19]. In addition to this, LFP has been shown to also possess low electronic conductivity, requiring the addition of conductive materials and changes to conventional synthesis routes to ensure good performance [20, 21].

Another interesting feature is the potential profile of LFP, which typically remains flat during the charge/discharge (~3.45 V vs Li/Li^+). This can be seen as undesirable as it becomes very difficult to determine the state of charge of the battery compared to a material whose potential profile slope [22] i.e. if a material has a unique potential for each state of charge, then it is very easy to determine the state of charge is by simply examining the electrode potentials. In the case of LFP, a more advanced battery management system to determine the state of charge of the battery is required.

Despite the disadvantages, LFP can be used in many other applications where safety and stability are the priority. Additionally, LFP is highly advantageous in research as a stable electrode to examine more reactive materials. Finally, due to the moderate potential of operation of LFP, well within the stability window of standard battery electrolytes, it has been shown that it does not partake in gas evolution/consumption reactions [6, 23]. This allows the use of LFP as a valuable control electrode when conducting gas analysis experiments, as any gas evolution that may occur can be sure to not originate from the LFP but rather the other elements within the cell.

1.2.1.2 $LiCoO_2$ (LCO) and $Li(Ni_xMn_yCo_z)O_2$ (NMC)

In addition to the discovery of LFP, J.B. Goodenough was also responsible for the discovery of lithium cobalt oxide (LCO), a layered transition metal oxide cathode material [24, 25], which ultimately led to the first commercial rechargeable lithium-ion battery by Sony Corporation that utilised LCO as the cathode. Since then, further work with LCO has led to the partial substitution of the cobalt transition metal with manganese and nickel [26], giving rise to a new family of layered cathode materials, $Li(Ni_xMn_yCo_z)O_2$ (where X+Y+Z = 1) or NMC, shown in Figure 3.

Due to the scarcity of cobalt, combined with various political and ethical issues surrounding cobalt mining [27, 28], cathodes with low cobalt content have become highly desired, making NMC cathodes such as $Li(Ni_{1/3}Mn_{1/3}Co_{1/3})O_2$ or NMC111 popular for commercial uses such as electric vehicles [29, 30].

The oxidation states of the transition metals within fully lithiated NMC111 are: Ni^{2+}, Co^{3+}, and Mn^{4+} where during charging, the metal ions are oxidised in the order of Ni^{2+} to Ni^{3+}, Ni^{3+} to Ni^{4+}, Co^{3+} to Co^{4+} whilst Mn stays at the same oxidation state throughout [31, 32].

Ni^{2+}/Ni^{3+} and/or Ni^{3+}/Ni^{4+} redox couples thus contribute the most to the reversible capacity [33]. Cobalt allows higher rate capability and increases electronic conductivity by stabilising the overall material structure [34], however as mentioned before due to its political and ethical disadvantages, it is undesirable to increase cobalt content. Manganese also has the role of stability and does not take part in the electrochemical processes, which consequently makes it

useful in stabilising the local structure. Increasing manganese content has shown to increase thermal and electrochemical stability of the compound [35-37].

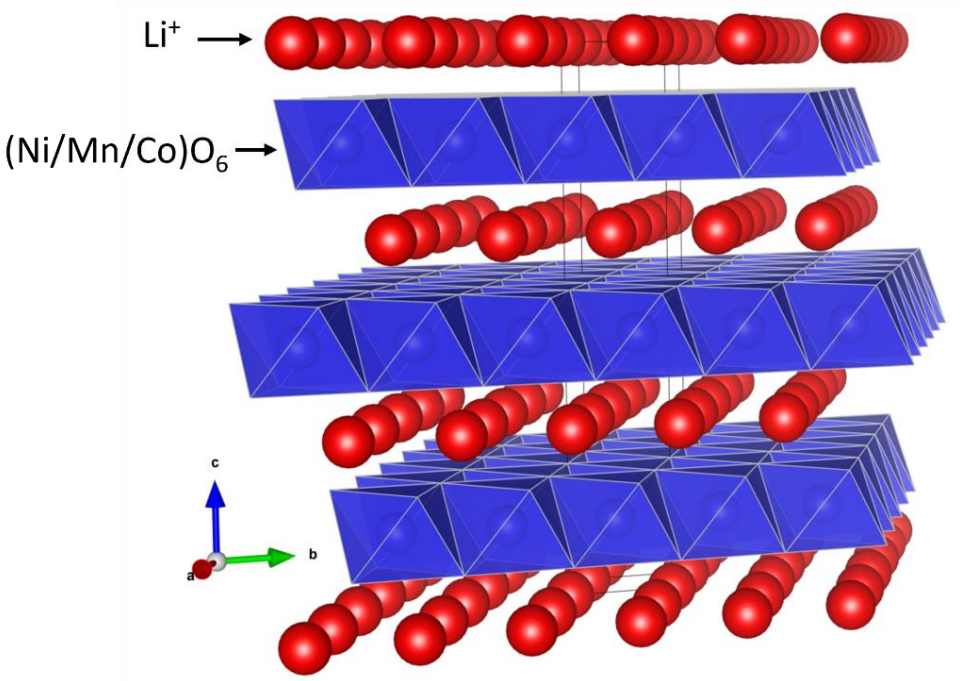

Figure 3 - NMC crystal structure, two dimensional layers for lithium ions. Figure was produced using VESTA 3 with the structure obtained from Inorganic Crystal Structure Database (ICSD).

The electrochemical performance of NMCs is strongly related to its transition metal composition [38]. Within literature, it has been shown that higher nickel contents leads to higher specific capacity, however suffers from stability issues and poor capacity retention, whereas high manganese content shows opposite effects [29].

Nickel rich NMCs such as $Li(Ni_{0.8}Mn_{0.1}Co_{0.1})O_2$ or NMC811 are already utilised in commercial applications such as in electric vehicles due to their decreased cobalt content compared to other cathode materials i.e., NMC111 and LCO [39]. Paired with their lower costs and toxicity, it is clear that the material has plenty of advantageous attributes for energy storage applications [5].

Unfortunately, NMC811 has several disadvantages that has thus far limited their commercial implementation. One of the biggest problems with all nickel rich NMC candidates, is the high capacity loss caused by the formation of an rock-salt structure on the NMC surface [40, 41]. These changes occur when the electrochemically active layered structure transforms into an inert rock salt structure [41] which can no longer undergo the lithium intercalation reaction; these transformations typically occurs when the material is at high levels of delithiation (when the cathode is near the upper voltage limit) [40, 42], as forming the inert rock-salt structure is more thermodynamically stable than the layered structure at high levels of delithiation [42]. Literature has

shown that this rock-salt structure formation also leads to increases in interfacial resistance [30] which manifests as poor stability, poor calendar storage, and poor cycle life [40, 41, 43]. Furthermore, the degradation of the active layer structure is also accompanied with dissolution of the structural transition metal ions (nickel, manganese, and cobalt) into the electrolyte, which can then cause further unwanted side reactions within the cell, this will be covered in further detail in a later section.

1.2.2 Anode Materials

1.2.2.1 Lithium Metal

Lithium metal has long been known as the theoretical best choice as the lithium-ion anode material, mainly due to its exceptionally high theoretical specific capacity (3860 $mAhg^{-1}$) and very low redox potential (-3.04 V vs SHE), which no other current anode material has. As such, there are numerous studies focussing on using lithium metal anodes, such as in Li-Air and Li-S systems [44, 45].

Differing from LFP and NMC materials where lithium ions is intercalated and extracted from distinct sites within the crystal structure, lithium metal anodes instead operate based on plating and stripping process from the surface of the lithium metal. This process involves the lithium ion being reduced to metallic lithium (Li^0) and deposited onto the surface of the working electrode (also metallic lithium). This process allows access to an excess of lithium ions from the lithium metal electrode in comparison to materials that utilise the intercalation mechanism where there are a limited number of intercalation sites, therefore much higher values of specific capacities can be achieved.

This key difference in processes however is one of the main reasons why lithium metal has not yet seen widespread implementation in commercial uses; upon charging and discharging, lithium metal is plated and stripped from the surface, however each time it does not remove and deposit at the same locations but rather preferentially at certain locations. This irregular plating and stripping eventually leads to the formation of spiky microstructures called dendrites, which uncontrollably form during the cycling of the cell [46]. Several issues can be encountered when dendrites are formed, such as internal short-circuiting, creation of electrochemically inert lithium which leads to permanent loss of capacity, and in extreme cases thermal runaway [46-48]. For lithium metal to have commercial success, all these issues must first be addressed, which is unfortunately a very tall task.

Due to their extremely high specific capacities, lithium metal can be used to analyse cathode materials as it removes the possibility of anode capacity limitations on the electrochemistry. For example, in systems where the anode may possess poor lithium-ion diffusion or low capacity, causing the anode to be the limiting factor for the charging/discharging mechanisms, then the performance of the cathode could be accurately studied by replacing said anode with a lithium metal anode. Within this project, lithium metal will primarily be used to isolate the electrochemical behaviours of other electrodes of interest by constructing "Half-Cells" whereby the electrode of choice is paired with lithium metal i.e., graphite half-cell is graphite vs lithium metal.

1.2.2.2 Graphite

Ever since Sony Corporation first commercialised the LCO vs graphite lithium-ion battery, graphite has been the dominant choice for anode materials in lithium-ion battery systems. Thanks to its high theoretical specific capacity (372 $mAhg^{-1}$), low redox potentials close to Li/Li^+, good long term cycling stability, excellent electronic conductivity, high abundancy and relatively low cost [7, 8], it has dominated the commercial battery scene where it has seen widespread use in a variety of purposes.

It is already well known that graphite has good electrical conductivity, however it also has very good ionic conductivity, allowing lithium-ions to intercalate in between the graphitic layers during charging of the cell. Figure 4 illustrates the lithiated graphitic structure. The lithium intercalation reaction allows one lithium ion per graphite unit cell (C_6) as seen below in Equation 1.

$$x\ Li^+ + x\ e^- + \ 6C \leftrightarrow Li_xC_6$$

Equation 1 - Graphite reaction scheme

One of graphite's most advantageous attributes is its ability to form a stable passivating layer on its surface, named the solid electrolyte interphase (SEI), which is integral to maintaining excellent electrochemical performance in long term cycling. The SEI layer is a lithium-ion conductive, electronically insulating layer formed at the anode surface through the reduction of electrolyte components when the redox potentials of the electrodes lie outside of the electrolyte stability window [49, 50] (diagram shown in Figure 5). This surface layer has been found to be crucial in determining the electrochemical performance of lithium-ion batteries, affecting capacity loss, self-discharge characteristics, cycle life, rate capability and safety [51]. In order for the SEI layer to function efficiently and to allow effective lithium intercalation reactions in the graphite structure, the layer should possess the following qualities [52]:

1. Low electronic conductivity (to prevent further electrolyte reduction).
2. High ionic conductivity (to allow lithium ions to migrate to and from the active material with the electrolyte).
3. Strong and stable composition (to be resistant to degradation and can accommodate expansion and contraction of the graphite structure).

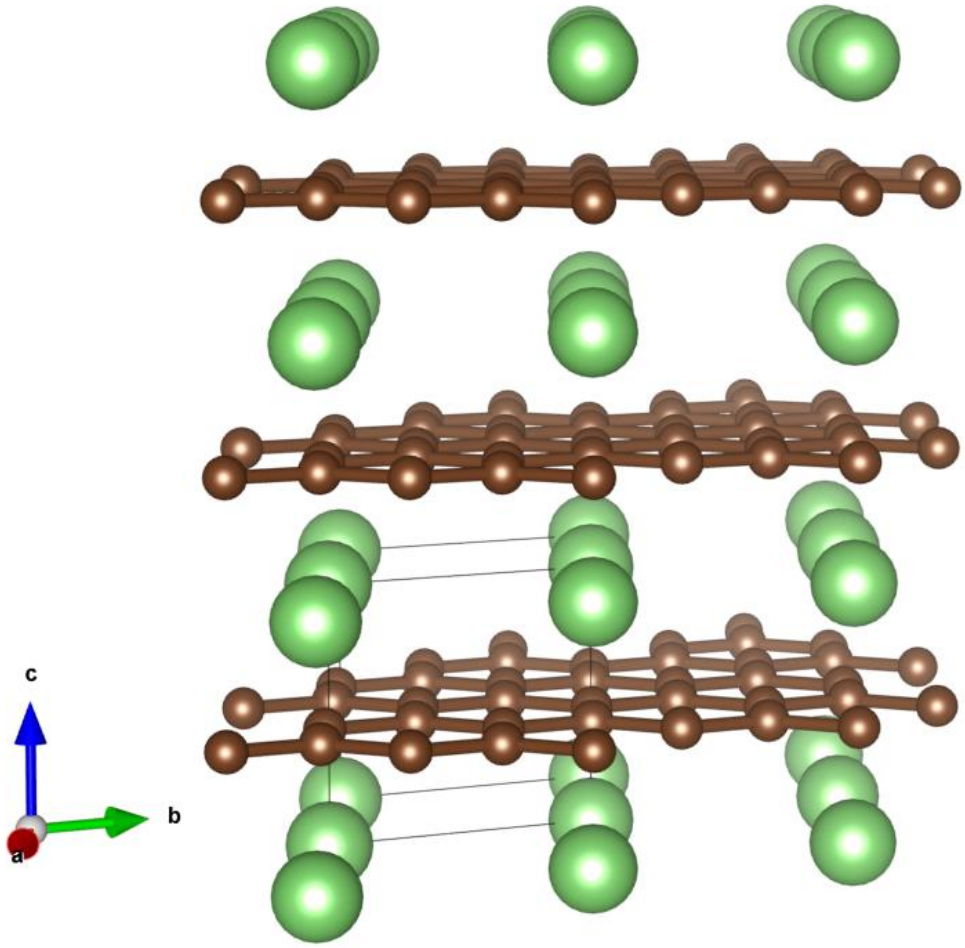

Figure 4 - Lithiated graphite crystal structure, two dimensional layers for lithium ions. Figure was produced using VESTA 3 with the structure obtained from Inorganic Crystal Structure Database (ICSD).

The SEI layer formation reaction on the graphite surface is extremely complex and can vary depending on a number of factors such as graphite morphology, the electrolyte composition, and the electrochemical cycling conditions [53]. The SEI layer typically forms at low potentials (0.8 V vs Li^+/Li for ethyl carbonate based electrolytes [54]) and occurs within the first several charging cycles; at later cycles, due to the electrical insulation properties of the SEI, no further SEI formation reactions should occur.

Although the SEI layer is very important to the longevity of the cell, the intimate details of what occurs during its formation and during cycling is still not well known [55]. This is partly due to the fickle nature of the SEI layer; the interphase is very dependent on the chemical environment in which it is formed and is highly susceptible to change depending on the conditions thus will vary slightly from cell to cell. Furthermore, it is very delicate and exposure to the wrong conditions could render any data gathered useless [56],therefore making attempts to predict the SEI's behaviour difficult and also limits the available in-situ investigative methods.

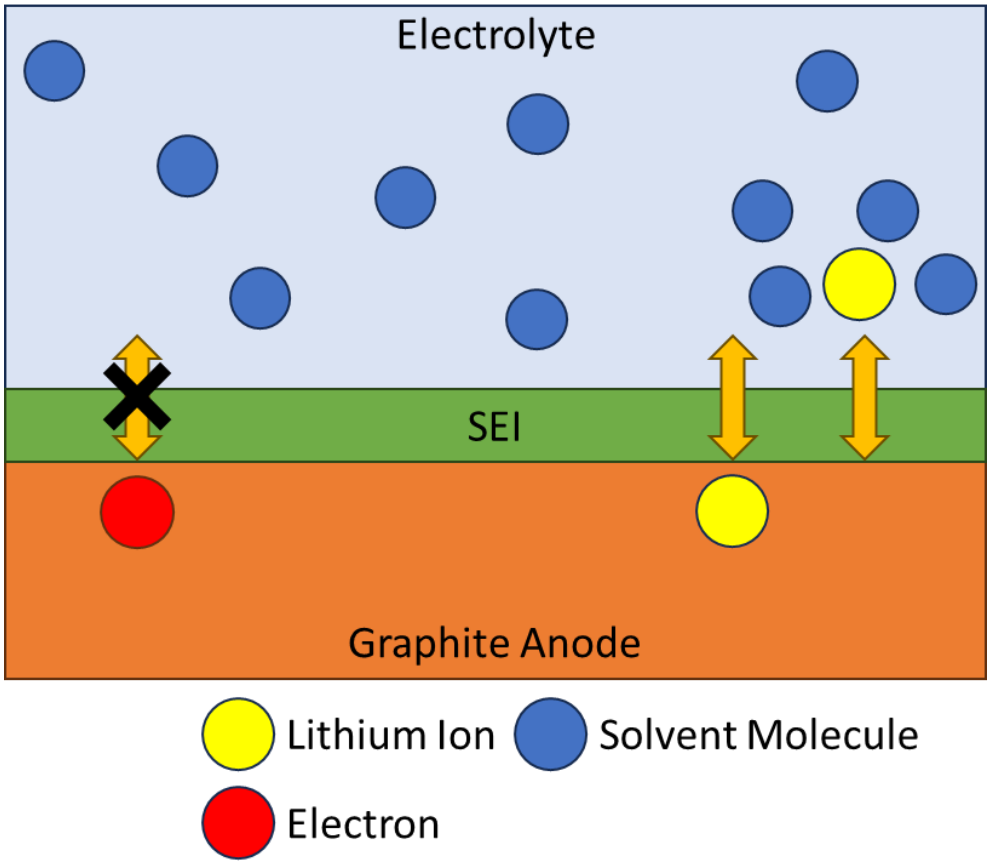

Figure 5 – Diagram showing the SEI layer that is formed on the surface of the graphite anode. This layer is electronically insulating whilst ionically conductive for Li^+ ions.

As mentioned above, the SEI layer is electronically insulating whilst remaining ionically conductive, thus allowing the movement of lithium ions through the layer whilst limiting electrons, which is akin to a solid-state electrolyte hence the name solid electrolyte interphase [53]. By acting as an electronic barrier between the electrode surface and the electrolyte, it is possible to limit further reduction of electrolyte components, hence providing a longer cell lifetime as continuous electrolyte depletion would be detrimental, thus making the formation of a good SEI layer necessary for many applications [51].

Furthermore, the formation of this passivating layer can limit parasitic side reactions that would ordinarily decrease the performance of the cell, such as further reactions with electrolyte components or impurities [51], which would otherwise decrease the cells longevity and electrochemical performance. It is important to note that ultimately, parasitic side reactions will still occur within the cell, the question is how much can be limited from occurring. If it is possible to understand the intricacies of SEI formation, it is possible to formulate effective strategies and solutions to ensure satisfactory SEI layer formation. Currently, one the most popular ways of formulating a strong robust SEI, is through the choice of electrolyte additives, which will be discussed in further detail later in this chapter.

To summarise, wielding strong electrochemical properties in conjunction with the ability to form an advantageous SEI layer, graphite is a phenomenal candidate for the anode material, and is currently used in the majority of commercial lithium-ion batteries [57] despite extensive research into anode alternatives. Whilst other candidates exist such as $LiTiO_2$ (LTO), silicon and metal oxides they all have their respective drawbacks that prevent them from succeeding graphite [57, 58].

1.3 Gas Evolution

1.3.1 Gas Analysis Methods

There are many ways to perform gas analysis using a wide variety of equipment; It is important to note that each technique has its own respective advantages and disadvantages, and the choice method for each experiment can vary depending on the desired outcome.

Techniques such as Gas Chromatography Mass Spectrometry (GC-MS), Differential Electrochemical Mass Spectroscopy (DEMS) and Online Electrochemical Mass Spectroscopy (OEMS) are frequently used in gas analysis experiments due to their ability to identify individual gas species that arise during cell cycling [59]. Furthermore, DEMS and OEMS also allows the quantification of the compounds whilst simultaneously recording the electrochemical data (voltages/currents etc.) [60, 61]. These techniques have shown to be invaluable in numerous studies within the lithium-ion battery research community and has shed light on the chemical processes that occur within the cell [61-65]. The problem with these three techniques mainly lies within the costs and difficulties surrounding the equipment; a mass spectrometer may not necessarily be accessible in many laboratories and even so, only a single cell could be analysed at a time which severely limits the ability to screen numerous cell chemistry candidates. Furthermore, these techniques can be invasive and rely on actively removing gaseous species and exposing the cell stack to conditions that are often not representative of real-world situations.

It is possible to analyse cell chemistries through less invasive means, for example measuring the change in cell volume or pressure, which provides information about the total amount of gas produced within the cell. Various examples of these methods for gas quantification have been reported, such as recording the cell thickness variation over time in pouch cells [66], measuring the buoyancy force of a pouch cell submersed in fluid and relating that to the volume change [67], or the use of pressure transducers that convert the physical exertion of pressure into an electric signal [68] .

Within this project, the chosen method for gas analysis was the utilisation of a simply modified Swagelok union cell which has been adapted to connect to a pressure transducer. In commercial settings, pouch cells are the industry standard, where they are machine-made in large batches whereby each batch has the same cell chemistries [69]. Conducting research on these pouch cells have the advantage of being commercially relevant as these cells are the same as those used in the automotive industry, however they have limitations for lab-scale research. At lab-scale research, it is important to be able to screen a wide variety of cell chemistries, where new electrode sheets can be made and implemented in a cell in a short time span, this is simply not possible to do with commercially made pouch cells. Coin cells and Swagelok union cells are significantly more common when investigating new materials for lithium-ion battery technologies and have also been successfully adapted to conduct gas evolution experiments [65, 70, 71]. Using these cells and pressure measurement techniques, it is possible to deduce the cells electrochemical performance whilst also obtaining gas analysis data.

1.3.2 Gas evolution at Graphite Electrode

The reactions that occur at the graphite electrode are complex, yielding many different products, however not all of these are desirable or beneficial for the cell. Some of these reactions result in gas evolution occurring and one such example is the formation of the SEI layer during the initial charging cycle [72]. The SEI formation reaction involves the reduction of electrolyte components to give a combination of organic and inorganic solids which make up the SEI layer [50], and also generates gaseous species such as C_2H_2, CO and CO_2 [72].

In the absence of electrolyte additives, C_2H_4 is the main gas that evolves from SEI formation on graphite [72]. C_2H_4 is formed through a one-electron reduction reaction where Ethylene Carbonate (EC) undergoes a ring opening reaction which is subsequently involved in another one-electron reaction of two reduced EC molecules to give LEDC and C_2H_4 [73, 74]. An alternative reaction mechanism is also possible using a two-electron reduction of the EC molecule, resulting in Li_2CO_3 precipitation and C_2H_4 gas production. CO and CO_2 are formed simultaneously with C_2H_4 and is

also formed first by a one-electron ring opening process which is then followed by a one-electron cleavage process [75, 76].

Another gas evolution reaction that occurs at the graphite electrode is through the reduction of contaminants such as water within the cell. For example, it is widely known that residual moisture within the cell can result in the formation of H_2 gas; it has been found that increasing concentrations of water within the cell results in increased H_2 gas evolution [72]. These water reduction reactions occur at below 2 V vs Li/Li^+.

Beyond the required gas evolution to produce the graphite SEI, gas evolution is seen as detrimental to cells as the increase in pressure within cells can lead to cell deformation, uneven cell reactions due to bubble formation, further unwanted side reactions or in extreme cases safety issues as these gasses can be highly flammable [77]. In the event of thermal runaway, this could be extremely dangerous.

Examples of gassing reactions at the graphite surface can be seen below in Figure 6. Where reactions [A] to [D] are all reductions of EC at the lithiated graphite surface to form different products. Reaction [A] produces ethene (C_2H_2) and lithium ethylene dicarbonate (LEDC or ($CH_2OCO_2Li)_2$), reaction [B] produces ethene and lithium carbonate (Li_2CO_3), reaction [C] produces carbon dioxide (CO_2) and lithium alkoxide (RO-Li), and reaction [D] which forms carbon monoxide (CO) and lithium alkoxide. Reaction [E] shows the reduction of water at the graphite surface to form hydrogen gas (0.5 H_2) and a hydroxide ion (OH^-).

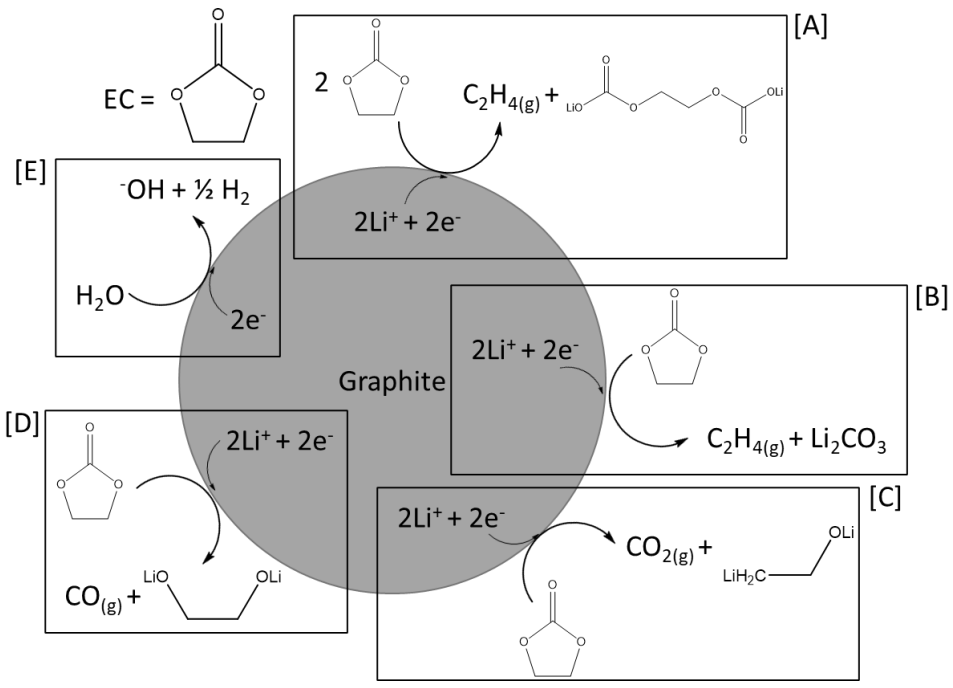

Figure 6 - Examples of gas evolution reactions occurring the graphite surface. Reaction [A] adapted from reference[74], [B] from [56], [C] from [75], [D] from [78], [E] from [60].

Highlighting the complexity of gas evolution reactions that occur on the graphite surface.

The gassing reactions shown in Figure 6 show the typical gassing reactions that may occur on the graphite surface, however this is very much dependant on the cell system, for example introduction of contaminants, additives, or different electrode materials may alter what gassing reactions will occur. This concept will be crucial in this project where we will investigate different factors that will affect gassing reactions.

1.3.3 Effect of Transition Metal Dissolution on Gas Evolution

During the cell's lifetime, it is inevitable that the cathode structure will undergo degradation reactions which can have adverse effects on the cell chemistry. Transition metal dissolution is one such example of these degradation events, where the loss of transition metals from cathode materials, such as NMC, can lead to irreversible structural change, rendering it less effective in the standard lithium intercalation mechanisms [79, 80].

The damage however is not simply limited to structural degradation of the cathode material, the dissolved transition metals can subsequently deposit and accumulate at the graphite electrode which can then impact the SEI layer [81-83]. This problem is significant as the incorporation of transition metals, such as nickel and manganese, on the anode surface can cause further unwanted reduction of electrolyte, producing further gases, by disrupting the SEI layer. This occurs as the transition metals can cause the SEI layer to be a less effective electronic barrier [83]. Furthermore, manganese accumulation onto the SEI structure is thought to cause catalytic decomposition of the SEI layer, and thus drastically reducing its effectiveness and leads to increased parasitic side reactions [81].

It is known that the negative impact of dissolved Mn^{2+} is considerably higher than Ni^{2+} and Co^{2+} [11, 80]; this occurs through many different complex pathways however the catalysis of SEI decomposition is among one of the most problematic. It is thought that the presence of manganese in the SEI layer causes a catalytic chain of reactions which leads to the continuous breakdown of the SEI layer and therefore diminishing the effectiveness of its passivity [81]. This process has been suggested to occur in several steps:

1. Deposition of dissolved Mn^{2+} onto the SEI layer.
2. Migration and reduction of the dissolved Mn^{2+} to Mn^{0} in the SEI layer by electron transfer from the graphite surface.

3. If the reduced Mn is surrounded by LEDC then the LEDC will be reduced to Li_2CO_3 (and C_2H_4 gas) causing the Mn^0 to oxidise back to Mn^{2+}.
4. The Mn^{2+} can then be reduced once again by electron transfer from the graphite surface (step 2) to become a catalytic cycle.

This proposed catalytic reaction can be seen in Figure 7.

Within NMC cathodes, it has been found that transition metal dissolution occurs stoichiometrically [80], therefore in materials such as NMC811, the highest absolute amounts of transition metal dissolved would be nickel. The impact of dissolved nickel, like manganese, on the graphite SEI causes C_2H_2 evolution, however the extent of gas evolution is smaller, which suggests that the pathway for decomposition might not be as catalytic [83]. This is most likely because the Ni ions are less reactive than Mn ions as it is less susceptible to form Ni^0, which has been seen in literature previously [80, 84, 85].

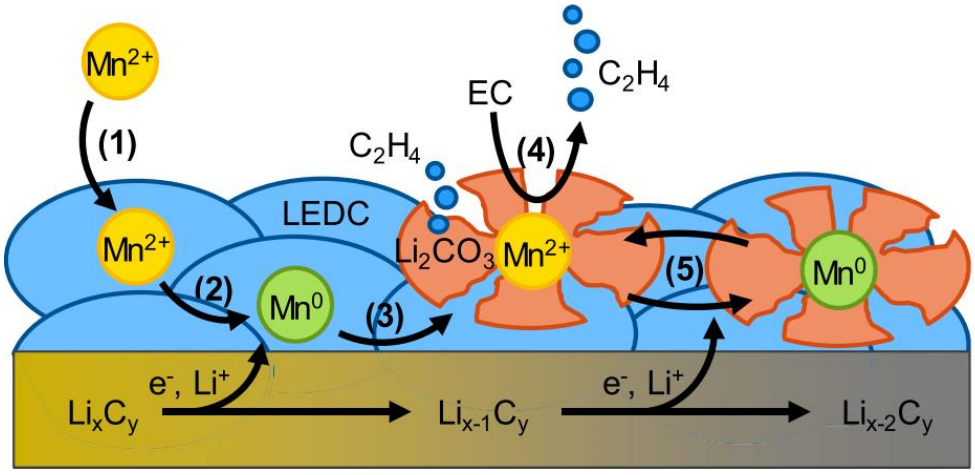

Figure 7 – Proposed catalytic pathway for the disruption of the graphite SEI by manganese dissolution, causing gas evolution via reduction of LEDC compound and further decomposition of EC. Taken from reference [83].

1.4 Improvement Strategies

1.4.1 Additives

Electrolyte additives have proven to be a powerful asset in developing an overall more successful battery and are commonly used in commercial cells. Small quantities of electrolyte additives are often sufficient to dramatically increase the battery performance thus making them highly economically effective [86]. Furthermore, when investigating avenues of improving the battery performance, additives provide a flexible approach as it can be applicable to almost every

cell design or active material. Regardless of whether it is a commercial pouch cell or a lab-scale coin cell, the impact of the electrolyte additive will be comparable, making it very easy to transition research into commercialisation.

There are numerous additives that can provide an assorted range of characteristic improvements to lithium-ion batteries, and depending on your desired outcome, it is possible to have a targeted solution to a poor performing cell system. For example, cells that are designed to function in extreme temperatures, would benefit from additives that provide thermal stability [86, 87]; additives can also be targeted at specific components, for example some electrolytes are known to improve characteristics specific to the cathode, stabilising the cathode structure from degradation [10].

Finally, from a research perspective, the screening of various additives and investigating the impact on a cell system is relatively uncomplicated, where the addition of additives can quite easily be incorporated into the existing experimental procedures and simply requires a process for changing the electrolyte formulation.

Within this project, we will investigate three key additives that have shown huge potential in commercial use due to their ability to modify the SEI layer on the graphite surface. These three additives are vinylene carbonate (VC), 1,3,2-dioxathiolane-2,2-dioxide (DTD), and $LiPO_2F_2$ (LFO). Whilst these three additives have already shown to provide several enhancements to the SEI layer, it has not been extensively investigated with regards to their interactions with transition metal dissolution and the subsequent impact on gas evolution.

1.4.1.1 Vinylene Carbonate (VC)

Vinylene Carbonate (VC), shown in Figure 8, was first used as an electrolyte additive by Saft in 1994 (patent accepted in 1997) [88], where they had discovered that small quantities was sufficient in promoting the formation of a passivating layer – the SEI layer. Since its discovery, VC is now currently one of the most popular electrolyte additives that is used in lithium-ion batteries; subsequently, this has led to it being one of the most studied additives with its characteristics and effects on the SEI being very well documented in literature [89-95].

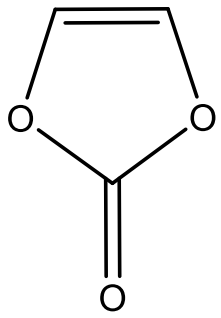

Figure 8 – Chemical structure of Vinylene carbonate (VC)

As discussed previously, the formation of a SEI layer to passivate unwanted side reactions on the graphite surface is imperative to the electrochemical performance of the cell. VC as an electrolyte additive has been shown to improve the quality of the SEI layer by reacting at the graphite surface prior to the electrolyte solvents, to form new reduction products that when present in SEI, improve uniformity and stability of the passivating layer [91, 96]. Typically, without the presence of the VC additive, the SEI layer consists mainly of lithium salt species (Li_2CO_3, LiF, LiOR, lithium ethylene dicarbonate or LEDC, and Li_2O). These lithium salt species are formed through the reduction of the ethylene carbonate (EC) molecules in the electrolyte solvent. However when VC is present and reduced, polymeric chain species are formed and incorporated into the passivating layer which is thought to make the SEI more uniform, flexible and stable [91]. This newly formed SEI layer then boasts many advantages such as increased ionic conductivity, reduction in parasitic side reactions, and increased cycling longevity [90, 91, 97].

VC has proven to be a powerful additive that can significantly improve the performance of lithium-ion batteries; however, Burns et al. found that there was a trade-off, where with increasing VC concentration came increased cell impedance when VC concentration was increased beyond 2% [90, 92]. Despite showing advantageous traits when VC is added, it is clear that careful formulation of the electrolyte composition and the VC concentration is needed to ensure a well-functioning cell rather than simply adding excess amounts of additives.

There is currently an abundance of literature describing the benefits of various electrolyte additive candidates and it is often common for electrolytes to achieve improved electrochemical results over cells with an absence of additives [98]. However, for an electrolyte to have greater benefits than the industry standard of 2% VC is very difficult, therefore here in this project, 2% VC additive will be used as the benchmark for all other additive/additive combinations to be compared to.

1.4.1.2 1,3,2-dioxathiolane-2,2-dioxide (DTD) and VC Combination

1,3,2-dioxathiolane-2,2-dioxide (DTD), shown in Figure 9, belongs to a family of organic sulphur-containing additives named as the cyclic sulfonates. These sulfonates were quickly found to be similar to VC as they too were an anode targeted additive which could help form a stronger and more robust SEI, again by preferentially reacting at the graphite surface prior to the electrolyte compounds to form a thin and compact SEI with a lower impedance than cells without DTD [99, 100].

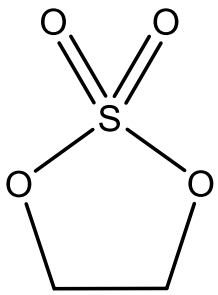

Figure 9 – Chemical structure of 1,3,2-dioxathiolane-2,2-dioxide (DTD)

Work done by Sano and Maruyama found that using the DTD additive led to a modified SEI layer which contained new polymeric and Li_2S like compounds, which led to the suppression of the initial irreversible capacity loss and allowed increased first cycle efficiencies [101]. Furthermore, it has been shown that the addition of DTD as an additive has improved other aspects of the cell such as better storage life and increased performance at high and low temperatures [101-104].

As VC is used as the benchmark for additive comparisons, it is important to only screen candidates that are competitive respective to the VC additive. Xia et al. demonstrated that the use of DTD as the lone additive allowed comparative electrochemical results to that of VC as a lone additive, however when using a blend of DTD and VC together as an additive combination, better electrochemical performances could be achieved (compared to VC alone) [99]. This combination of DTD and VC together as an electrolyte additive combination, clearly shows promise as a potential additive candidate which could compete with VC, however, requires more research before it can be used.

Here in this project, both cells with DTD (alone) and DTD with VC combination will be investigated but with further attention given specifically to the DTD with VC combination.

1.4.1.3 $LiPO_2F_2$ (LFO)

In 1997, Sanyo Electric company discovered that certain phosphorus-containing lithium salts such as lithium difluorophosphate ($LiPO_2F_2$, known here as LFO), shown in Figure 10, at small

quantities could be used as an electrolyte additive. Interestingly, LFO is a detectable reduction product of the $LiPF_6$ salt that is already present in the electrolyte; initial work done by Andersson et al. intended to use the LFO additive to prevent the $LiPF_6$ decomposition [105], however it was later found that the addition of LFO actually helped the formation of an thin SEI layer with better ionic conductivity and electronic insulation properties, which thus improves the overall electrochemical performance [106].

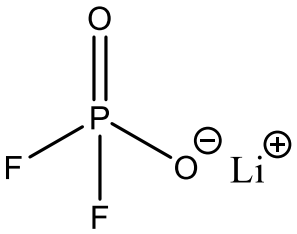

Figure 10 – Chemical structure of $LiPO_2F_2$ (LFO)

It has been shown that a stable SEI even without the use of additives, typically contains $Li_xPO_yF_z$ compounds within the passivating layer [107]; these compounds, when present in the SEI, have been found to contribute towards reducing parasitic side reactions, increased capacity retention and reducing unwanted lithium plating [107, 108]. By utilising LFO as an additive, it is possible to increase the content of $Li_xPO_yF_z$ within the SEI layer and thus improving the cells performance [109]. Drastic improvements can be achieved even at very low concentrations (1% wt.) making it a strong competitor amongst electrolyte additive candidates [109].

Ma et al. demonstrated using NMC532/graphite pouch cells, that the addition of just 1% LFO (there labelled as "LiDFP") improved the cell cycle lifetime to a degree that is comparable if not better than cells containing just 2% VC [109], making a LFO an interesting candidate for further study in this project.

1.5 Thesis Aims and Objectives

The aim for the project is to use a highly sensitive cell design [68], using standard Swagelok cell parts to perform operando quantitative detection of gas evolution from lithium batteries via operando pressure measurements, with a focus on examining the impact of transition metal dissolution and electrolyte additives on the formation reaction of the graphite SEI layer.

Transition metal dissolution is a process that occurs as a result of the degradation of cathode materials such as NMC, in which the transition metal ions from the cathode dissolve into the electrolyte, which unfortunately, severely disrupts the SEI layer on the graphite surface[80]. A method of investigating the effect of dissolved transition metal ions, without the complications of

introducing a NMC electrode, is to purposely add the metals to the electrolyte via metal bis(trifluoromethanesulfonyl)imide (TFSI) salts ($NiTFSI_2$ salt etc.) [83], thus allowing the quantitative control of transition metal dissolution. The TFSI anion is not expected to have any noticeable impact on the cell system. Furthermore, this allows us to utilise an inert counter electrode, such as LFP, so that the gas evolution properties of the cell can be unambiguously ascribed to the graphite response.

The introduction of electrolyte additives is another important factor that affects the SEI formation properties, and thus, it is worth studying their effect on the graphite gassing behaviour to deepen the understanding of the reaction mechanism of the additive and its effect on battery performance.

The present study differentiates from other gas analysis studies in the literature in the following aspects: i) uses an inert and oversized LFP electrode to selectively study the full gas evolution properties of the graphite electrode, ii) employs a highly sensitive cell design that enables the reliable quantification of the amount of gas produced or consumed via operando pressure measurements, and iii) systematically investigates the effect of the presence of dissolved transition metal ions, selected electrolyte additives, and their combination. These investigations produced new understanding on the effects of dissolved manganese, nickel and cobalt on the gas evolution and consumption reactions on graphite, as well as how electrolyte additives affected these reactions.

Chapter 2 Methodology and Optimisations

2.1 Context

The end goal for the project is to use a modified Swagelok union cells to perform operando detection of gas evolution from lithium-ion batteries, examining the impact of transition metal dissolution and electrolyte additives on the SEI layer and the associated gas evolution behaviours.

Work done during my fourth-year integrated masters project, “Lab scale investigation of mechanism of degradation of high-capacity battery materials (NMC811 and NMC622) using 3-electrodes cells”, provided a rudimentary methodology which acted as an initial framework which would subsequently be developed and optimised to achieve this project’s goals.

Within this chapter, the final experimental methodologies will be detailed, and the optimisations and adaptations that took place to achieve this will be discussed.

2.2 Methodology

2.2.1 Baseline Swagelok Assembly

The previous work done in the master’s project had many parallels to the work done in this project, most notably the assembly of Swagelok cells to conduct electrochemical testing of various cathode and anode materials, thus helping form the initial experimental methodologies for this project. Below a summary of that original procedure for Swagelok cell assembly is given.

Firstly, all the Swagelok cell components are cleaned via sonication, once in water, then a second time in ethanol. Current collectors and the cell body required the additional step of polishing using sandpaper (3M P1200 wet and dry sandpaper) prior to sonication. The Swagelok components utilised are listed below in Table 1.

After sonication, half of the Swagelok cell was then assembled (labels A-F in Figure 11) with the aim of reducing the amount of work needed for assembly in the glovebox later. The half-assembled cell and the rest of the cell components were then dried in a vacuum oven at 80 °C for 24 hours.

Electrodes and separators (GF-F, Whatman) were cut and then dried in a Buchi tube at 120 °C for 72 hours. Procedure for electrode production is described in more detail in section 2.2.4.

Cell components, electrodes and separators were transferred into a glovebox after drying step was complete. These parts were then allowed to cool down to room temperature overnight.

Once cooled, the components are arranged as shown in Figure 11 with the addition of a Teflon FEP film which lined the cell body wall to act as an electrical insulator between the current collector and the cell body. The cell stack was organised as shown in Figure, with the separators wetted with 600 µL of the formulated electrolyte (see section 2.2.2 for electrolyte preparation methodology).

After the cell has been assembled, it is transferred out of the glovebox and subjected to electrochemical cycling, the details of which is described later in section 2.2.5.

Label	Component	Material
A	Cathode current collector	Copper/Aluminium, dependant on electrode
B	Nut	Stainless-steel
C	Ferrules	Nylon
D	Spring	Stainless-steel
E	Cap	Copper/Aluminium, dependant on electrode
F	Cell body	Stainless-steel
G	Cell stack	Electrode/2x GF-F/electrode
H	Anode current collector	Copper for all cells

Table 1 - List of Swagelok cell components and their relative materials. Label column corresponds to those seen in Figure 11.

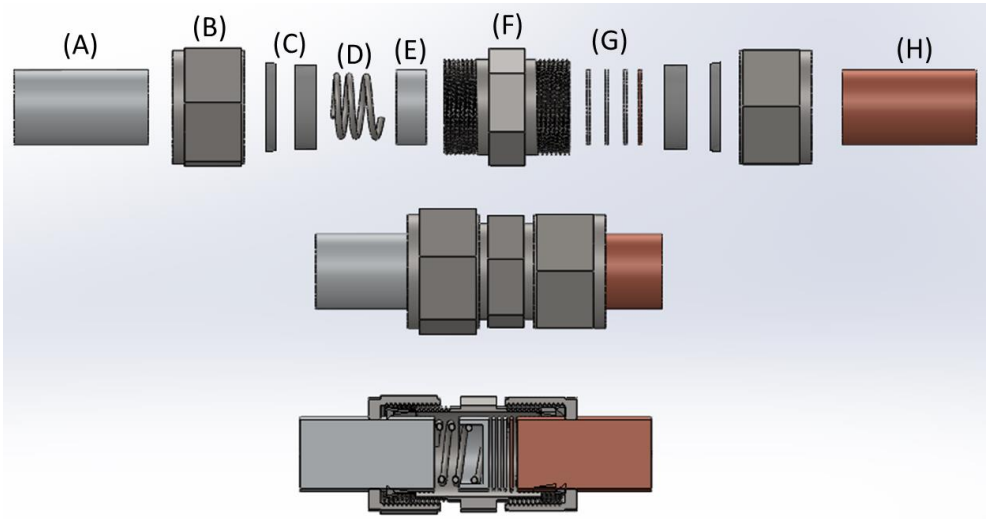

Figure 11 – Diagram showing the Swagelok cell parts used in the baseline assembly in a deconstructed, constructed, and cross-sectional view. Labels (A-H) correspond to parts listed in Table 1 where additional information is given.

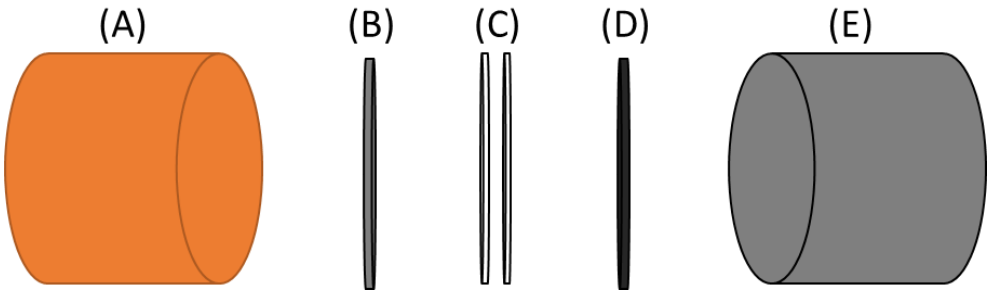

Figure 12 - Cell stack arrangement for standard Swagelok cell configuration. where (A) – cap, (B) – counter electrode such as lithium metal or graphite, (C) – 2x GF-F separator, (D) – working electrode such as LFP or graphite, (E) – current collector.

2.2.2 Electrolyte Preparation

Throughout this project, various electrolyte formulations will be used in the LFP vs Graphite Swagelok cells, here the methodology for preparing these electrolytes will be outlined.

LP57 (1M LiPF6 in ethylene carbonate (EC) and ethylene methyl carbonate (EMC) with EC: EMC weight ratio of 3:7), also denoted as “Baseline electrolyte”, and LP57 + 2% VC (1M LiPF6 in ethylene carbonate (EC) and ethylene methyl carbonate (EMC) with EC: EMC weight ratio of 3:7 and added 2% VC by weight) were pre-formulated and sourced from Soulbrain MI.

Electrolytes used for investigating the effects of dissolved transition metals (Chapter 3) were made by dissolving transition metal salts in the pre-formulated LP57 electrolyte, such that the concentration of the transition metal salt was 10 mmol. Transition metal salts used were:

Nickel bis-(trifluorosulfonyl)imide ($Ni(TFSI)_2$, Alfa Aesar, 95%), Manganese bis-(trifluorosulfonyl)imide ($Mn(TFSI)_2$, Solvionic, 99.5%), and Cobalt bis-(trifluorosulfonyl)imide (, $Ni(TFSI)_2$, Alfa Aesar, 95%).

Electrolytes used for investigating the effects of electrolyte additives (Chapter 4) were made by dissolving the additive in the pre-formulated LP57 electrolyte or LP57+2% VC, such that the weight percentage of additive matched that seen in literature (DTD – 1%, LFO – 1%, VC+DTD – 2% and 1% respectively) [99,109], with the exception of the LP57 + 2% VC electrolyte which was preformulated. The electrolyte additives used were: 1,3,2-Dioxathiolane 2,2-dioxide (DTD, Sigma-Aldrich, 98 %), and LiPO2F2 (LFO, TCI chemicals, 98%).

Electrolytes used for investigating the effects of electrolyte additives with the co-addition of Mn ions (Chapter 5) were made by first making the LP57 with 10 mmol of $Mn(TFSI)_2$, as described above. This was then used to dissolve the electrolyte additives to again give weight percentages as described above, with the exception of VC where the $Mn(TFSI)_2$ was dissolved in the pre-formulated LP57 + 2% VC electrolyte.

All electrolyte formulation was prepared in an argon glovebox (Labstar, MBraun with H_2O and O_2 <0.5 ppm) and stored in aluminium bottles (Buerkle™ Aluminium Bottles).

2.2.3 Pressure Measurement Adaptations

2.2.4 Electrode Production

Electrode manufacturing procedure involved adding the active material (LFP or graphite, from Tatung or MGP-A from China Steel Chemical Corp., respectively), C65 conductive carbon (Timcal Super C65 Carbon), and polyvinylidene fluoride or PVDF (PVDF 5130) to a mixing pot, where it is then mixed with a glass rod (2 minutes) to ensure all the solid powders are properly dispersed. 1-Methyl-2-pyrrolidone or NMP (Sigma) was then added by pipetting onto the side of the pot to ensure trace materials adhered to the side was washed to the bottom to create an ink slurry. The quantities of powders and NMP solvent is shown below in Table 2.

The mixing pot was then placed in a planetary mixer (Thinky ARE-250) to mix at 2000 RPM for 5 mins, this was repeated until the ink had been mixed 3 times with 5-minute rest in between each mix. The rest time was crucial to allow the cooling of the mixer and the ink slurry (NMP solvent would evaporate at higher temperatures). Whilst the ink was mixing, the substrate foil was cleaned by wiping with Kimtech tissues and excess ethanol. Electrode ink was then coated onto the substrate foil at a set thickness (dependant on the active material) using a DrBlade spreader. The electrode sheet was then dried in a vacuum oven (Thermo scientific, VT 6025)

overnight at 80°C. Once dried, electrodes were punched out using a handheld precision punch (Nogami) and calendared for 1 minute using a hydraulic press (Specac). Details on substrate foil, DrBlade thickness, precision punch size and calendaring pressure can be seen in Table 3.

Ink	Active material (AM) /g	Conductive carbon (CC) /g	PVDF /g	NMP /ml	AM:CC:PVDF ratio
LFP	7.5	0.35	0.35	13.5	92:4:4
Graphite	7	0.24	0.24	7.5	94:3:3

Table 2 – Ink formulation for LFP and graphite electrodes, showing the weights of materials and the desired active material/conductive carbon/PVDF ratio used to make the electrode ink.

Electrode	**Substrate**	**DrBlade thickness /µm**	**Precision punch size /mm**	**Calendaring pressure /tonnes**
LFP 1-inch	Aluminium foil (0.35 mm, 99% purity, Advent)	400	25	5
LFP 0.5-inch	Aluminium foil (0.35 mm, 99% purity, Advent)	400	11	2
Graphite 1-inch	Copper foil (0.1 mm, 99% purity, Advent)	300	25	5

Table 3 – Details on electrode substrates, coating thickness, electrode diameter and calendaring pressure.

Electrodes were then transferred to a Buchi tube and dried under vacuum overnight at 120 °C before being transferred into an argon glovebox (Labstar, MBraun with H_2O and O_2 <0.5 ppm).

For pressure measurements, the graphite 1-inch electrodes were adapted to allow effective gas transfer. This was done by perforating the electrode post ink coating and drying with a 2 mm hole in the centre of the electrode.

Lithium foil (Rockwood lithium) and GF-F separators (Whatman® glass microfiber filters) was punched out using hand punches (same size as their corresponding electrodes i.e., 25mm for LFP 1-inch or 14 mm for graphite coin). Lithium foil was punched out in the glovebox and GF-F separators was punched out in the lab.

2.2.5 Electrochemical Cycling and Analysis

2.2.5.1 Galvanostatic Cycling with Potential Limitation (GCPL)

After cell assembly, cells are placed within a climatic chamber (Memmert, IPP110plus, 25°C) and connected to a potentiostat (Biologic, VMP2) where they are first allowed to acclimatise to the temperature before undergoing galvanostatic cycling with potential limitation (GCPL).

This electrochemical technique subjects the cell to a constant current whilst recording the voltage response over time. During cycling, the constant current induces electrochemical reactions within the cell which is reflected in the voltage changes. Voltage limits are imposed onto the cell, where during cycling, a constant current will be continually applied until the cell reaches the said voltage limit. For example, Figure 13 shows a LFP vs Li 1-inch Swagelok cell, where the cell is first subjected to a constant specific current of 17 mA/g_{LFP} (charging of the cell) which over time leads to the cell voltage reaching the upper voltage limit of 4.1 V. Once the upper voltage limit has been reached, the current is then reversed to -17 mA/g_{LFP} (discharge of cell) until the cell reaches the lower voltage limit of 2.7 V. The charging and discharging of the cell represent one full cycle of the cell and is core to gathering electrochemical data.

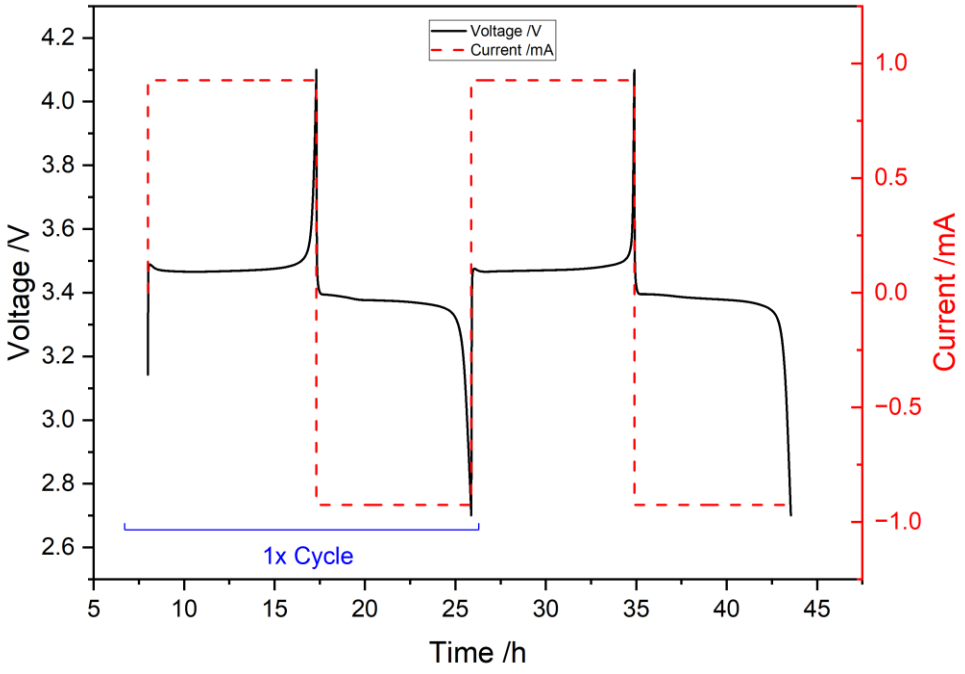

Figure 13 – Example of Galvanostatic cycling of an LFP vs Li half-cell at C/10 or 17 mA/gLFP. 2 cycles are shown with each cycle consisting of a charging phase (positive current imposed) followed by a discharging phase (negative current imposed).

The value of the constant current that is imposed onto the cell is also very important and requires the use of a concept called “C-rate”. The C-rate is the measure of the rate at which the

battery is charged/discharged relative to its maximum capacity. The C-rate also relates the amount of time needed to fully charge/discharge, where higher C-rates would decrease the amount of the time needed to full charge and vice versa.

To calculate the C-rate, it is necessary to determine the maximum capacity of the battery or material. Here, we will employ the theoretical capacities, calculated using Faraday's law (Equation 2) under the assumption that the active material is able to achieve full lithiation/delithiation.

$$Q = \frac{nF}{M}$$

Equation 2 – Faradays Law, Q – theoretical specific capacity, n – number of electrons in reaction, F – Faraday's constant, M – molar mass of the active material.

Using LFP as an example, the reaction mechanism for LFP delithiation is:

$$LiFePO_6 \rightarrow FePO_6 + Li^+ + e^-$$

So, the number of electrons in the reaction is 1 mol, Faraday's constant is 96485 C mol^{-1} however can be converted to 26.8 A h mol^{-1} to have more convenient units, and the molar mass of LFP is 157.755 g mol^{-1}. This gives us a theoretical specific capacity:

$$Q = \frac{1\ mol * 26.8\ A\ h\ mol^{-1}}{157.755\ g\ mol^{-1}} = 169.9\ mA\ h\ g^{-1}$$

During the cell assembly step, the working electrode would be weighed, and by knowing the mass of the foil substrate and the active material percentage of the ink, it is possible to determine the mass of active material (LFP in this case) and therefore calculate the theoretical capacity of the electrode.

$$C - rate = \frac{I}{Q}$$

Equation 3 – C-rate, I – Current, Q – Theoretical specific capacity.

Using the equation for the C-rate (shown above in Equation 3), the desired current can be calculated dependent on the desired C-rate. For example, in the experiments shown in Figure 13, the LFP working electrode was found to 9.26 mA h capacity, therefore, to achieve a C-rate of 0.1C, a current of 0.926 mA needs to be imposed onto the cell.

The cycling protocols used in the optimisation experiments (LFP/Li and graphite/Li half cells, and LFP (WE)/Graphite (CE) full cells) consisted of an open circuit voltage/voltage hold for 8h initially to ensure the electrodes were sufficiently wet by electrolyte and the cell to

equilibrate to the climatic chamber temperature, followed by 2 cycles at C/10 which emulates SEI formations cycles in commercial settings, and then finally 20 cycles at C/2 which would represent real world charging and discharging at a faster rate relative to the formation cycles. For the characterisation of the final system (graphite (WE)/LFP (CE) full cell), the decision was made to change the cycling protocols to faster C-rates and fewer cycles as it was not possible to finish longer term cycling before the project ended.

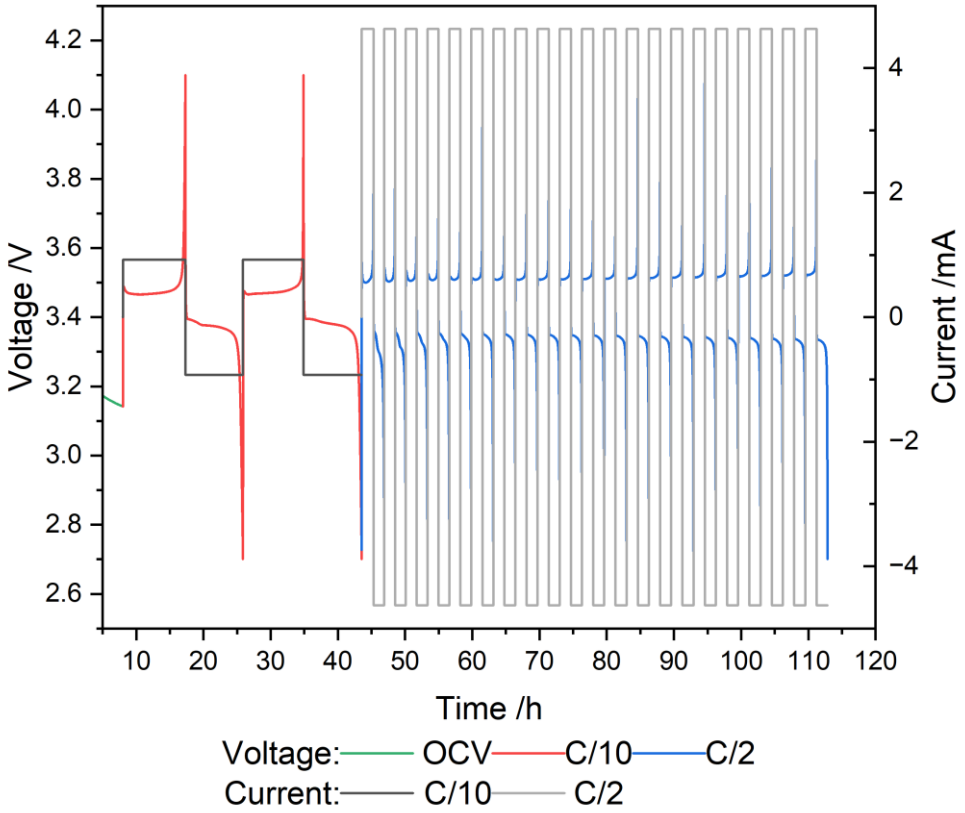

Figure 14 –Example of an LFP vs Li half-cell undergoing a standard galvanostatic cycling protocol, where there is an initial period of cycling at lower C-rate (2 cycles at C/10) followed by subsequent further cycling at higher C-rates (20 cycles at C/2).

It is important to note that the cycling protocol for LFP and graphite differed slightly in that LFP vs Li cells had an open circuit hold for the first 8 hours whereas graphite vs Li and graphite vs LFP cells had a voltage hold at 1.5V. This was the case as the voltages at the open circuit voltage (OCV) hold could induce copper dissolution of the graphite electrode foil, whereas this does not occur at 1.5V.

Voltage limits for the experiments in this chapter were:

- LFP/Li: 2.7 V to 4.1 V
- Graphite/Li: 0.005 V to 1.5 V
- LFP (WE)/Graphite (CE): 2.5 V to 4 V

- Graphite (WE)/LFP (CE): -3.45 V to -1.8 V

The cycling protocol for the experiments in this chapter were:

- LFP/Li: Open circuit voltage for 8 hours, 2 cycles at C/10, 20 cycles at C/2.
- Graphite/Li: Voltage hold at 1.5 V for 8 hours, 2 cycles at C/10, 20 cycles at C/2.
- LFP (WE)/Graphite (CE): Voltage hold at 1.5 V for 8 hours, 2 cycles at C/10, 20 cycles at C/2.
- Graphite (WE)/LFP (CE): Voltage hold at 1.5V for 8 hours, 2 cycles at C/10, 4 cycles at C/5.

An example of an LFP/Li half-cell undergoing galvanostatic cycling under these cycling protocols can be seen in Figure 14.

2.2.5.2 Electrochemical Analysis

The first step when examining the electrochemical data is to analyse the voltage vs capacity graph of the cell, since it serves to visualise the capacity changes between cycles and C-rates which gives a good indication of the overall performance of the cell.

In Figure 15, the voltage vs capacity graph of a LFP/Li cell is shown, where it is first important to note the difference in capacity between the C/10 and C/2 C-rates; the slower C/10 rate allow capacities of ~150 $mAhg^{-1}$ in its first discharge cycle, whereas the faster C/2 only reaches ~140 $mAhg^{-1}$. This small decrease in capacity when increasing C-rate is typically found in the literature and can be attributed to various kinetic limitations (electron wiring, ion diffusion, etc.) [110]. During the project, a small decrease between C-rates is expected however in some cases larger decreases indicate degradation of the active material or unwanted side-reactions occurring.

It is also possible to analyse the degree of degradation within the cell by considering the change in capacity between cycles within the same C-rates. Using Figure 15 as an example again, with each C/2 cycle the capacity decreases by a small increment indicating a loss in capacity within the active material over the course of many cycles. This is to be expected as with each cycle, the active material is expected to participate in some unwanted side reactions which can ultimately lead to its degradation; in a hypothetical scenario where the lithium intercalation reaction is the only reaction occurring with no degradation reactions present, then the potential vs capacity graph profiles would be perfectly overlapping in each C-rate cycle. This route of analysis was especially useful during this project as it was key indicator of the impact of changing variables, i.e., a methodology optimisation could improve capacity retention and thus better overlap of capacity profiles.

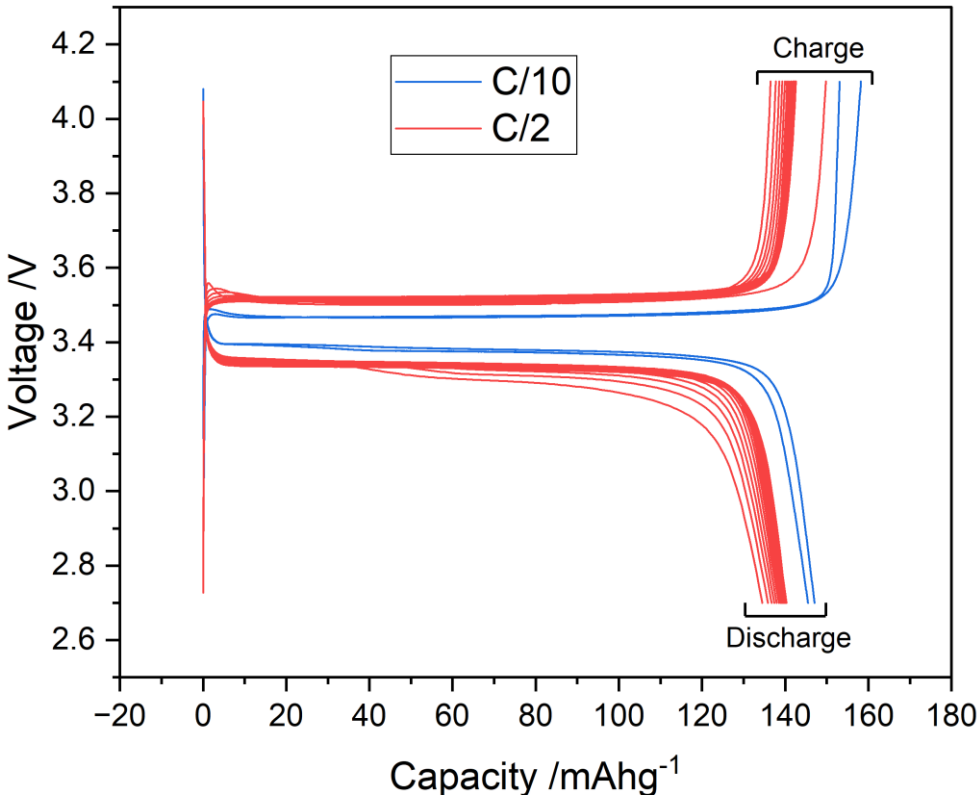

Figure 15 – Example of a voltage vs capacity graph for an LFP vs Li half-cell where the charge and discharge profiles can be observed. Data from this graph it is possible to determine the capacity and therefore coulombic efficiency at each cycle.

An important part of this project is the examination of the SEI formation on the graphite anode. The SEI generally forms within the initial stages of the cycling protocol, and it has been shown that the SEI layer formed under slower C-rates are more stable [111]. These initial slower C-rate cycles are denoted as the formation cycles.

During the formation cycles, charge is consumed to reduce the electrolyte to form the SEI layer, thus allowing the cell to show capacities above the theoretical specific capacity (charge consumed in lithium intercalation + charge consumed in SEI formation); this does not occur during the discharge stage and therefore explaining the decreased capacity.

Closely related to the potential vs capacity analysis, coulombic efficiency vs cycle is also very useful especially in the context of long-term cycling and real-world application of the materials (high coulombic efficiency could mean longer lifetime of the battery). The coulombic efficiency represents the ratio of the charges passed between the charging/discharging stages in a cycle. Again, if the cell were to function perfectly and solely undergo the lithium intercalation reaction, then the efficiency would be at 100%, however this is never the case due to additional reactions occurring. For example, if the coulombic efficiency were to decrease for a given cell, it may indicate that the SEI is damaged and is unable to prevent side reactions or that the active

materials in the cell have degraded and are unable to effectively undertake lithium intercalation/extraction.

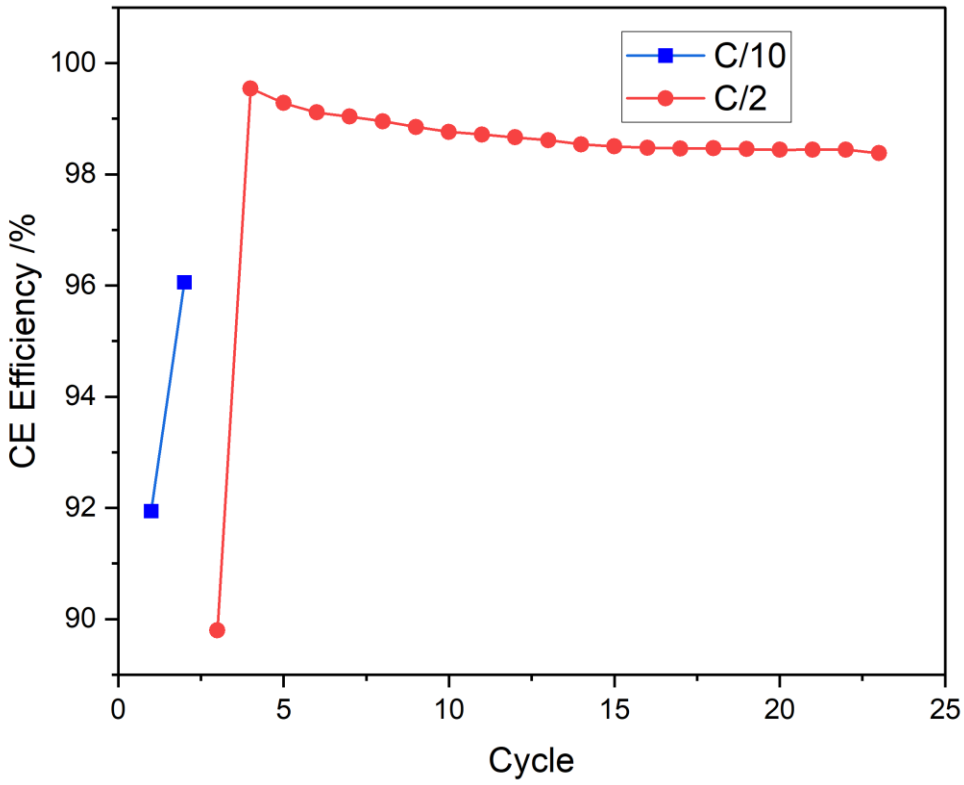

Figure 16 – Coulombic efficiency vs cycle number plot with coulombic efficiency values calculated from the voltage capacity graph for LFP vs Li half-cell, as shown in Figure 15. This figure highlights the expected low coulombic efficiency expected in early stages of cycling.

In Figure 16, the two cycles at C/10 and the first cycle of C/2 are shown to have lower coulombic efficiencies than those at later cycles. This can be explained once again through the formation of the SEI, where a given amount of lithium is extracted from the LFP material and deposited onto the lithium metal surface. This lithium is then able to react with the EC molecules within the electrolyte forming SEI products, therefore reducing the available lithium ions for the intercalation back into the LFP, thus decreasing the coulombic efficiencies during the initial cycles.

Finally, differential capacity vs differential voltage (dQ/dV) analysis can also be conducted to examine the electrochemical behaviour of the cell, or more specifically the reactions that occur at the active material during cycling. This analysis operates by measuring the change in capacity respective to the corresponding change in voltage and then plotting against the voltage in which it occurs. Materials undergoing lithium intercalation mechanisms usually show an increase in capacity whilst maintaining similar voltage values, thus appearing as peaks (at their respective voltages) in the dQ/dV vs voltage graph. Figure 17 shows a dQ/dV graph for an LFP/lithium metal

cell, illustrating how this graph is useful to identify the voltage values at which the (main) lithium intercalation reaction occurs.

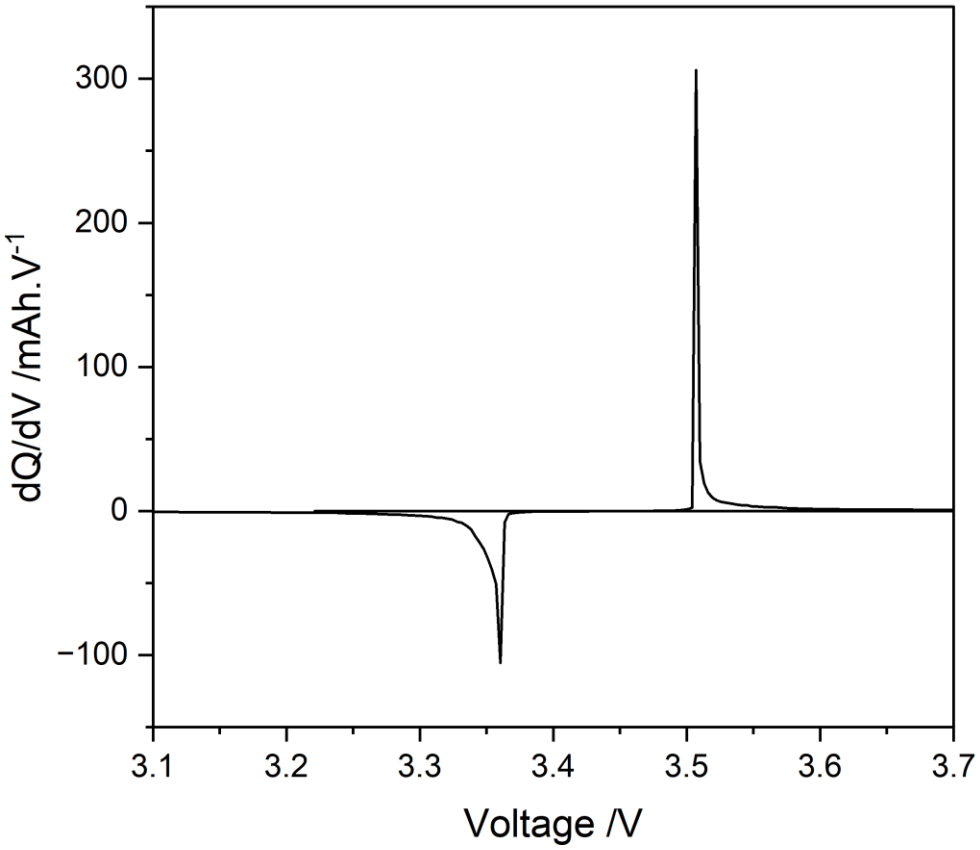

Figure 17 – dQ/dV vs voltage graph of the LFP vs Li half-cell as shown in Figure 15, where a singular peak is observed during the charge step and a corresponding singular peak for the discharge step. Each peak represents the lithium intercalation and extraction mechanism occurring at that voltage.

It is important to note that not all cells will resemble the example in Figure 17, with the graph profile changing considerably especially between materials. For example, the graphite lithium intercalation reaction occurs in three main stages, each at a different voltage thus appearing as three distinct peaks. Furthermore, peak height, area and peak voltage locations can be impacted by the degree of degradation occurring at the active material, making this type of analysis extremely useful when studying the impact of experimental variables.

These three graphs (voltage vs capacity, coulombic efficiency vs cycle, and dQ/dV vs voltage) form the core of the initial analysis of the electrochemical data as they reveal a significant amount of information on the electrochemical performance of the cell.

2.2.6 Additional Pressure Measurement Procedures

2.2.6.1 Headspace Volumes

The pressure changed caused by gas evolution from the cell is directly related to the headspace volume of the cell as shown in which was derived from the ideal gas law:

$$\Delta P = P_0 \frac{\Delta V}{V_{Cell} - \Delta V.}$$

Equation 4 – Equation to calculate the change in pressure ΔP induced by the formation of a gas volume ΔV, for a cell with a headspace volume Vcell and P0 initial pressure.

From this equation, it can be deduced that by decreasing the cell headspace volume (V_{Cell}), it is possible to increase the value of pressure change from a set gas volume. For example, the typical volume of gas produced during SEI formation on the graphite surface is approximately 2 µl of gas per mg of graphite [72], the headspace volumes within this project are approximately 2 ml and typical graphite mass from mesh electrodes is 25 mg; from these values, we can determine that the change in pressure for a would be ~ 26 mbar. If the headspace volume was then doubled in size at 4 ml, then the corresponding pressure would approximately halve to be ~13 mbar. Assuming the gas evolution would then decrease depending based on certain cell systems, it would be even more difficult to detect the pressure changes, therefore ensuring the lowest possible headspace volumes is important. The technique utilised in this project has shown to provide comparable headspace volumes to that of other modified Swagelok cells in literature [68], whilst still maintaining accessibility to a widespread audience.

Small variations in headspace volume are expected between cells, however this would also mean that comparisons of pressure measurement data from different cells need to consider the differences between cell headspace volumes. For that reason, pressure measurement data is normalised relative to each cells headspace volume to give gas volume ($mLg^{-1}_{Graphite}$) rather than pressure change ($bar.g^{-1}_{Graphite}$), using the following equation:

$$\Delta V = \frac{\Delta P . V_{Cell}}{\Delta P + P_0}$$

Equation 5 - Equation to calculate the volume of gas produced (or consumed) from changes in the internal pressure of the cell, ΔP, for a cell with a headspace volume Vcell and P0 initial pressure.

To deduce the total cell headspace volume of a cell connected to a transducer, Boyle's law was utilised, where the initial and final cell pressures and volumes are related assuming the

temperature is constant: $P_1V_1 = P_2V_2$. By using a combination of known cell parts and placing the cell system under known pressures, it is possible to deduce the unknown cell part volumes. Here in this section, the process of how this was done is described.

Firstly, the whole structure was divided into the transducer component and the cell component (Figure 18 (3A) and (3B) respectively). Once the two unknown volumes were determined separately, they were added together to yield the total cell headspace volume of a cell connected to a pressure transducer.

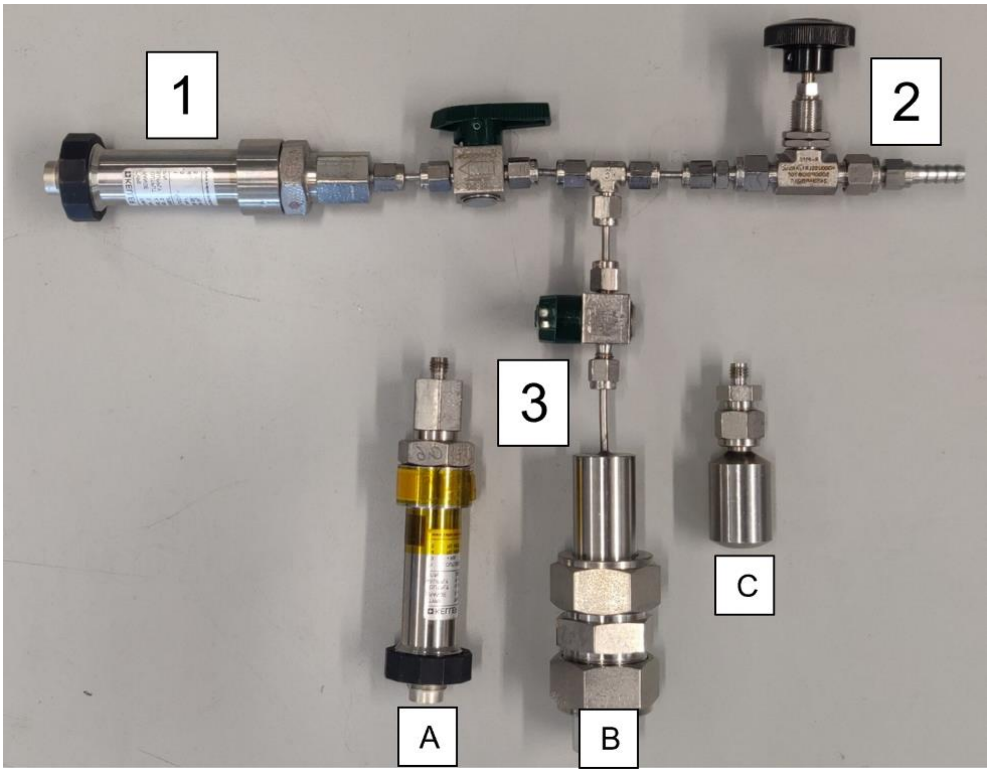

Figure 18 – Photograph showing the equipment needed for headspace volume measurements. Equipment parts are labelled: (1) Reference transducer, (2) vacuum line, (3A) pressure transducer, (3B) cell body, (3C) known volume metal bottle.

The image shown in Figure 18 depicts the equipment set up used to conduct the volume measurements. Further detailed explanation of how the evaluation of total cell headspace volume was determined can be found in Figure 81 in the appendix, here we will only briefly describe the experimental process of volume and pressure measurements. Figure 19 also illustrates the steps taken during this experiment.

Steps taken:

1. The metal bottle (Swagelok SS-4CS-TW-10, Figure 18 (3C)) was fitted with a Swagelok adaptor (SS-600-6-2) and weighed. The bottle was then filled with water until full and then was weighed again. By using the density of water, the volume of the bottle was determined to be 10.94 ml.

2. The known volume bottle was then attached to the set up shown in Figure 18.
3. System was then allowed to equilibrate for ~1 minute, so that the reference transducer and the metal bottle would be at atmospheric pressure (~1 bar). Figure 19 – step 1.
4. After the system has equilibrated, the valve to the bottle is closed and the valve to the vacuum line is opened (~1 min), such that the reference transducer is then placed under vacuum. Figure 19 – step 2.
5. The vacuum line valve was then closed to create a system with two containers at different pressures. Figure 19 – step 3.
6. The bottle valve was then opened to allow the system to equilibrate once again. Figure 19 – step 4.

The data gathered in the steps above were then used to deduce the volume of the reference transducer. Once this was done, steps 3 – 6 were repeated after replacing the bottle with either the unknown volume transducer or the unknown volume cell. An example of the pressure data collected during these experiments can be seen in Figure 20. 3 repeats were conducted for each cell component with the average of the repeats used as the cell headspace volume.

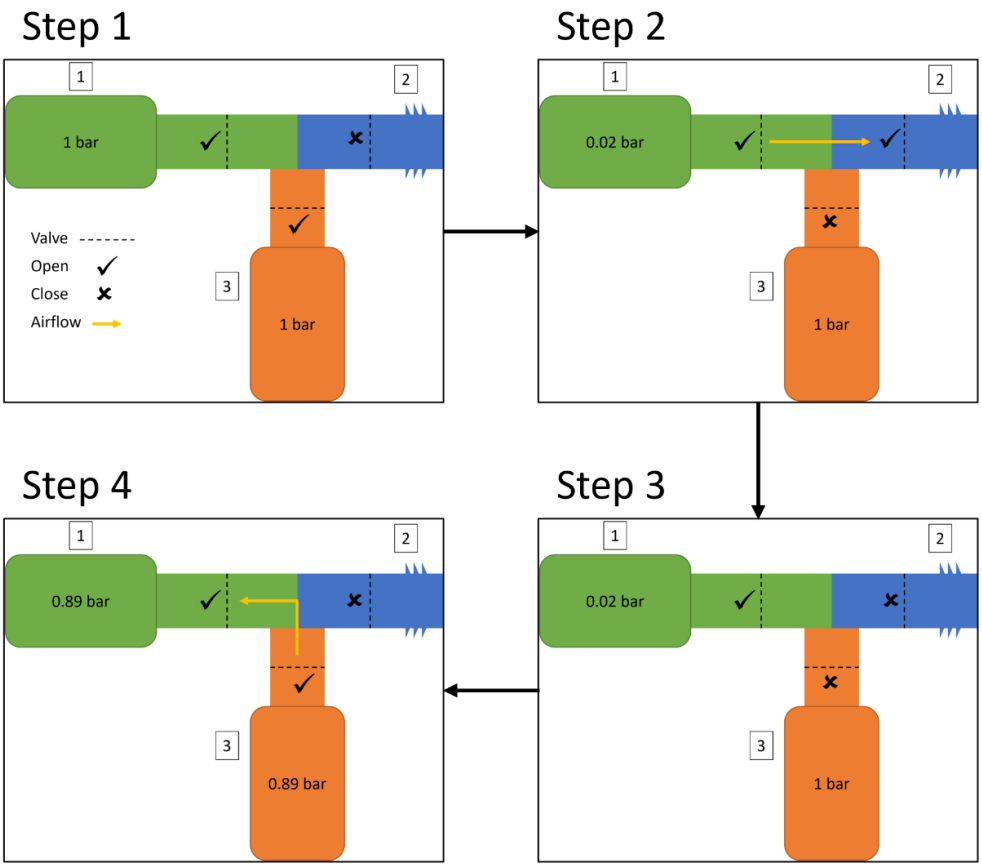

Figure 19 – Schematic showing the steps taken within headspace volume measurement experiment. Labels 1,2 &3 correspond to the parts shown in Figure 18. Step 1 represents system at atmospheric pressure, step 2 represents evacuation of the reference transducer, step 3 represents sealing of the system, and step 4 is equilibration of the cell/transducer/metal bottle.

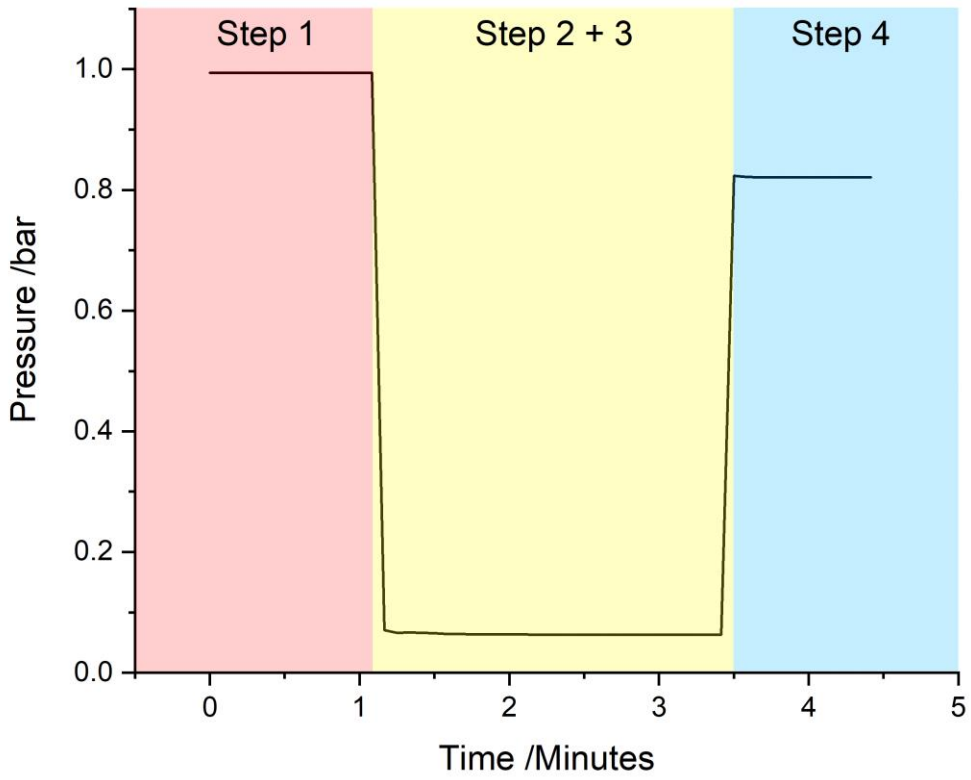

Figure 20 – Example of pressure data taken from headspace volume measurements, where the values can be used in Equation 5 to determine the headspace volume of the cell. Step labels correspond to those in Figure 19.

When calculating the final headspace volume, one must also take into consideration of the electrolyte volume added to the cell, therefore the 0.6 ml of electrolyte volume is subtracted from the calculated headspace volume of the cell set up.

During the project, new cell bodies and transducers were introduced to replaced damaged or aged parts, therefore headspace volumes were undertaken once every 3 months or whenever a part was changed (whichever came first). Small variations in headspace volume were observed not only between different cells but also in the same cells over time, this is to be expected due to general wear and tear in addition to inherent differences in the cell components (some had O-rings, some had been machined to different tolerances). These small variations however do not have a significant impact of the data obtained and do not change the overall gas evolution trends observed.

2.2.6.2 Normalisation of data

The pressure transducer also contains a temperature sensor alongside a pressure sensor, allowing the monitoring of both the pressure and temperature of the cell. This is advantageous because despite the cell being in a climatic chamber, small temperature variations within the cell

can still be observed which consequently impacts the pressure values recorded. To account for this, the pressure measurement data was corrected using Equation 6.

$$Pressure\ (corrected) = Pressure\ (experimental) \times \frac{298\ K}{Temperature\ (experimental)}$$

Equation 6- Equation to calculate the corrected pressure from experimental pressure and temperature data.

As the temperature variations are relatively small (approximately 0.2 °C), the corrected data does not show drastic differences from the recorded data, however it is still visible and distinctive enough to be relevant. Comparison of a temperature corrected vs raw data pressure measurement can be seen in Figure 81 within the appendix.

The pressure changed caused by gas evolution from the cell is directly related to the headspace volume of the cell as shown in Equation 4 which was derived from the ideal gas law:

$$\Delta P = P_0 \frac{\Delta V}{V_{Cell} - \Delta V.}$$

Equation 7 – Equation to calculate the change in pressure ΔP induced by the formation of a gas volume ΔV, for a cell with a headspace volume Vcell and P0 initial pressure.

From this equation, it can be deduced that by decreasing the cell headspace volume (V_{Cell}), it is possible to increase the value of pressure change from a set gas volume. For example, the typical volume of gas produced during SEI formation on the graphite surface is approximately 2 µl of gas per mg of graphite [72], the headspace volumes within this project are approximately 2 ml and typical graphite mass from mesh electrodes is 25 mg; from these values, we can determine that the change in pressure for a would be ~ 26 mbar. If the headspace volume was then doubled in size at 4 ml, then the corresponding pressure would approximately halve to be ~13 mbar. Assuming the gas evolution would then decrease depending based on certain cell systems, it would be even more difficult to detect the pressure changes, therefore ensuring the lowest possible headspace volumes is important. The technique utilised in this project has shown to provide comparable headspace volumes to that of other modified Swagelok cells in literature [68], whilst still maintaining accessibility to a widespread audience.

Small variations in headspace volume are expected between cells, however this would also mean that comparisons of pressure measurement data from different cells need to consider the differences between cell headspace volumes. For that reason, pressure measurement data is normalised relative to each cells headspace volume to give gas volume ($mLg^{-1}_{Graphite}$) rather than pressure change ($bar.g^{-1}_{Graphite}$), using the following equation:

$$\Delta V = \frac{\Delta P . V_{Cell}}{\Delta P + P_0}$$

Equation 8 - Equation to calculate the volume of gas produced (or consumed) from changes in the internal pressure of the cell, ΔP, for a cell with a headspace volume V_{cell} and P_0 initial pressure.

2.2.6.3 Leak Testing

As previously mentioned, leaks within the cell are highly undesirable as they immediately invalidate any pressure measurement data obtained. As these cells require a significant amount of time and effort to manufacture and cycle, it is imperative to reduce the likelihood of leaks within the cell. Unfortunately, during initial testing, it was found that the Swagelok cell parts were highly susceptible to leaks if not handled properly, creating the need for new methodologies for identifying sources of leaks and ensuring the airtightness of the cell. In this section, methods of detecting and reducing leaks are discussed. It should be noted that despite diligent efforts, it was impossible to eliminate leaks within all cells completely, however by following strict protocols, the frequency of leaking cells each week was reduced greatly.

It is first important to understand how an airtight seal is created within the Swagelok cells (assuming all parts and connections are in good condition). The seal is primarily formed using the nylon ferrules that wrap round the current collector. These ferrules serve two purposes; firstly, they hold the current collector in a rigid manner such that the current collector does not tilt and touch the cell body or the cell nuts. Secondly, when the ferrules are compressed during the tightening of the nuts onto the cell body, they press against the cell body forming a seal between the current collector and the cell body, hence why the need for a new tightening protocol as tightening by hand was often insufficient to produce a good seal. Aside from major causes of leaks such as broken connections or damage of cell parts, most leaks within the Swagelok cells are expected to arise from the disturbance of the ferrules, specifically the contact between ferrule and current collector or ferrule and cell body. As such, ferrules are routinely inspected and replaced regularly, especially if any sign of damage or wear and tear is seen.

The easiest way to determine if a leak is present within the cell prior to cycling, is through the same set up used in the headspace volume calculations. The cell is attached to a vacuum line in the same manner and the entire set up is subjected to a vacuum, if the pressure holds then the cell is air-tight, however if over time it changes then a leak is present. Once a leak is found, all the connections are tightened again, and the test is repeated; if the leak persists then further methods need to be employed. Examples of pressure data from a leaking cell and a non-leaking

cell can be seen in Figure 21 and Figure 22 respectively, where in the figures, Step 1 - cell parts have equilibrated to atmospheric pressure, Step 2 - components are placed under pressure, Step 3 - Vacuum line valve is closed and if no leak is present, then the pressure value will remain the same however if a leak is present, then the pressure will return to atmospheric values.

In most scenarios, the leak is caused simply by a damaged ferrule, therefore replacing the ferrule ordinarily resolves the leak. However, there are on occasions other sources of leaks that are not inherently clear; to investigate these illusive sources, the cell (not including the transducer) can be connected to a pressurised gas line (argon) and then submerged into a transparent container of water. When the pressured gas enters the cell, bubbles would then appear where the source of the leaks were. This method allowed the identification of a few more potential sources of leaks, such as hairline cracks within the soldering of the modified current collector (rectified by resoldering or replacement) and new current collectors that were manufactured with small grooves on the surface therefore creating insufficient contact between the ferrule and the current collector (rectified by polishing with sandpaper or replacement).

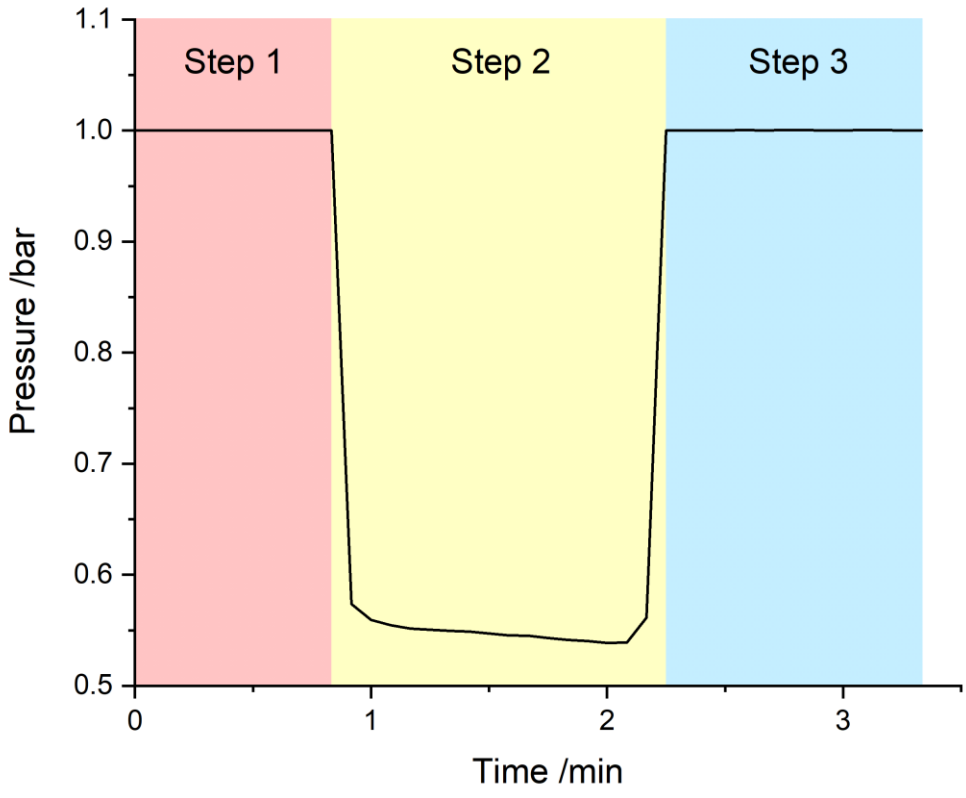

Figure 21 - Pressure data obtained from leak testing showing a cell with a leak present. Step 1 shows the cell at atmospheric pressure, step 2 is the cell subjected to vacuum, and step 3 is where the vacuum line is sealed. In step 3, since there is a leak, the cell returns to atmospheric pressure.

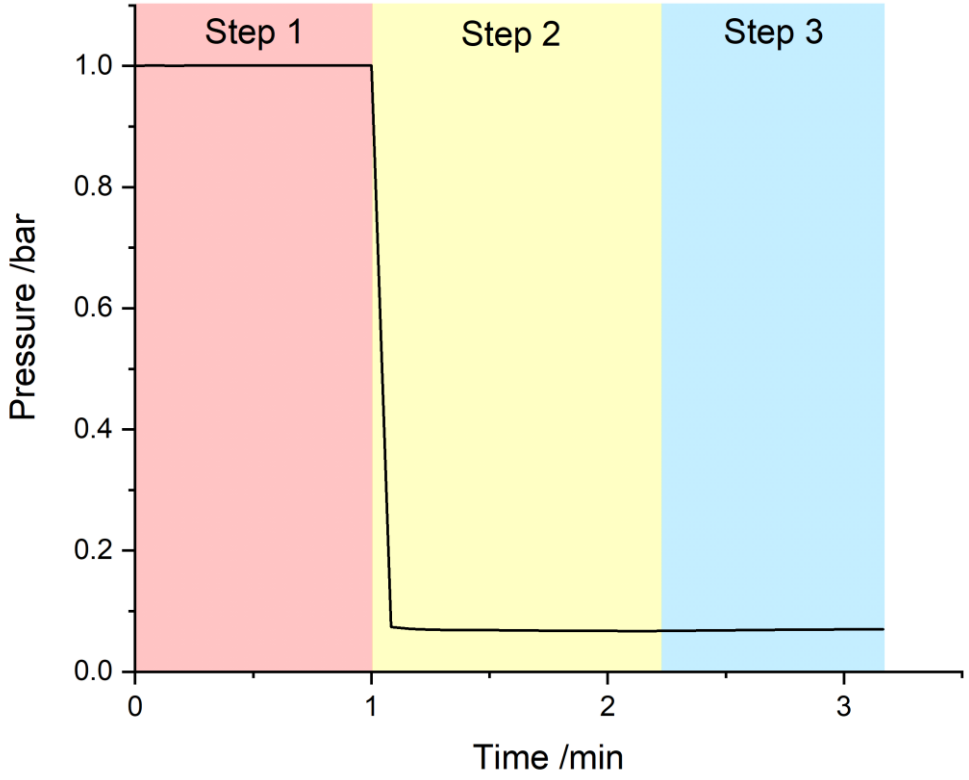

Figure 22 - Pressure data obtained from leak testing showing a cell with NO leaks present. Step 1 shows the cell at atmospheric pressure, step 2 is the cell subjected to vacuum, and step 3 is where the vacuum line is sealed. In step 3, since there is NO leak, the cell retains its vacuum thus giving a lower pressure reading.

During the experiments to be discussed later in this chapter, records of which cells exhibited leaks were made to track which cell parts were the likely culprits of leaks. Cell parts are not interchanged between one another, therefore if a set of cell parts show leaks consistently week after week, then those parts would be subjected to the leak tests.

During the experiments to be discussed later in this chapter, records of which cells exhibited leaks were made to track which cell parts were the likely culprits of leaks. Cell parts are not interchanged between one another, therefore if a set of cell parts show leaks consistently week after week, then those parts would be subjected to the leak tests.

2.3 Methodology Optimisations and Adaptations

The original experimental methodology that was used during the early periods of this project differed significantly to what is seen in the final methodology. The original methodology was found to be inadequate for consistent and reliable data, therefore extensive work was dedicated towards optimisations to create an improved methodology.

The need for an optimisation process was clear during the first initial set of LFP/lithium half cells, where the electrochemical data gathered showed promising data however was very inconsistent. This theme continued throughout the project, where unexpected electrochemical data from cells led to changes in methodology until reliable and consistent results were achieved. During this optimisation process, various other electrochemical cells were tested such graphite/lithium half cells, graphite/LFP full cells, and graphite/LFP pressure measurement cells. Here, the optimisations and adaptations made at each stage of the process will be discussed in chronological order.

2.3.1 Addressing Poor Electrochemical Performance

Before discussing the optimisations that were made, it is first necessary to establish the original electrode production methodology used prior to the optimisations.

Firstly, dry powders (graphite/LFP, carbon black and PVDF) and solvent (NMP) were added to a glass vial and homogenised using an Thinky Planetary Mixer (using a vial-compatible adapter) yielding an electrode slurry. The substrate foil was then gently polished using sandpaper (3M™ Wetordry™ Abrasive Paper Sheet 734) and then sonicated for 20 mins. The slurry was then deposited onto the substrate a Dr. Blade Coater to give an electrode coating. This coating was then dried in a vacuum oven for overnight.

Initial experiments utilised LFP/lithium metal half cells using electrodes made using the above electrode production methodology. Data from these cells showed that it was possible to obtain desirable electrochemical performances, such as first cycle discharge capacities ≥ ~150 $mAhg^{-1}$, first cycle coulombic efficiencies ≥90% with the later cycles having ≥97%, and the presence of a clear single peak in the dQ/dV analysis representing the lithium intercalation mechanism occurring at a singular potential. However, a key point to note is that this desirable electrochemical performance only appeared in 17% of the cells (2 out of 12 cells total), with the other cells exhibiting poor electrochemical behaviours such as potential profile anomalies, poor first cycle discharge capacities and poor first cycle coulombic efficiencies. This highlighted a need for optimisation of the overall methodology.

The initial hypothesis was that inexperience with the cell assembly and electrode production were the source of the issues. To investigate this, the entire experimental procedure was repeated by a more experienced colleague, Ben Rowden. Electrochemical performance from cells made by Ben Rowden were then compared with my previous results. A common factor that was present in all poor performing cells was a low first cycle coulombic efficiency (<90%), indicating the presence of an unwanted side reaction that was either increasing charge capacity

through redox reactions or decreasing discharge capacity by interfering with the lithium insertion into the LFP material. This therefore became the metric in determining the success of the cells. The comparison between cells showed negligible differences between the cell manufacturers, with Liam Lu cells possessing average first cycle efficiencies of 85.09 ±5.75% (12 cells) and Ben Rowden cells possessing 83.26 ±7.82% (10 cells), as shown in Figure 23. Additionally, the number of cells that exhibited desirable electrochemical performances remained low, with only 10% of cells made by Ben Rowden (1 out of 10 cells total) being successful, compared to 17% of the Liam Lu cells (2 out of 12 cells total). It was therefore concluded that the source of the poor electrochemical performance was not likely to be caused by human errors stemming from inexperience, but instead from a factor inherent to the methodology or cell parts.

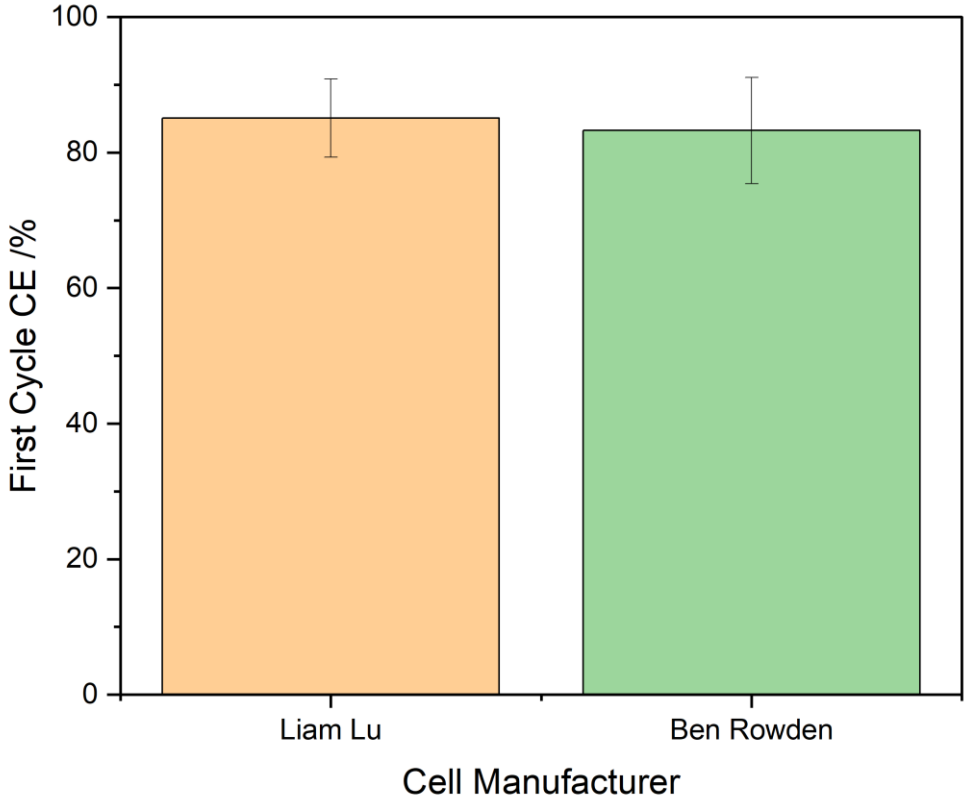

Figure 23 - Comparison of first cycle efficiencies between initial LFP vs Li Swagelok half cells made by Liam Lu and Ben Rowden to determine whether user error was responsible for low success rate for cells. Errors calculated from standard deviation of 12 Liam Lu cells and 10 Ben Rowden Cells.

Another possible factor that was thought to impact the cell performance was the presence of corrosion products within the cell parts, especially the cell body. This theory was corroborated with the fact that the stainless-steel cell bodies were not brand new and had previously been used by other members of the research group for other studies, therefore corrosion could not be

ruled out. Additionally, literature has shown that corrosion of cell parts can actively impact the reliability of electrochemical data [112] [113].

To check this theory, the impact of stainless-steel corrosion within the cell had to be minimised. To do this, the stainless-steel cell body was replaced with a plastic counterpart, thus eliminating the largest source of stainless-steel in the cell. Repeats of electrochemical cycling of LFP/Li half cells were done but now in a plastic cell body with the same cycling protocols and conditions and the stainless-steel body cells.

An initial analysis of the results revealed that indeed by reducing the presence of stainless-steel and therefore possible corrosion products, allowed for an increase in first cycle efficiencies in all cells (8 total cells) to >90% and a significant improvement to the reproducibility as shown in the decrease in standard deviation (average first cycle coulombic efficiency: 95.17 ±0.61%), as shown in Figure 24.

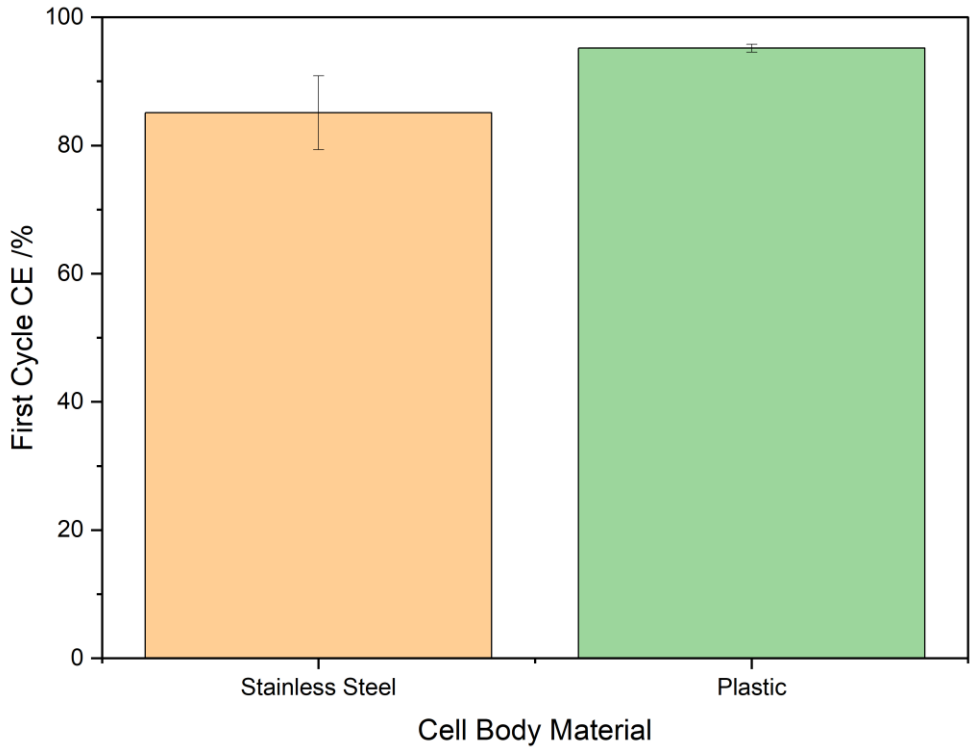

Figure 24 - Comparison of first cycle efficiencies between initial LFP vs Li Swagelok half cells with either stainless-steel or plastic cell body, to determine the impact of stainless-steel corrosion on electrochemical performance. Errors calculated from standard deviation of 12 stainless-steel cells and 10 plastic cells.

However, when analysing the first cycle discharge capacities, all 8 cells did not reach the minimum target value of 150 $mAhg^{-1}$, indicating that it was likely that further factors in addition to corrosion were affected the cell performance. Comparing the capacity values with those in the

previous stainless-steel cells, an overall decrease in average capacity is observed with plastic cells having 136.85 ±1.85 $mAhg^{-1}$ whilst stainless-steel cells achieved a higher 144.99 ±2.94 $mAhg^{-1}$, as shown in Figure 25. This indicates that whilst reducing the impact of stainless-steel parts within the cell can improve certain aspects of the electrochemistry, a common factor between the plastic and stainless-cells cells is still present, which is negatively impacting the performance of the cell.

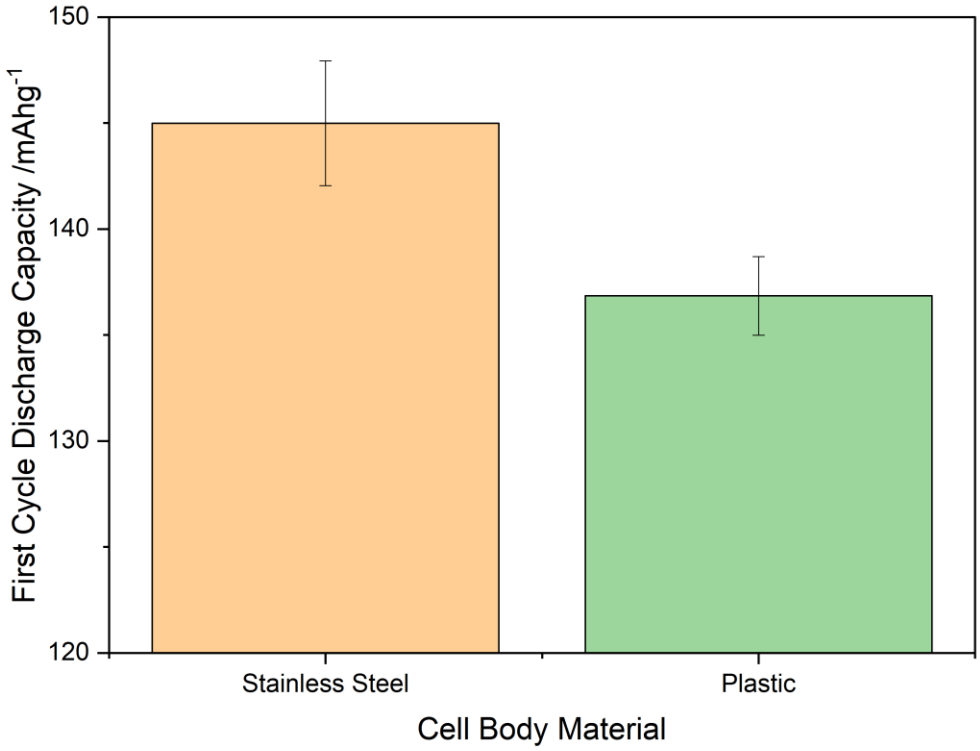

Figure 25 - Comparison of first cycle discharge capacity between initial LFP vs Li Swagelok half cells with either stainless-steel or plastic cell body, to determine the impact of stainless-steel corrosion on electrochemical performance. Errors calculated from standard deviation of 12 stainless-steel cells and 10 plastic cells.

Other sources of contamination were also considered, for example on the plastic cell bodies or on the other remaining cell parts such as the current collectors or electrodes. Unlike the stainless-steel cell parts, the plastic cells were brand new and were thoroughly cleaned via sonication therefore unlikely to have contaminants present that could cause this decreased discharge capacity. The remaining parts such as current collectors, cap and spring, may have been a source of contamination, however there was not a feasible method of optimisation as these parts were irreplaceable. Instead, the upmost care was taken to ensure these parts were clean such as diligent polishing and sonication. Finally, when considering the electrodes present in the cells, it seemed very possible that the electrode could be the limiting factor to the cell performance and there were many avenues to explore with regards to optimisation. a

Addressing the possibility that the electrode was a limiting factor, three key changes were made to the electrode production methodology:

1. Changing the mixing container that was used to holds the powders and solvent, from a vial and adapter to a standard Thinky mixer pot.
2. No longer polishing the aluminium foil with sandpaper, instead thoroughly wiping with Kimtech tissues and isopropanol.
3. Agitating the dry powders with a glass rod before the addition of NMP solvent.

The switch from vial to Thinky pot was thought to help with increasing homogeneity of the electrode slurry. The use of the glass vial was remnant of previous methodologies from previous work in the group, where mixing was done using equipment such as an IKA T23 digital Ultra Turrax which was only compatible with glass vials. Whilst mixing using a vial in a Thinky mixer was possible, the recommended procedure from the manufacturers was to use their Thinky pots and was thought to allow optimal mixing. Furthermore, by using vials, it was suspected that errors in powder weight measurements may have occurred, as the glass vials were incredibly difficult to transfer powders into.

Removing the polishing step of the aluminium foil substrate was deemed necessary to ensure a consistent loading of the electrode slurry onto the foil, as polishing the surface may have led to an inhomogeneous substrate surface and thus larger variations in loading.

Finally, mixing the dry powders with a glass rod prior to the addition of NMP solvent was introduced to reduce the risk of PVDF agglomeration, which would again lead to better homogeneity of the slurry. This was implemented as on several occasions, during the coating step of the electrode production, very small lumps were visible. These lumps were theorised to be PVDF agglomerates, which if that were the case could mean poor integration of PVDF elsewhere in the coating and thus leading to decreased electrochemical performance.

With these changes implemented, new electrodes were produced and cycled in plastic cells, again under the same cycling protocols and conditions. Results from the cells using the optimised cell production methods (12 cells total) showed an increase in first cycle discharge capacity, obtaining 153.66 ±1.09 $mAhg^{-1}$ (compared to the original 136.85 ±1.85 $mAhg^{-1}$), which satisfies the minimum capacity targets. Graph comparing the first cycle discharge capacity of the two methodologies can be seen in Figure 26. Additionally,

Of the cells cycled, 92% of cells (11 out of 12 total cells) successfully satisfied all the electrochemical performance targets, further emphasising the success of the optimisation changes.

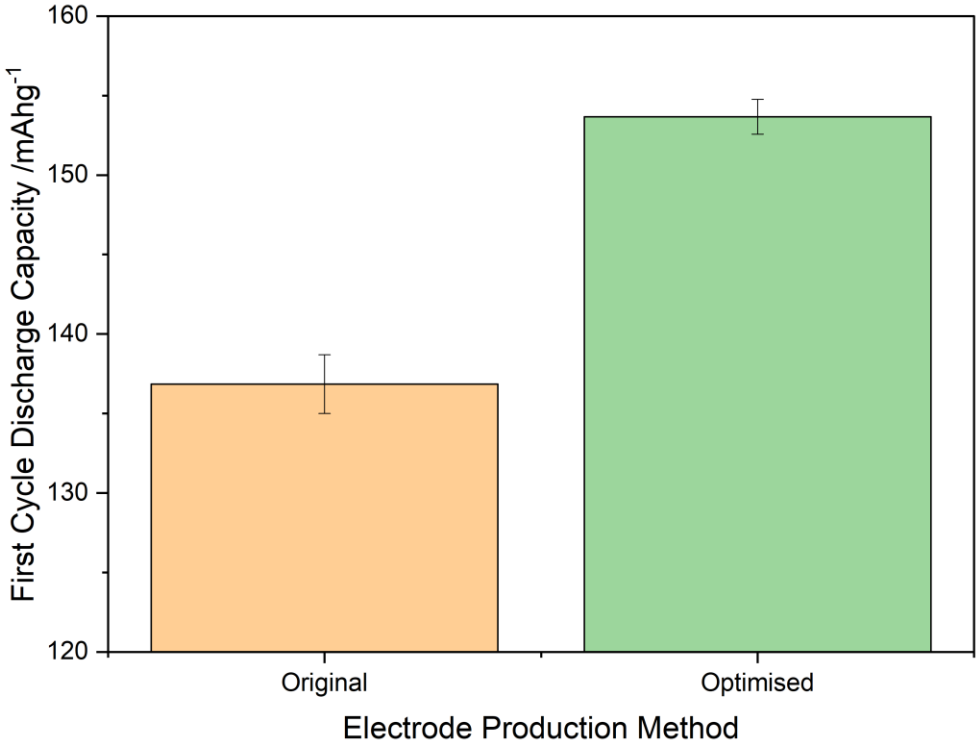

Figure 26 - Comparison of first cycle discharge capacity between LFP vs Li plastic Swagelok half cells with electrodes made using the original and optimised production methodology. Errors calculated from standard deviation of 10 original cells and 12 optimised cells.

These promising results were achieved with contributions from both the stainless-steel corrosion considerations and the electrode methodology changes, however it is difficult to determine the relative impact of these two optimisation steps. To investigate this further, stainless-steel cell were cycled using electrodes manufactured with the new methodology. The electrochemical performance of these cells once again met the target values for both the first cycle efficiency and discharge capacity, with values of 96.71 ±0.19% and 149.98 ±0.43 $mAhg^{-1}$ respectively. When compared to the plastic cell counterpart, there is negligible differences in first cycle efficiencies with both achieving ~97%, whilst a minor decrease of ~3 $mAhg^{-1}$ was observed in the first cycle discharge capacities of the stainless-steel cells. This was unexpected as the re-introduction of the stainless-steel cell body was predicted to decrease the first cycle efficiency whilst also increasing the discharge capacity.

At the time of writing, it is still unclear why this was the case, however despite being unable to elucidate the exact reason for this odd behaviour, the goal of optimising the methodology to yield LFP/Li half cells with good electrochemical performance was achieved.

2.3.2 Addressing Slow Gas Transfer

The next optimisation that was made was the development of pressure measurement adapted electrodes. For the pressure transducer to function in an optimum way, rapid gas transfer between the main cell and the pressure transducer was required. Initial tests (described later in section 2.2.6.1) with the pressure transducer cells showed that the use of un-perforated electrodes would cause the delayed transfer of gas within cells. This was demonstrated by the very slow changes of pressure over time, where cells with the electrode would take 12+ hours before the pressure would stabilise whilst cells with no electrodes showed almost instantaneous stabilisation. Upon further investigation, it was found that during the assembly of the cell, the electrode foil substrate would block the tubing opening thus impeding gas flow.

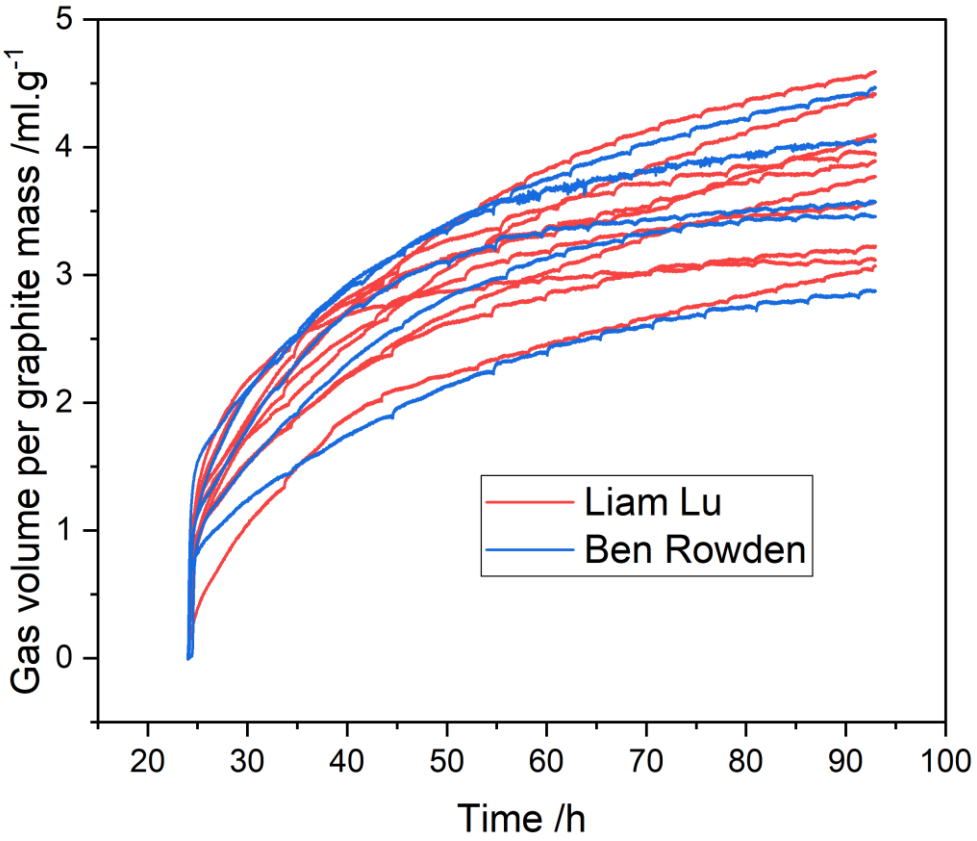

Figure 27 - Gas volume produced over time in graphite vs Li half cells with graphite electrodes coated onto copper mesh substrate. Comparison between electrodes produced by Liam Lu (red line) and Ben Rowden (blue line) to demonstrate reproducibility of pressure measurement results.

To remedy this, electrodes were coated on thin copper mesh with <0.05 mm holes (Boegger Industech Limited) with the hypothesis that gas would easily permeate through the mesh holes to the transducer. Cells with copper mesh electrodes demonstrated that they were able to show comparable pressure measurement data to similar experiments conducted by a colleague, Ben

Rowden, as shown in Figure 27. This figure shows the pressure measurement cells manufactured by me (red data labelled Liam Lu) and cells manufactured by Ben Rowden (blue data labelled Ben Rowden), both using copper mesh electrodes, highlighting the reproducibility of the cell set up.

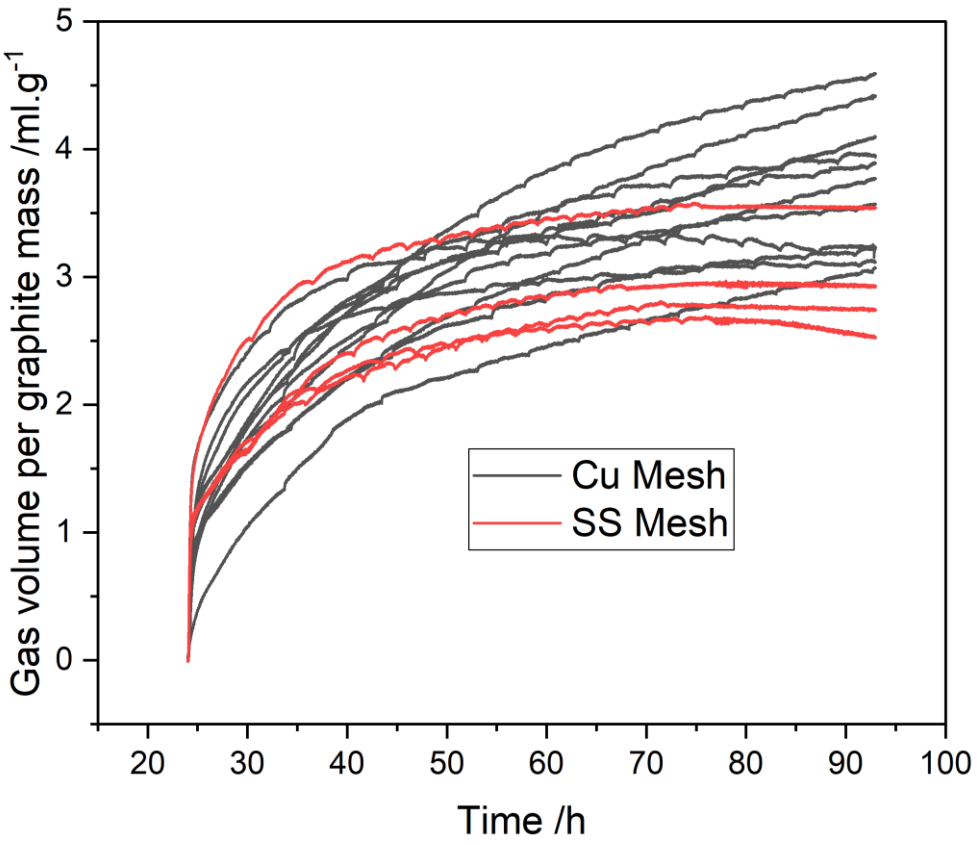

Figure 28 – Gas volume produced over time in graphite vs Li half cells with graphite electrodes coated onto copper/stainless-steel mesh substrate. Comparison between the different electrode's substrate materials shows the replacement of copper mesh with stainless-steel mesh does not significantly impact the pressure measurement.

However, it was theorised that using copper mesh as an electrode substrate may lead to copper dissolution within the cell [114, 115], therefore it was decided to transition to using stainless-steel mesh (The Mesh Company, 316 stainless steel) as the substrate. Additionally, during the coating of the copper mesh, difficulties were encountered, where the large holes in the mesh caused the substrate to adhere to the work surface under the mesh as the graphite slurry was able to penetrate past the mesh and dry between the substrate and the work surface. This meant that occasionally when removing the coating from the work surface, the coating would crack and be damaged as the coating would be stuck to the work surface. To prevent this, mesh with a smaller hole size of 0.026 mm was chosen with the hopes of preventing the graphite slurry from permeating through the mesh as much.

The use of the new stainless-steel mesh once again allowed effective gas transfer, as shown in Figure 28, where stainless-steel mesh exhibited similar gas evolution profiles to the copper foil mesh cells. No significant pressure measurement differences were observed between the substrate materials, highlighting that the replacement of copper with stainless as the substrate material would not have any notable impact on studying gas evolution within the cells. The small differences such as the increased gas evolution in some copper mesh cells or small differences in profile shape can be attributed to the inherent variability of the gas evolution measurements.

However, upon analysing the electrochemical data from cells using stainless-steel mesh, it was clear that the cells had sub-par performance. Firstly, the first cycle discharge capacity for stainless-steel mesh cells were found to be lower than that of the copper foil and copper mesh cells, as shown in Figure 30. In this figure, we see that copper foil and mesh have comparable values of 336 and 339 $mAhg^{-1}$ respectively, whilst stainless-steel mesh has significantly lower value of 211 $mAhg^{-1}$. Evidently, the use of stainless-steel mesh is reducing the amount of lithium that is able to be extracted from the active material, leading to a lower first cycle discharge.

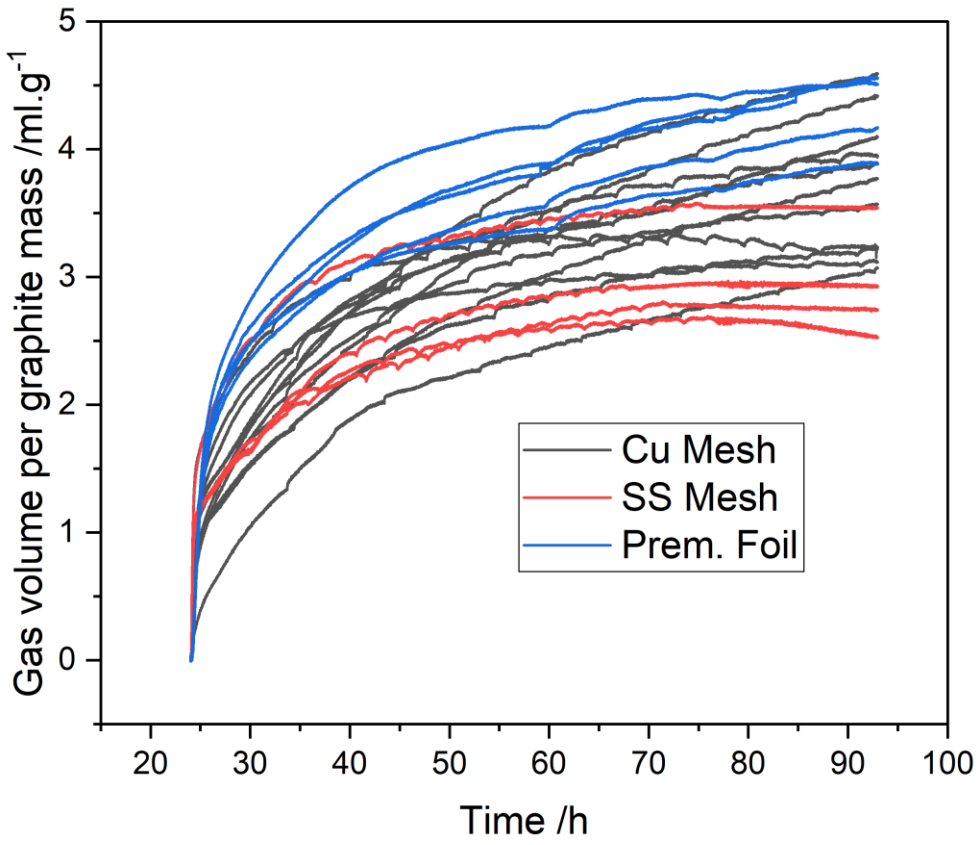

Figure 29 - Gas volume produced over time in graphite vs Li half cells with graphite electrodes coated onto copper/stainless-steel mesh substrate and premade foil electrodes. Comparison between the mesh electrodes and the premade foil electrodes highlights the ability for premade foils to reproducibly give pressure measurement data.

To investigate further, the first cycle coulombic efficiency was compared between the cells, as shown in Figure 31. Here, the efficiency values between all the cells are very comparable, with copper foil achieving 95%, copper mesh 93% and stainless-steel mesh 92%. The very minor difference between the copper foil/mesh and stainless-steel mesh implies that the loss of discharge capacity is not linked to increased side reactions occurring at the graphite surface.

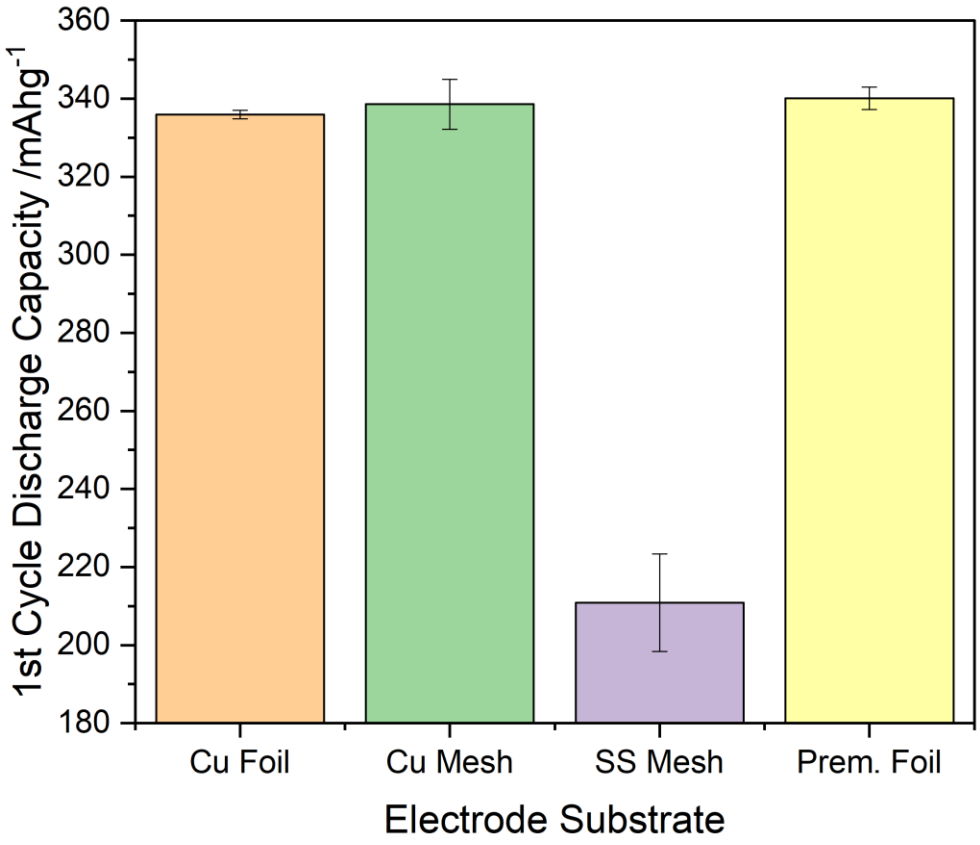

Figure 30 – Comparison of first cycles discharge capacity in graphite vs lithium metal half cells with different electrode substrates for the graphite electrode. Error bars calculated from the standard deviation of 8 cells for each electrode substrate

Analysis of the dQ/dV data, as shown in Figure 32, reveals that the stainless-steel mesh electrodes do not undergo the full reaction of lithium intercalation and extraction. From Figure 32, we see that copper foil and copper mesh both show the expected three peaks that correspond to the completion of lithium intercalation/extraction into graphite, however the stainless-steel mesh only shows one peak during the charging stage and two peaks during the discharge stage. This lack of the remaining peaks highlights that during charging, fewer lithium ions maybe intercalating into the graphite, therefore during discharge, fewer lithium ions are available for extraction, thus explaining the decreased discharge capacities. Furthermore, the decreased peak

heights for stainless-steel mesh cells also indicate that less charge was during the intercalation stages, which again supports the theory that the charging reactions are not being completed.

It is unclear what the cause of the poor electrochemical performance is for the stainless-steel electrodes. As seen in Figure 31, the high coulombic efficiencies suggest that the poor lithium intercalation is not caused by the presence of unwanted side reactions. It is not common for graphite to be coated onto stainless-steel substrates in lithium-ion battery research, therefore there is a lack of literature that describes the electrochemical effects of doing so. Furthermore, the possibility of errors in making the graphite slurry could also have caused the poor electrochemical performance.

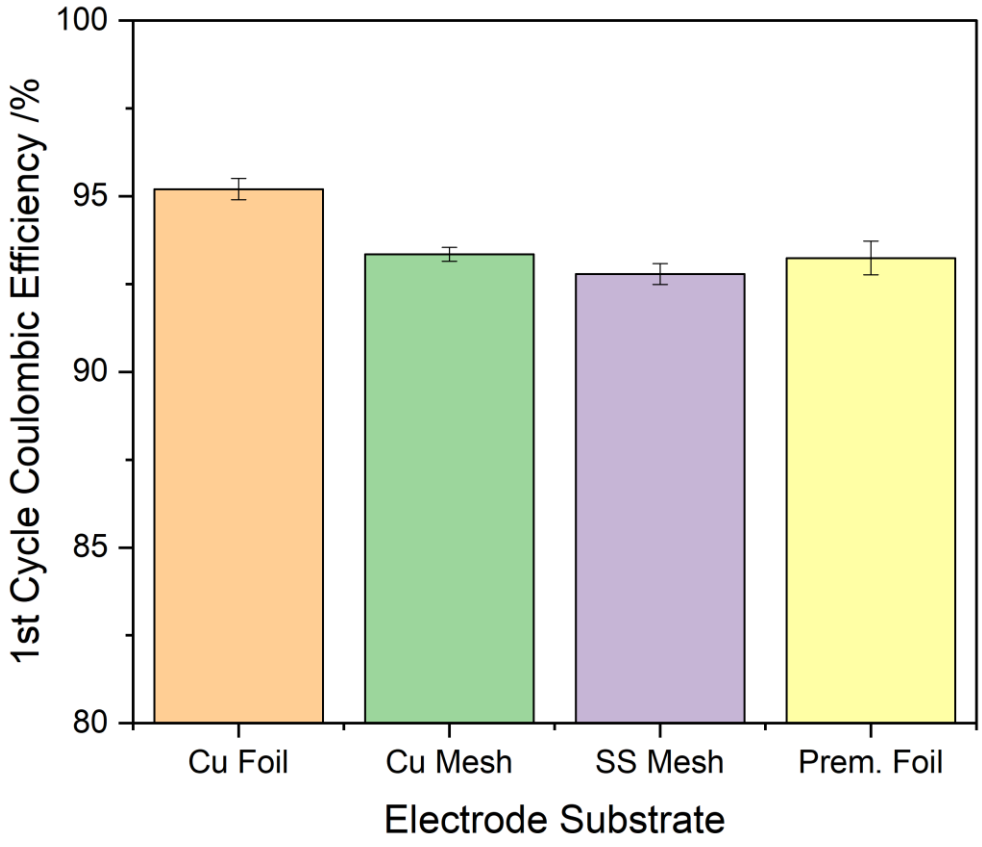

Figure 31 – Comparison of first cycles coulombic efficiency in graphite vs lithium metal half cells with different electrode substrates for the graphite electrode. Error bars calculated from the standard deviation of 8 cells for each electrode substrate

Following the poor electrochemical performance of stainless-steel mesh electrodes, another form of pressure measurement adapted electrode was required. Industry standard graphite electrodes, produced by LiFun Technology Corporation, were obtained through partners within The Faraday Institution. These electrodes are made with a high-performance graphite powder (Kaijin AML400) and were used previously in Jeff Dahn's group [116, 117]. The advantage of using premade industrial electrodes is mainly the confidence in the quality of the electrodes as it's

use has already been documented in the literature [116, 117], thus proving that achieving good electrochemical performance is possible.

These electrodes however, similar to the initial copper foil electrodes, were not adapted for pressure measurements. To rectify this, the electrode was perforated with a 2 mm diameter hole in the center of the electrode using a hand punch, thus providing a direct opening for gasses within the cell stack to reach the transducer. This was clearly effective as it again allowed gas evolution data to be obtained that was not too dissimilar to that obtained with copper mesh and stainless-steel mesh, as shown in Figure 29.

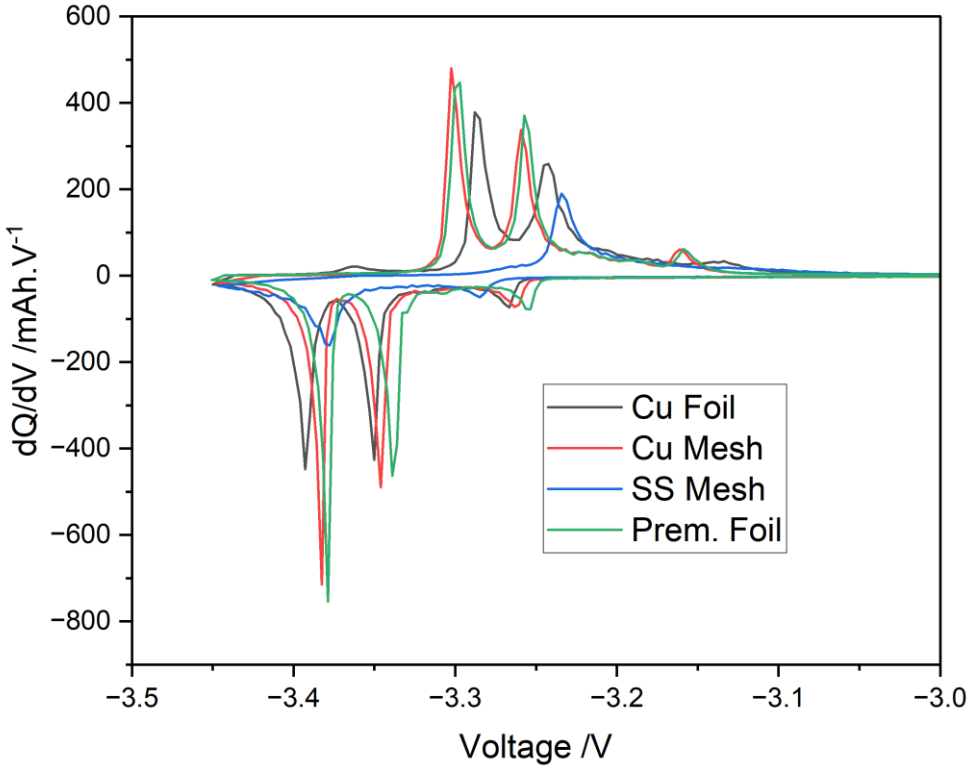

Figure 32 – Comparison of dQ/dV vs voltage data in graphite vs lithium metal half cells with different electrode substrates for the graphite electrodes.

The electrochemical performance also significantly improved in comparison to the stainless-steel mesh electrodes, where in Figure 30, we see that the premade foil was able to achieve first cycle discharge capacity of 340 $mAhg^{-1}$ which is very similar to copper foil and copper mesh cells. Furthermore, Figure 31 shows that the premade foil cells are also able obtain similar first cycle coulombic efficiencies of 93%, again highlighting a lack of side reactions that are occurring. Finally, Figure 32 shows the return of the three peaks that are associated with lithium intercalation into the graphite, with each peak having comparable peak heights which indicate similar amount of charge passing during the reactions. All the aforementioned data suggests that the use of premade electrodes is adequate for pressure measurement investigations.

To summarise the premade electrode to allows pressure measurement data to be collected, achieves good electrochemical performance, and also provides reliability due to the elimination of errors during electrode manufacturing. These factors together meant that the premade graphite electrodes were used for the remainder of the project for gas evolution investigations.

2.3.3 Summary of Optimisations and Adaptations

During the initial stages of the project, numerous optimisation steps were taken to allow desirable electrochemical performance and gas evolution data to be collected.

From the electrochemical performance optimisations, adjusting the electrode manufacturing methodology proved to be the most impactful, drastically improving reproducibility and electrochemical performance. Whilst investigations into human error during cell assembly and stainless-steel corrosion were not as fruitful, they were nonetheless useful in the development subsequent optimisations.

The gas evolution optimisations consisted of investigating various electrodes substrates that allowed effective gas transfer between the cell stack and the pressure transducer. Firstly, copper mesh was investigated, which was then replaced with stainless-steel mesh, and then finally with perforated premade copper foil electrodes. The copper mesh proved to be capable of allowing effective gas transfer between the cell stack and the pressure transducer, however, worries regarding copper dissolution led the use of stainless-steel mesh. This unfortunately caused a substantial reduction in first cycle discharge capacity. Further options were explored, with a premade graphite on copper foil electrode with a perforated hole being examined. This premade electrode showed a similar capability for gas transfer compared to copper mesh and also provided similar electrochemical performance, this paired with its documented use in literature meant that the premade electrode was chosen going forward in the project.

Chapter 3 Investigation Into the Effects of Dissolved Transition Metals on Gas Evolution Properties of Graphite Electrodes

3.1 Context

As discussed in the introduction, to accommodate the rapidly growing need for higher performing batteries, new high-capacity cathode materials need to be investigated and eventually incorporated into commercial cells. A particularly promising class of materials are nickel rich NMCs, which have a decreased cobalt content, but are prone to degradation.

The degradation processes of NMC cathodes have also been found to cause the structural transition metal ions to dissolve into the electrolyte [80, 85, 118]. The nickel, manganese, and cobalt transition ions can then travel to the graphite electrode and disrupt the SEI layer, thus producing exacerbated capacity fading [11, 119-123]. Specifically, manganese has been found to have the strongest effect on capacity fading [11], which has been ascribed to its catalytic activity to decompose graphite SEI components [83] as well as bulk electrolyte components [84], and the structural degradation of graphite due to manganese co-intercalation [124].

This work undertakes a systematic gas analysis investigation of the three transition metal ions (nickel, manganese, and cobalt) in graphite vs LFP cells designed with a capacity oversized LFP counter electrode. This was done so that both the electrochemistry and the gas evolution properties were solely dominated by the graphite electrode response. Although a previous gas analysis study compared the effect of nickel and manganese [83], this is the first study that also includes cobalt.

3.2 Gas Evolution Behaviour in Baseline LP57 Electrolyte

Before the effects of dissolved transition metals on gas evolution can be explored, it is first important to establish a point of comparison. Here, electrochemical and pressure measurement data from the LFP vs graphite cells with LP57 electrolyte will form the baseline for comparison in later discussions.

It is important to first note that during Chapter 3, Chapter 4, and Chapter 5, averaged data with error calculations that will presented, are calculated based on 3 repeats with errors calculated by determining the standard deviation between the 3 repeats. Data that uses a specific

cell as an example will use a cell that has shown to have reproducible results in comparison to the repeats and thus is an adequate representative of the group of cells.

The electrochemical cycling protocol for these cells consisted of a voltage hold at 1.5 V for 24 hours, followed by 1 cycle at C/20, and then 2 cycles at C/10, with the 3 cycles having voltage limits of -1.8 to -3.45 V.

To attribute gas evolution behaviours to specific electrochemical events, pressure measurement data will be examined alongside electrochemical cycling data. In Figure 33, the gas volume over time is shown, with the electrochemical cycling data alongside for cycling protocol reference.

Firstly, when examining the gas volume evolved during the voltage hold (initial 24h in Figure 33), the cell produces a very low volume of gas over the entirety of the voltage hold, with a change of approximately 0.51 ±0.31 $\mu l g^{-1}$ over the 24-hour period. It should be noted that at the very beginning of the voltage hold, a small increase in gas volume is observed; this is thought to be caused by the wetting of the separators and electrodes with electrolyte and therefore is not considered a gas evolution event. The negligible change in gas volume correlates well with expectations, as the cell is not expected to undergo any electrochemical reactions that would produce gasses at 1.5 V. Any pronounced increases or decreases in gas volume during this period would most likely be due to the presence of contaminants or leaks. Therefore, during the project, the voltage hold became an indicator for the viability of the cell, where only the cells with a relatively pressure values in the voltage hold were considered successful.

After the voltage hold, the cell undergoes cycling at a C-rate of C/20 (cycle 1 in Figure 34), where the gas volume initially increases drastically before plateauing into a slower rate of gas evolution. Over the course of cycle 1, 3.64 ±0.49 $\mu l g^{-1}$ of gas evolved over a time span of 38.5 hours, with half of the gas being evolved within the first 5 hours. This again corresponds well with expectations, as the SEI formation reaction on the graphite surface is expected to create this characteristic pressure measurement profile [72, 83]. At the start of the cycle, the pristine graphite surface reacts with the electrolyte components generating SEI compounds and gaseous products (such as those shown in Figure 6 in section 1.3.2), which leads to the observed drastic increase in gas volume. Over time, as these SEI compounds accumulate, a stable SEI layer is formed. This SEI layer would then prevent further reactions with the electrolyte as it is electronically insulative, which would then decrease the amount of gas evolved and therefore lead to the plateauing effect seen after the drastic increase.

In the subsequent C/20 cycles (cycle 2+3 in Figure 34), the pressure measurement profile continues the plateauing behaviour, with no significant changes from the trend observed in the later parts of cycle 1. During cycle 2+3, approximately 1.09±0.13 $\mu l g^{-1}$ of gas evolved over 36 hours, with the rate of gas evolution being the same in both cycle 2+3. This indicates that there is also no extensive change in the SEI properties once the plateauing behaviour occurs, which again is in line with expectations. It is important to note that whilst the plateau in gas volume indicates a formation of a stable (unchanging) SEI, the amount of gas produced in later stages of cycling is not negligible. This continuous evolution of gas after the formation of the SEI suggests that electrolyte components are still, to some extent, able access the graphite surface and/or undergo the gassing reaction despite the presence of the SEI layer. The continuation of these gassing reactions implies that the properties of the SEI layer, whilst able to supress the reactions, are inadequate to fully prevent them in later cycles.

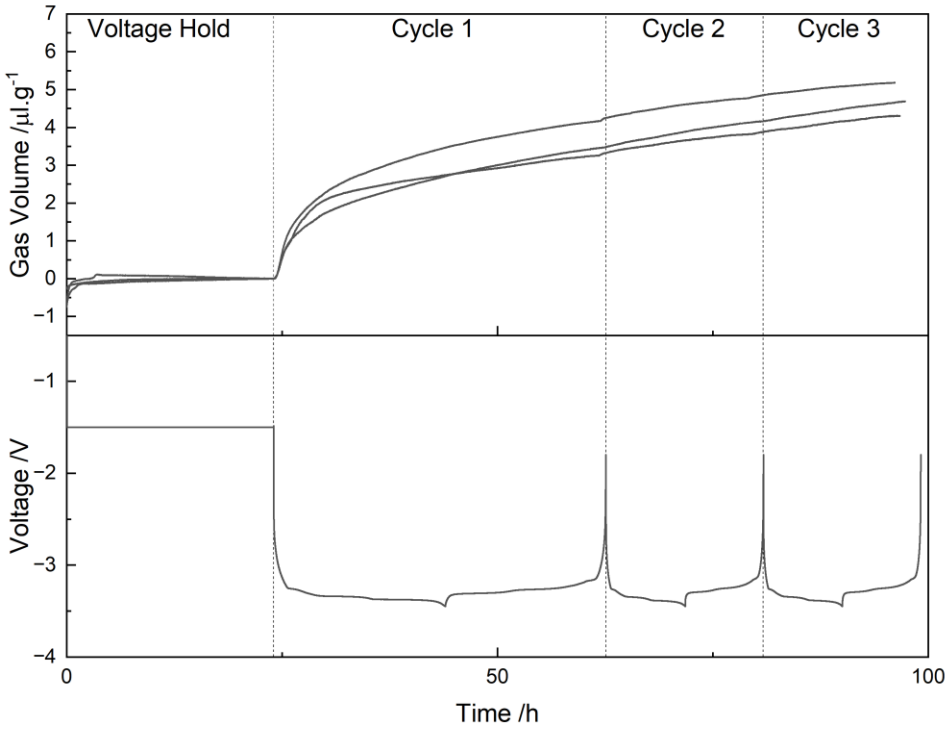

Figure 33 – Gas volumes produced overtime during cycling of LFP vs graphite Swagelok Pressure cells with the baseline LP57 electrolyte (3 cells). Voltage vs time graph for one of the cells (Cell 211) is given for cycling protocol reference.

Figure 34 shows the voltage vs capacity graph for an example baseline LP57 electrolyte cell, where we are able to see the expected profile trends. Additionally, it is possible to extract key information such as discharge capacity and coulombic efficiencies from each cycle, which can be averaged among the repeats to give an understanding of the electrochemical performance from the cells, as summarised in Table 4.

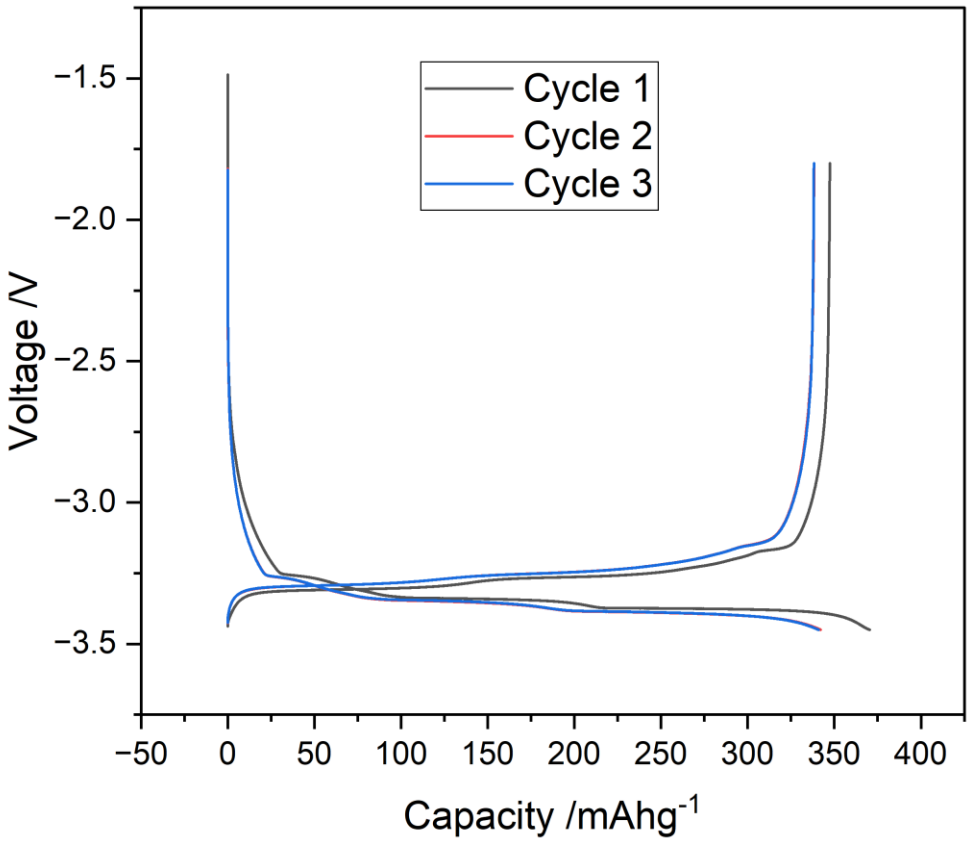

Figure 34 - Voltage vs capacity graph for a baseline LP57 electrolyte LFP vs graphite full cell (cell 211), showing the expected electrochemical behaviour of the cell, providing a comparative point for future work in this project.

	Discharge Capacity /mAhg^{-1}			Coulombic Efficiency /%		
Electrolyte	Cycle 1	Cycle 2	Cycle 3	Cycle 1	Cycle 2	Cycle 3
Baseline	347.0 ± 1.9	340.1 ± 2.9	340.3 ± 3.0	93.2 ± 0.5	99.0 ± 0.2	99.3 ± 0.1

Table 4 - Discharge capacity and Coulombic efficiency values per cycle for baseline electrolyte LFP vs graphite cells. Errors calculated from the standard deviation of 3 repeats.

In cycle 1 of Figure 34 , the example baseline LP57 the charge capacity of the cell is 370 mAhg^{-1}, which would be the maximum theoretical capacity of LFP as a material; it is unlikely for the cell to achieve this capacity solely on the lithium intercalation mechanism since the perfect utilisation of LFP is practically unachievable. Instead, this increased capacity (assuming the capacity obtained from lithium intercalation is lower than the theoretical maximum) is most likely due to the consumption of charge during the SEI formation reaction, originating from the reduction of electrolyte components. This correlates well with the gas evolution behaviours seen in Figure 33, where the onset of the SEI formation reaction is indicated by a sharp increase in gas

volume produced at this stage of the cycling. Additionally, the first cycle discharge capacity for the cell is 347 $mAhg^{-1}$, which is likely to be much closer to the capacity obtained solely from lithium intercalation as the SEI formation reaction does not occur during the discharge step of cycling [49]. From these values, it is possible to calculate the first cycle efficiency, in this case being 94%. First cycle efficiency values are expected to be approximately 95% assuming ordinary operation of the cell [125], therefore dramatic deviations would indicate additional factors impacting the electrochemistry.

Cycle 2+3 in the voltage capacity graph in Figure 34 exhibit very similar electrochemical behaviours, with both cycles achieving charge capacities of 341 $mAhg^{-1}$ and discharge capacities of 338 $mAhg^{-1}$, giving a first cycle efficiency of 99%. At this point in the cycling protocol, the SEI layer is expected to be fully formed, therefore the capacity values should only reflect the lithium intercalation reaction and an almost negligible amount of side reactions; this expectation matches well with the electrochemistry, as shown by the near 100% coulombic efficiency. This electrochemical data matches well with the gas evolution data, as no significant differences in behaviours were observed between cycle 2+3 and no abnormal changes in pressure were observed, reinforcing our expectations.

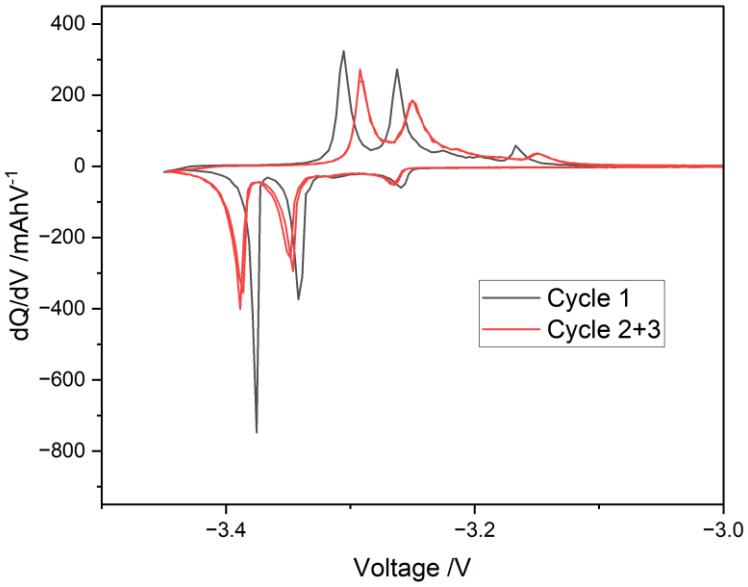

Figure 35 – dQ/dV vs voltage graph for baseline LP57 electrolyte LFP vs graphite full cell (Cell 211), showing the expected dQ/dV peaks for cycle 1 and cycle 2+3 (combined) associated with lithium intercalation/extraction, providing a comparative point for future work in this project.

The capacity and coulombic efficiency values obtained from Figure 34 match the averaged values shown in Table 4. For the remainder of this thesis, it can be assumed that the voltage vs

capacity graph of the example cell is a good representation of the behaviour seen across all 3 repeats.

Examination of the dQ/dV analysis as shown in Figure 35, shows the expected peaks that would arise from the intercalation/extraction of lithium ions into the graphite structure, where 3 clear peaks can be seen in the charge and discharging stages. A slight peak shift can also be observed between cycles 1 and cycles 2+3, where the peaks for cycles 2+3 have increased peak separation between the charging and discharging steps, indicating that greater potentials are required to drive the intercalation/extraction reactions, as expected from higher C-rates. Furthermore, greater peak heights were observed during cycle 1 when compared to cycle 2+3, which is again expected as higher capacities are obtained during lower C-rates that occur in cycle 1.

3.3 Gas Evolution Behaviour with the Introduction of Nickel Ions

Once the baseline electrochemical and pressure measurement data were obtained, the impact of the introduction of nickel ions was investigated. Nickel TFSI salt ($Ni(TFSI)_2$) was added to the baseline electrolyte, which was then used once again in the cycling of LFP/graphite cells.

From Figure 36, immediately, the impact of nickel dissolution can be seen in the gas evolution behaviour of the cell. The nickel cell at the beginning of cycle 1 behaves very similarly to the baseline cell, however with a slightly steeper increase in gas evolution before plateauing off. A total of 2.61 ±0.33 $\mu l g^{-1}$ of gas evolved over the entire cycle 1 which is comparatively less than the baseline cell (3.64 ±0.49 $\mu l g^{-1}$); however, half the gas of the Ni cell evolved in the first 2 hours (baseline: 5 hours), manifesting as a slightly steeper initial increase before the plateau. This indicates that the presence of Ni ions is promoting further reduction of the electrolyte components, suggesting that the presence of Ni ions is disrupting the SEI formation reaction. This is in line with expectations, as discussed in section 1.3.3, where the presence of transition metal ions is expected to reduce the LEDC to generate further gasses. Further discussion of this transition metal dissolution effect can be found later in this section.

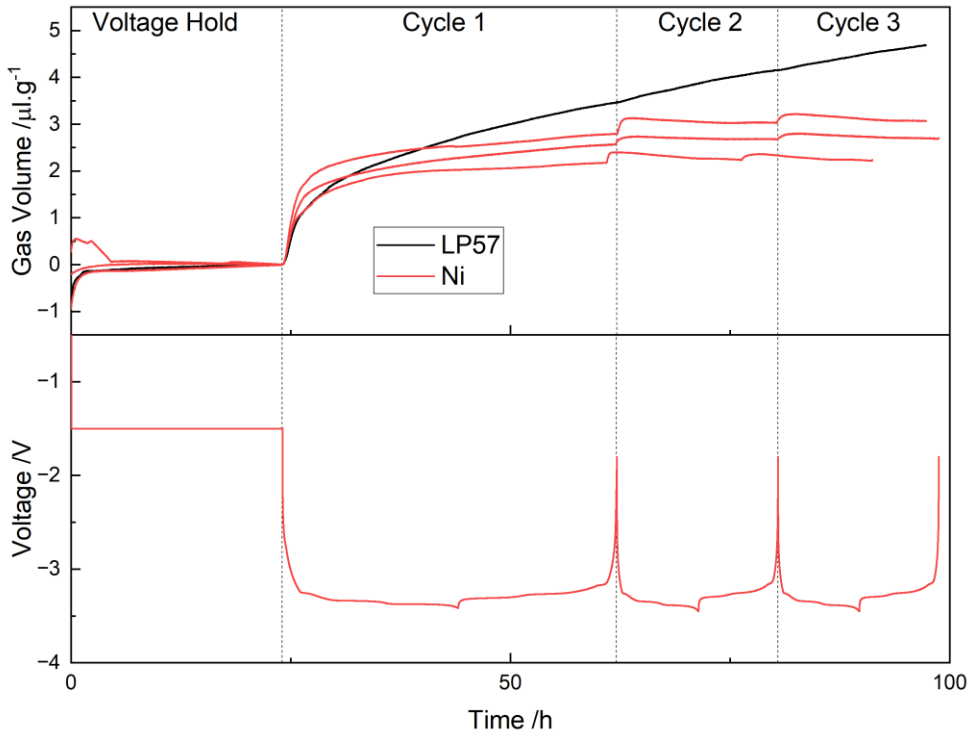

Figure 36 - Gas volumes generated in Ni doped electrolyte LFP vs graphite full cells (3 cells) with baseline LP57 cell 211 for comparison. Voltage vs time graph for Ni doped cell 282 below for cycling protocol reference.

In contrast to the steeper increase of gas evolution seen in cycle 1, at the plateauing stage, the rate of gas evolution of time is visibly different between the two cells, with 0.06 ±0.08 μlg^{-1} of gas evolved in cycle 2+3, which are both considerably lower than the 1.09 ±0.13 μlg^{-1} per cycle in the baseline cells cycle 2+3.The Ni cell shows a remarkably flatter plateau profile in comparison to the baseline cell, which is the opposite to expectations. The presence of nickel metal within the system is expected to destabilize the SEI layer formation, therefore increasing the number of gas evolution reactions, as shown by work done by Solchenbach et.al, where they demonstrated that the addition of Ni^{2+} ions lead to increased gas evolution [83]. However, in Figure 36, the flatter plateau suggests that the SEI layer formed under nickel electrolyte has improved properties over the baseline electrolyte and thus is more effective in preventing the decomposition of electrolyte components into gas. It is possible that the nickel ions present react with the electrolyte to form new compounds which are make the SEI layer more stable and/or resistant to further electrolyte decomposition.

Another distinct feature caused by the presence of nickel dissolution is the appearance of small pressure jumps, seen at the start of the charging steps of cycles 2+3 (Figure 37) shows a magnified section of this step). These small pressure jumps indicate in sudden increase in gas evolution and thus may signify that electrolyte is once again reacting at the graphite surface, resulting in the sudden jump in pressure. If this is the case, this would point to the Ni transition

metal ions interfering and possibly damaging the SEI layer, resulting in electrolyte molecules being able to access the graphite surface. The presence of Ni transition metal ions within the SEI structure having a detrimental effect would be in line with expectations.

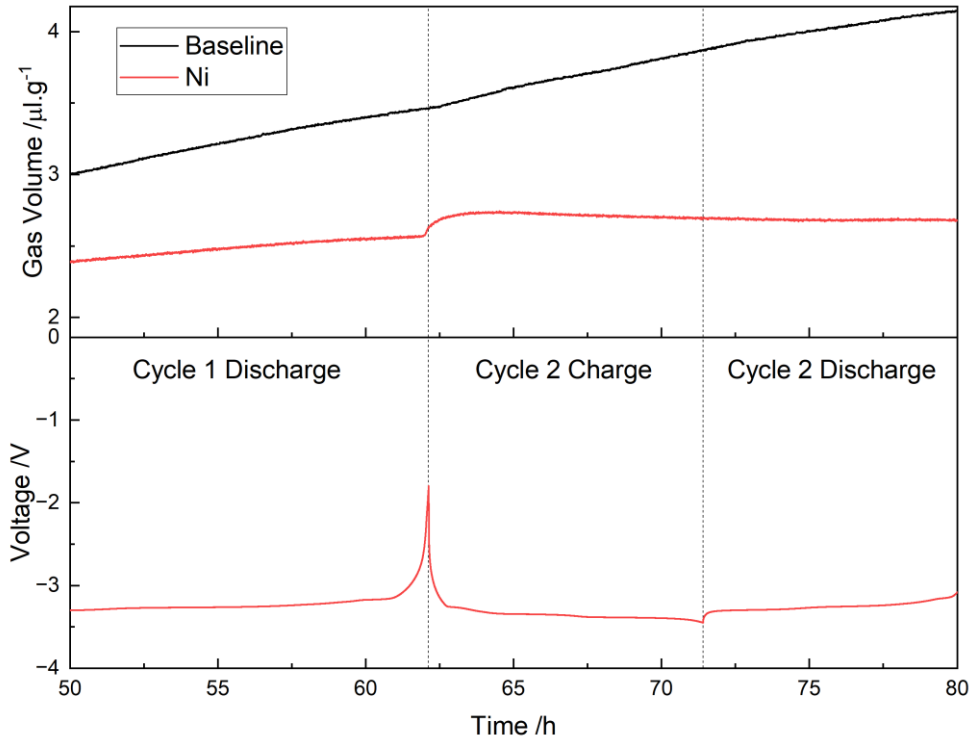

Figure 37 – Magnified view of Figure 37, focussing on a Ni doped cell 282, showing a small jump in gas volume produced at the beginning of cycle 2 charge step. Voltage vs time graph for Ni doped cell 282 below for cycling protocol reference.

From the gas evolution behaviour alone, it is not possible to determine whether the presence of Ni transition metal ions is advantageous for the cell. On one hand, the presence of Ni has decreased the overall amount of gas evolution occurring over the entire duration of cycling, however the presence of the small pressure jumps implies that the SEI is not particularly robust. To investigate this further, it is necessary to examine the opposing gas evolution factors alongside the electrochemical data, such as the discharge capacity (shown in Figure 38).

Figure 38 shows the voltage vs capacity graph of the LFP/Li half-cell with Ni electrolyte. From this graph, we see that Ni cells present the expected voltage vs capacity profile shape, however, exhibits a lower cycle 1 discharge capacity than expected. Clearly the presence of Ni in the SEI during cycle 1 affects the electrochemical performance of the cell.

From Table 5, the Ni cells show first cycle discharge capacities of 340.3 ± 1.6mAhg^{-1} and a first cycle efficiency of 91.4 ± 0.4%. Firstly, when compared to baseline cells, the Ni cells show a decrease in first cycle discharge capacity (difference of ~6.7 mAhg^{-1}) and a decrease in first cycle

coulombic efficiency (difference of ~1.8%). Firstly, the lower the first cycle discharge capacity highlights the detrimental effect of the presence of Ni transition metal ions, as less capacity from the lithium intercalation mechanism is available when compared to the baseline. Clearly, the intercalation reaction was impacted by the Ni ions and resulted in an increase in unwanted side reactions, as shown by the decreased first cycle efficiency. However, when comparing with the gas evolution data, the profile of the pressure change within the first cycle are very similar between the baseline cell and the Ni cell, with no significant increase in gas evolution being present which would have been expected if further SEI formation reactions had occurred. Therefore, it is more likely that the presence of Ni ions promotes an unwanted side reaction that does not produce any additional gas. Within literature, it has been shown that the presence of Ni dissolution can result in the disruption of the SEI layer, which can lead to less lithium intercalating/extracting to and from the graphite structure [121, 126, 127], this would explain the decrease in first cycle discharge capacity.

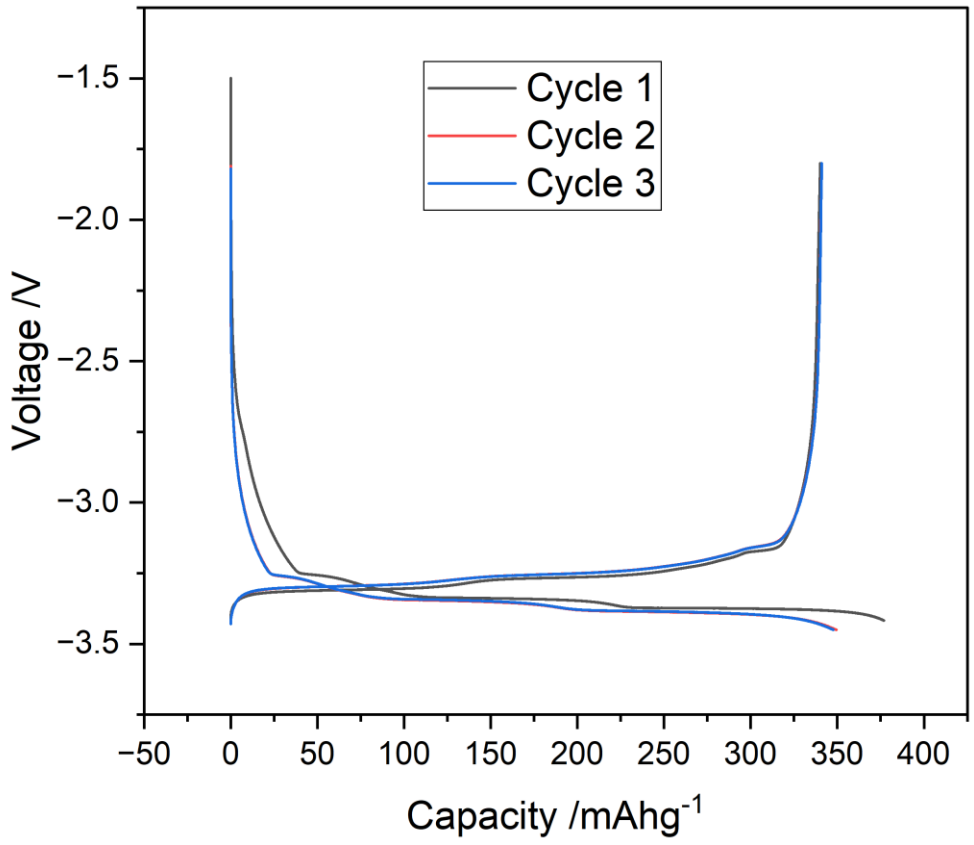

Figure 38 - Voltage vs capacity graph for a Ni doped electrolyte LFP vs graphite Swagelok cell (cell 282), showing decreased cycle 1 discharge capacity.

	Discharge Capacity /mAhg^{-1}			Coulombic Efficiency /%		
Electrolyte	Cycle 1	Cycle 2	Cycle 3	Cycle 1	Cycle 2	Cycle 3
Baseline	347.0 ± 1.9	340.1 ± 2.9	340.3 ± 3.0	93.2 ± 0.5	99.0 ± 0.2	99.3 ± 0.1
Ni	340.3 ± 1.6	333.2 ± 6.1	332.4 ± 6.6	91.4 ± 0.4	98.7 ± 0.2	99.0 ± 0.2

Table 5 - Discharge capacity and Coulombic efficiency values per cycle for Ni doped electrolyte LFP vs graphite cell, with the baseline LP57 values for comparison. Errors calculated from the standard deviation of 3 repeats.

In cycle 2 and 3 of Table 5, the Ni cell exhibits a discharge capacity of 333.2 ±6.1 mAhg^{-1}and 332.4 ±6.6 mAhg^{-1} respectively, and a coulombic efficiency of 98.7 ±0.2% and 99.0 ± 0.2% respectively. As mentioned previously, the SEI layer is expected to be fully formed by cycle 2+3; clearly the presence of Ni ions within the SEI layer is damaging the insulative properties and allowing the electrolyte to reach the graphite surface, as shown by the decreased discharge capacities and marginally decreased coulombic efficiencies. By following the SEI disruption pathway outlined in section 1.3.3, this could explain the electrochemical and gas evolution behaviours. Firstly, it is possible that Ni^{2+} is reduced to Ni^{0} by electron transfer from the graphite surface. This Ni^{0} then reacts with the surround LEDC or EC to generate gas, causing the observed pressure jumps in Figure 36. The fact that this occurs during the charging step of the cycles reinforces this hypothesis as this SEI decomposition pathway is expected to only occur during the charging step. As discussed earlier, literature has shown that the presence of Ni ions can reduce the amount of lithium that is intercalated/extracted from the graphite structure [121, 126, 127], not only would this decrease the first cycle capacity but it would also decrease the subsequent capacities in later cycles as the lithium remains trapped in the SEI layer.

The dQ/dV analysis shown in Figure 39 shows that in cycle 1 and cycle 2+3, the peaks representing the lithium intercalation/extraction are near identical between baseline LP57 and Ni cells. This similarity suggests that the presence of Ni does not have an adverse effect on the charging/discharging mechanism and any impact of Ni on the SEI conductivity properties are relatively small.

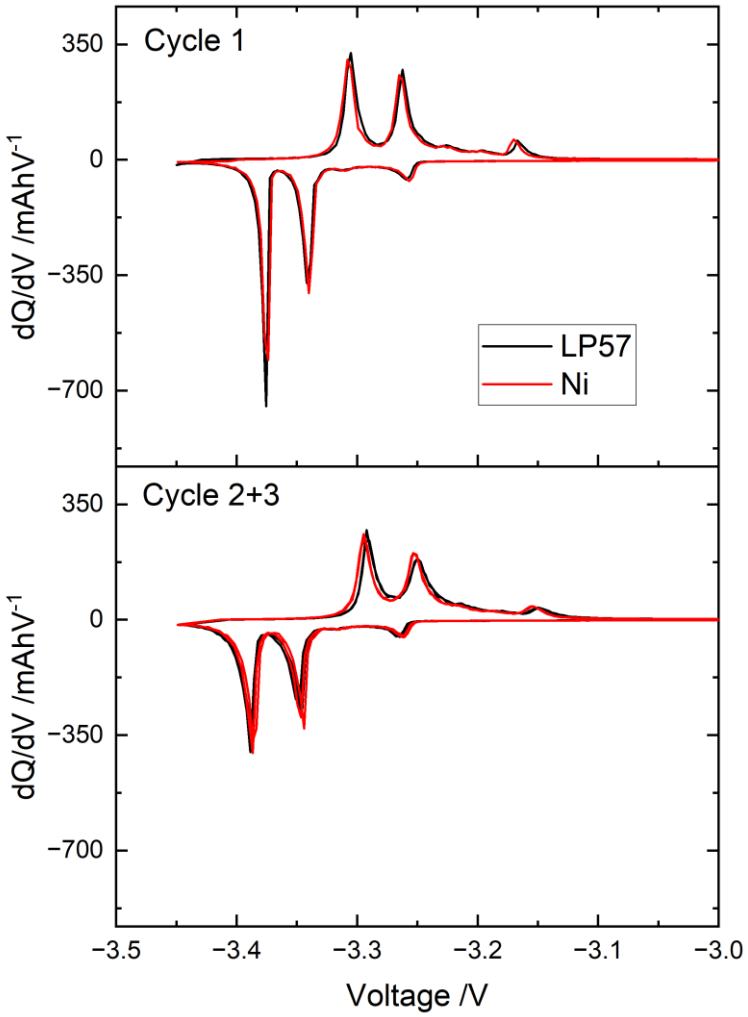

Figure 39 - dQ/dV vs voltage graph for Ni doped LP57 electrolyte LFP vs graphite full cell (Cell 82) compared with baseline LP57 cell 211.

3.4 Gas Evolution Behaviour with the Introduction of Manganese Ions

Gas evolution behaviour of cells with the introduction of manganese transition metal ions (manganese TFSI salt ($Mn(TFSI)_2$) to the baseline electrolyte was then investigated. Here in this section, the results from the manganese cells will only be compared to the baseline cell, with comparisons between transition metal cells being discussed in a later section (section 3.6).

When examining the gas evolution behaviour of Mn cells as seen in Figure 40, it is firstly clear that the quantity of gas evolved for the Mn cell during cycle 1 is considerably greater than that seen in the baseline cell. Not only is the total gas evolved over cycle 1 greater, 5.14 ±0.39 μlg^{-1} compared to baseline cell's 3.64 ±0.49 μlg^{-1}, the time elapsed to achieve half the total gas was also 2 hours compared to baseline cell's 5 hours, exemplifying the significantly greater increase in gas evolution during the SEI formation step. This gassing behaviour matches well with expectations, again linking with the transition metal dissolution impact on the SEI, where the

presence of manganese transition metal ions is expected to react with LEDC and EC molecules to create more gaseous products.

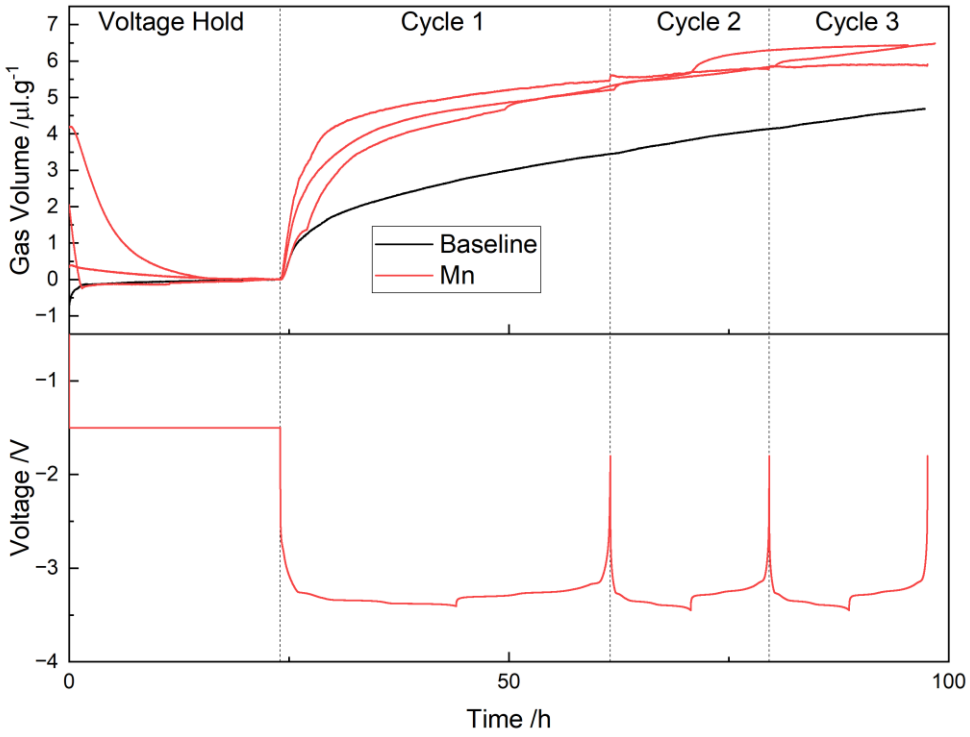

Figure 40 - Gas volumes generated in Mn doped electrolyte LFP vs graphite full cells (3 cells) with baseline LP57 cell 211 for comparison. Voltage vs time graph for Mn doped cell 276 below for cycling protocol reference.

In cycles 2+3, Mn cells generated 1.14 ±0.64 μlg^{-1} of gas. This compared to baseline cell's 1.09 ±0.13 μlg^{-1}, shows that the final SEI layer formed with or without the presence of Mn has similar ability to prevent further reduction of electrolyte components. This is unexpected as the presence of Mn is expected to cause the catalytic disruption of the SEI layer causing further gas evolution. The fact that this does not happen implies that eventually, the SEI layer is able to prevent the reduced Mn from further reaction. The presence of Mn is expected to promote further growth of the SEI layer, making it thicker and therefore less likely for electrolyte components to reach the graphite surface [128-130], therefore given enough time, the SEI layer should in theory be robust. However, the presence of the pressure jumps is also observed, corresponding well with the current understanding of the transition metal dissolution SEI disruption pathway, where the Mn^{2+} is being reduced back to Mn^{0} during the charge step which then subsequently reacts with LEDC and electrolyte molecules to generate gas.

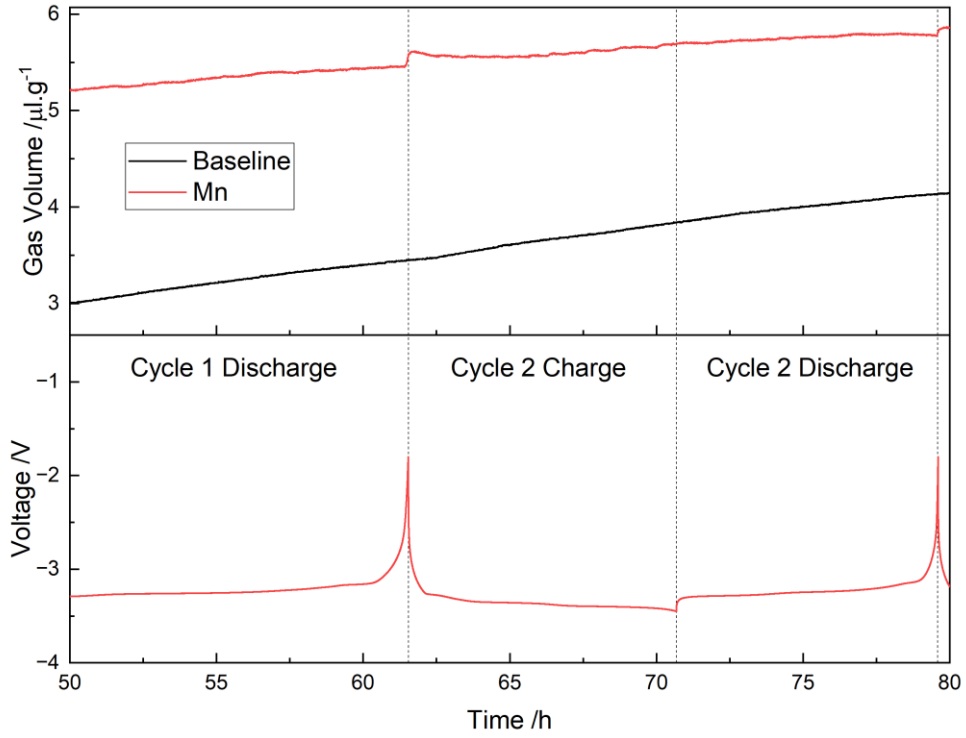

Figure 41 - Magnified view of Figure 40, focussing on a Mn doped cell 276, showing a small jump in gas volume produced at the beginning of cycle 2 charge step. Voltage vs time graph for Mn doped cell 276 below for cycling protocol reference.

Figure 42 shows the voltage vs capacity graph for a Mn cell, where the first cycle discharge capacity profile appears to give a lower capacity value than in cycle 2 and 3. This indicates that the presence of Mn is significantly disturbing the first cycle lithium intercalation/extraction mechanism, thus resulting in a deviation of voltage-capacity profile from the baseline.

From Table 6, where the first cycle discharge capacity for Mn cells is 329.4 ±6.5 $mAhg^{-1}$ and a first cycle coulombic efficiency of 87.8 ±0.4%. When comparing the discharge capacity, the Mn cell is drastically lower than the baseline cell (difference of ~17.6 $mAhg^{-1}$); as discussed earlier, the discharge capacity is thought to be a better indicator for the capacity associated solely on the lithium intercalation/extraction mechanism, where the disparity between the charge and discharge capacity can be associated with the SEI formation reaction or other unwanted side reactions. Since the discharge capacity has decreased, it is likely that the presence of Mn ions has disrupted the SEI formation and/or taken part in additional side reactions. The decrease in first cycle coulombic efficiency matches well with expectations, both electrochemically and from the gas evolution trends, where the presence of Mn ions is likely to promote further electrochemical reduction of electrolyte/LEDC compounds to produce increased volume of gas during the first cycle charge step.

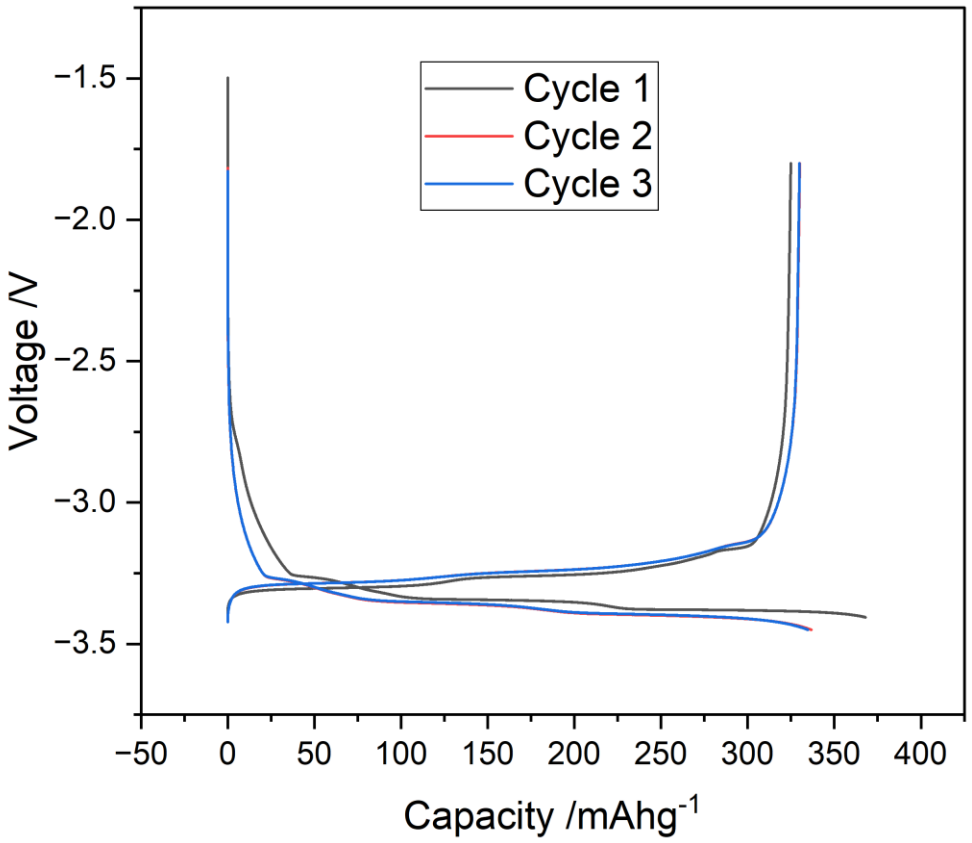

Figure 42 - Voltage vs capacity graph for a Mn doped electrolyte LFP vs graphite full cell (cell 276), showing a deviation from the standard profile. This is caused by the lower discharge capacity achieved in cycle 1.

	Discharge Capacity /mAhg^{-1}			Coulombic Efficiency /%		
Electrolyte	Cycle 1	Cycle 2	Cycle 3	Cycle 1	Cycle 2	Cycle 3
Baseline	347.0 ± 1.9	340.1 ± 2.9	340.3 ± 3.0	93.2 ± 0.5	99.0 ± 0.2	99.3 ± 0.1
Mn	329.4 ± 6.5	331.0 ± 5.1	330.9 ± 5.1	87.8 ± 0.4	97.6 ± 0.5	98.4 ± 0.1

Table 6 - Discharge capacity and Coulombic efficiency values per cycle for Mn doped electrolyte LFP vs graphite cell, with the baseline LP57 values for comparison. Errors calculated from the standard deviation of 3 repeats.

Table 6 also shows that the Mn cell continues to perform worse than the baseline cells in both cycle 2+3. The Mn cell achieves discharge capacities of 331.0 ±5.1% and 330.9 ±5.1% for cycle 2 and 3 respectively. Both values are lower than that seen in the baseline cells (difference of ~10 mAhg^{-1} for both cycles), indicating that the lithium intercalation/extraction mechanism is being disrupted by the presence of Mn ions. A possible explanation for this could be that the SEI layer that has been formed is now too thick for optimal transfer of lithium ions through the SEI

layer and into the graphite structure, therefore limiting the amount of lithium that is able to be extracted later. This also aligns well with the observed gas behaviour, where the increased gas evolution indicates further degradation of the electrolyte components into SEI layer products; more products would mean greater accumulation at the graphite surface, resulting in a thicker SEI layer. Work done by Shin et.al showed that dissolved Mn ions promoted further decomposition of electrolyte which then resulted in a thicker SEI layer and reduction in cell capacity [129]. This is further supported by the lower cycle 2 and 3 coulombic efficiencies, 97.6 ±0.5% and 98.4 ±0.1% respectively, which indicate an increase of side reactions occurring.

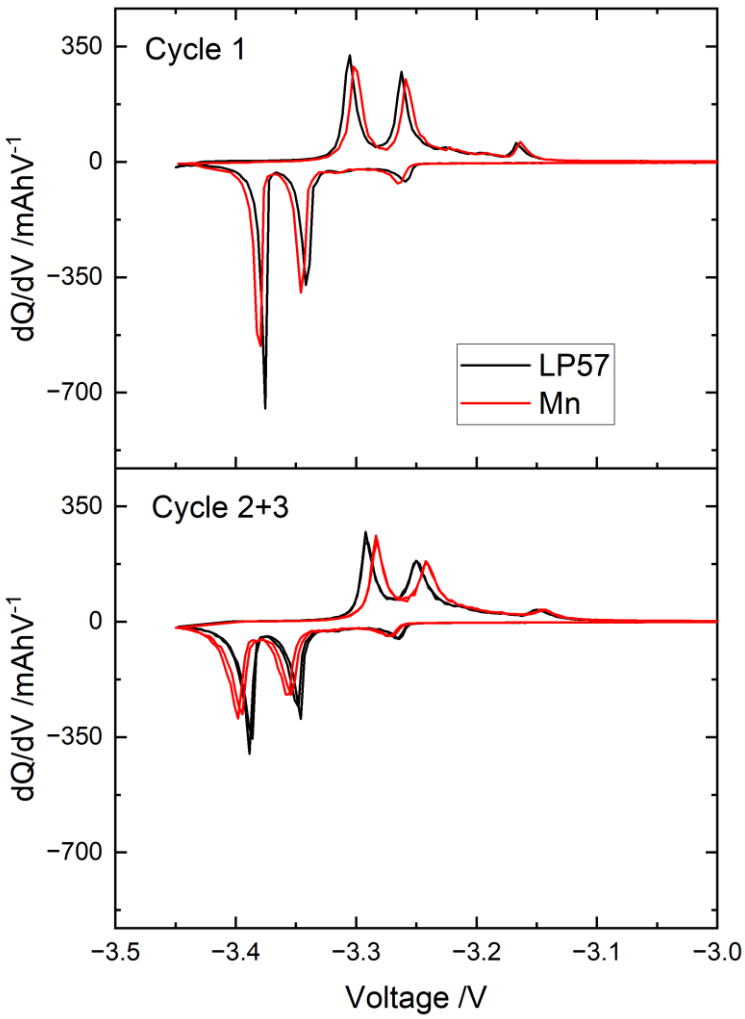

Figure 43 - dQ/dV vs voltage graph for Mn doped LP57 electrolyte LFP vs graphite full cell (Cell 276) compared with baseline LP57 cell 211.

The dQ/dV analysis shown in Figure 43 further corroborates the trends seen in the gas evolution behaviour and the capacity/coulombic efficiency analysis, where peak shifts in both cycle 1 and cycle 2+3 are observed in Mn cells in comparison to the baseline. From this, it is reasonable to assume that the presence of Mn in the SEI layer is decreasing the ionic/electronic conductivity of the SEI layer, thus explaining the increased peak shifts. This would match our predictions of the SEI layer growing thicker and therefore increasing the SEI resistance and

slowing the movement of Li ions to the graphite surface. Increased resistance of the SEI would then lead to lower charge/discharge capacities.

3.5 Gas Evolution Behaviour with the Introduction of Cobalt Ions

Examination of gas evolution behaviour in Cobalt cells, as shown in Figure 44, shows a new gas evolution trend, where the overall gas evolved over the entirety of the cycling protocol is lower however the sharp increase in pressure in cycle 1 is also lower than that of the baseline cell. From Figure 44, it is shown that Co cells produce a 2.20 ±0.29 μlg^{-1} during cycle 1, with half of the gas evolved within the first 3 hours. Compared with the baseline cell (3.64 ±0.49 μlg^{-1}), Co cells produce relatively lower amounts of gas, indicating that less electrolyte components are being reduced to gaseous products.

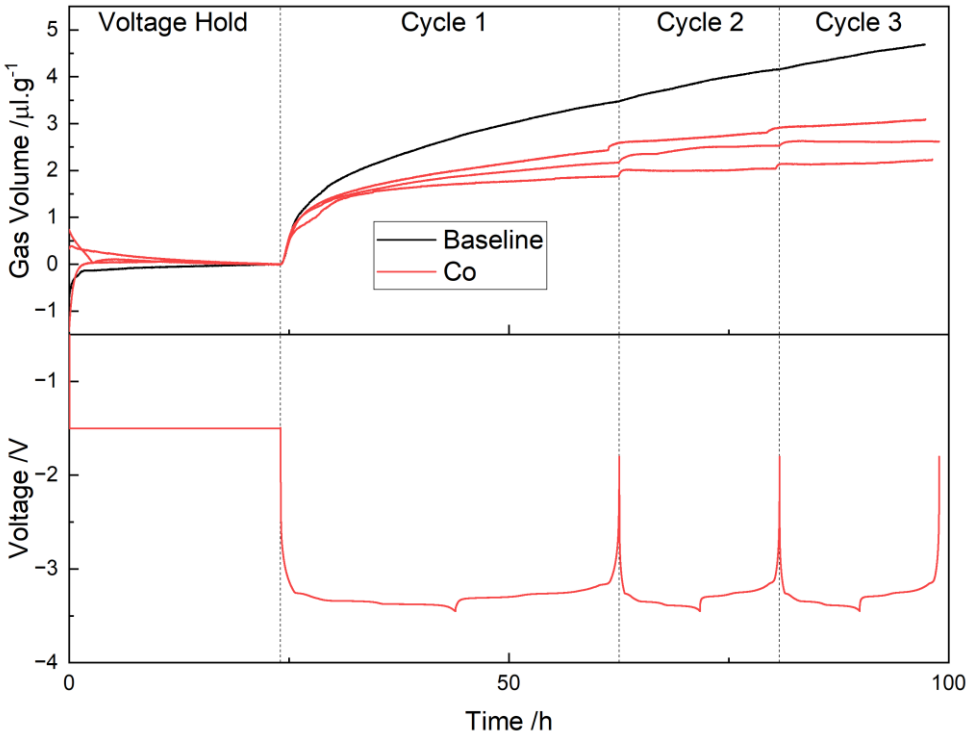

Figure 44 - Gas volumes generated in Co doped electrolyte LFP vs graphite full cells (3 cells) with baseline LP57 cell 211 for comparison. Voltage vs time graph for Co doped cell 249 below for cycling protocol reference.

This is the opposite of expectations as cobalt was expected to partake in the SEI disruption mechanism. Clearly from the gas evolution data, the presence of Co ions is instead beneficial as less electrolyte is consumed. The explanation for this behaviour is unclear; if the Co ions simply do not undergo the SEI disruption pathway, then the Co cell gas evolution data should in theory mimic that of the baseline cells. However, the gas evolution is reduced, therefore the Co ions must have a positive interaction with the SEI layer which leads to an improvement in its

properties, in particular its passivating abilities as less gas evolved means less electrolyte components being reduced. A possible explanation for this is that the Co ions are still undergoing reactions with either the electrolyte or SEI components, however these reactions may not be giving gaseous products. If this is the case, these new products could then accumulate once again in the SEI layer, which may possibly improve its properties without generating additional gas.

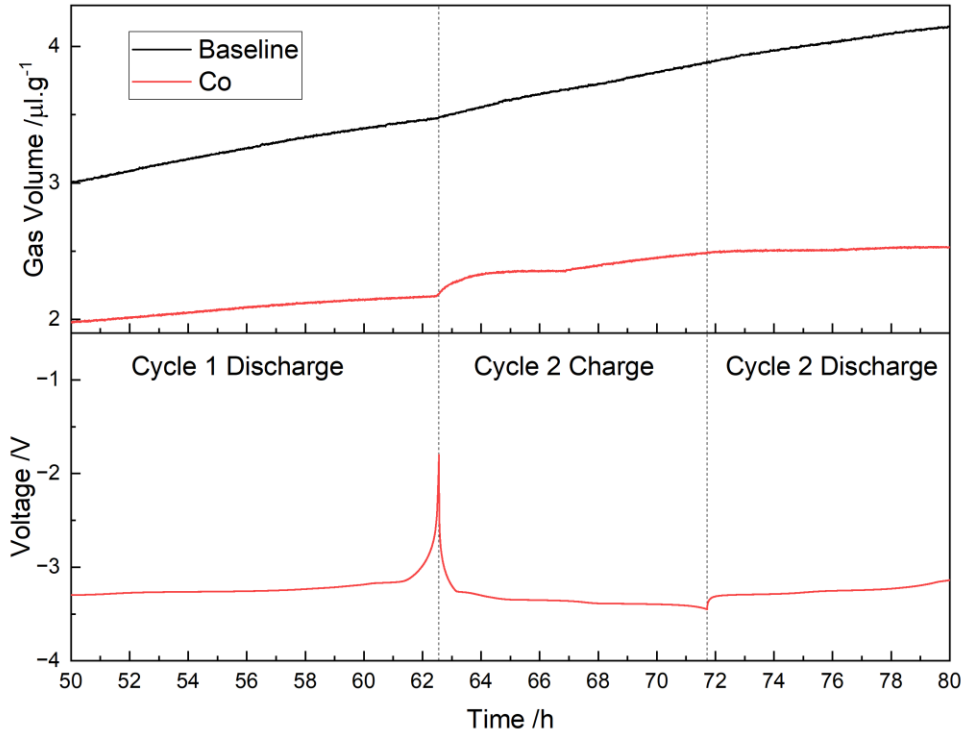

Figure 45 - Magnified view of Figure 37, focussing on a Co doped cell 249, showing a small jump in gas volume produced at the beginning of cycle 2 charge step. Voltage vs time graph for Co doped cell 249 below for cycling protocol reference.

When examining cycle 2+3 in Figure 44, the volume of gas produced is less than the baseline cell, with the Co cell producing 0.45 ±0.14 μlg^{-1} in cycle 2+3, compared to 1.09 ±0.13 μlg^{-1} for the baseline cell. This decrease in gas evolution can again be attributed to the improved SEI layer that is formed in the presence of Co ions. Interestingly, small pressure jumps are observed in Figure 45, once again at the start of the charging steps in cycle 2+3, indicating that the Co ions, to some extent, do still generate gasses in later cycles. This contradicts our earlier thoughts that Co does not partake in the SEI disruption pathway, instead it may be possible that it is simply to a much lesser extent than expected, such that it does not generate enough gas to surpass the baseline cells initial sharp pressure increase in cycle 1.

Figure 46, shows the voltage vs capacity graph for Co cells. Where the profile of the data seems to match the baseline LP57 very well. This is unexpected as the presence of transition

metal ions is thought to cause side reactions within the cell causing the cycle 1 discharge profile to be shifted to give lower capacity values.

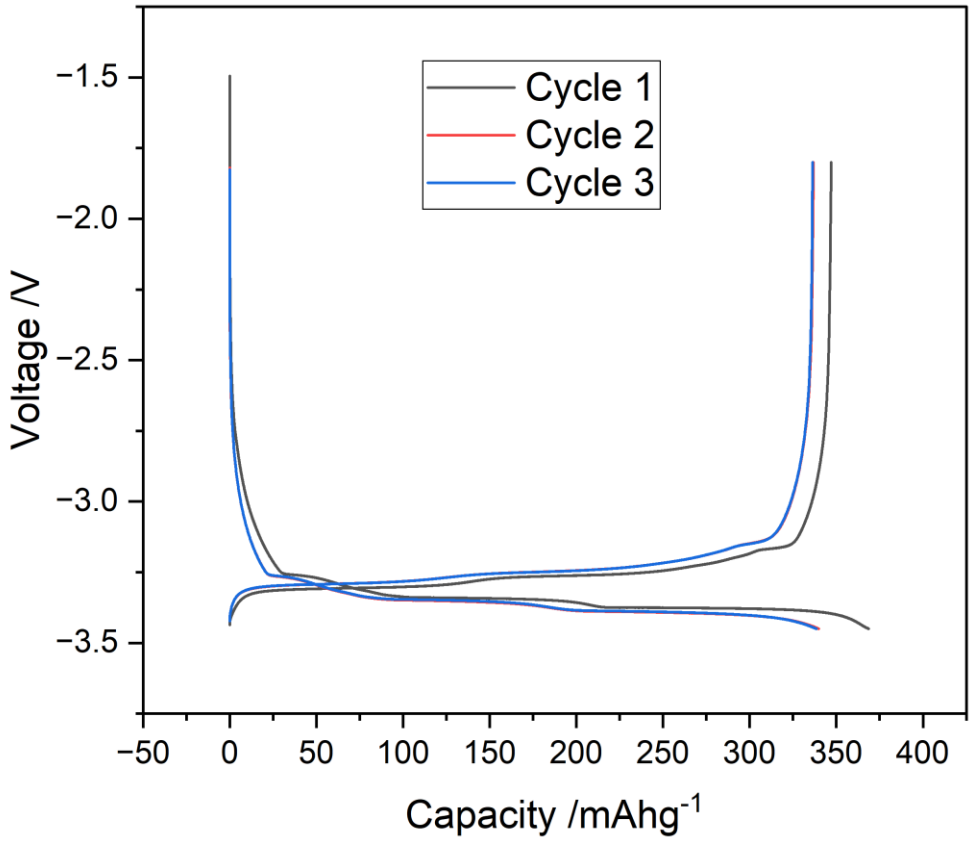

Figure 46 - Voltage vs capacity graph for a Co doped electrolyte LFP vs graphite full cell (cell 249).

	Discharge Capacity /mAhg^{-1}			Coulombic Efficiency /%		
Electrolyte	Cycle 1	Cycle 2	Cycle 3	Cycle 1	Cycle 2	Cycle 3
Baseline	347.0 ± 1.9	340.1 ± 2.9	340.3 ± 3.0	93.2 ± 0.5	99.0 ± 0.2	99.3 ± 0.1
Co	343.8 ± 3.7	334.2 ± 4.3	334.3 ± 4.6	92.8 ± 0.2	98.9 ± 0.1	99.3 ± 0.1

Table 7 - Discharge capacity and Coulombic efficiency values per cycle for Co doped electrolyte LFP vs graphite cell, with the baseline LP57 values for comparison. Errors calculated from the standard deviation of 3 repeats.

In cycle 1 of Table 7, the cell achieves a discharge capacity of 343.8 ±3.7 mAhg^{-1}, giving a first cycle efficiency of 92.8 ±0.2%. These electrochemical values match well with the expectations from the gas evolution data. Given that a visible difference between the gas evolution behaviour or the Co and baseline cells, a corresponding difference in electrochemical performance was

anticipated. This is seen in the decreased cycle 1 discharge capacity and coulombic efficiency of the Co cells, indicating that the Co is increasing the degree of side reactions occurring.

As the overall gas evolution behaviour has decreased during cycle 1, it is expected that the first cycle efficiency is to improve, as less capacity is dedicated for the decomposition of electrolyte and therefore the first cycle charge capacity would be lower. Our previous hypothesis could provide an explanation for this electrochemical behaviour; the capacities determined from Figure 46 is derived from the amount of charge passed during the cycling protocol, however it is not possible to discern what specific reactions are responsible for any exact amount of capacity. For example, it may be possible that the proportion of the charge capacity relating to the gas evolution reactions has indeed decreased, however with the presence of Co allows new electrochemical reactions that pass charge but does not generate gas, thus increasing the charge capacity whilst exhibiting lower gas evolution.

In cycle 2+3 of Table 7, Co cells obtain discharge capacities of 334.2 ±4.3% and 334.3 ± 4.6% for cycles 2 and 3 respectively, giving coulombic efficiencies of 98.9 ±0.1% and 99.3 ±0.1%. The discharge capacities show a small decrease when compared to the baseline cells (difference of ~6 $mAhg^{-1}$) however the coulombic efficiencies remain very similar. Once again, the hypothesis explained above, with Co allowing new electrochemical reactions, could explain the unexpected cycle 2+3 electrochemical behaviour. This would also explain the gas evolution behaviour observed for the Co cell during cycle 2+3 (decreased total gas evolved and small pressure jumps at the start of charging steps).

The dQ/dV analysis for Co cells can be seen in Figure 47, where the position of the three expected peaks are near identical between Co cells and baseline cells, indicating that the presence of Co within the SEI does not have a significant impact on the lithium intercalation/extraction mechanism.

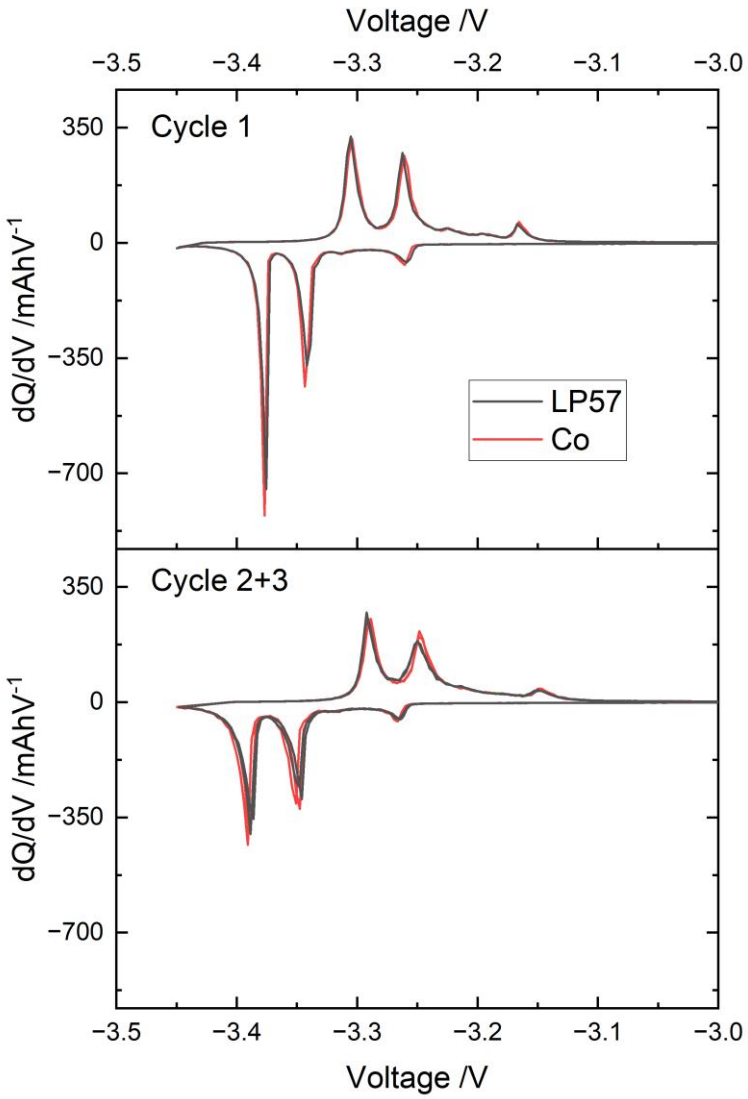

Figure 47 - dQ/dV vs voltage graph for Co doped LP57 electrolyte LFP vs graphite full cell (Cell 249) compared with baseline LP57 cell 211,.

3.6 Comparison of Gas Evolution Behaviour Transition Metals Dissolution

Here in this section, we will compare the gas evolution behaviour and electrochemical performance of cells containing electrolyte with transition metal ions present. Figure 48 compares the gas evolution behaviour between the transition metal doped cells with baseline cells, with the addition of the baseline cell voltage vs time graph to give reference to the cycling protocol.

Firstly, when comparing the gas evolution behaviour in cycle 1, Mn cells produce the most overall gas (5.14 ±0.39 μlg^{-1}), with baseline cells being second (3.64 ±0.49 μlg^{-1}), Ni cells third (2.61 ±0.33 μlg^{-1}) and Co cells very close behind at fourth (2.20 ±0.29 μlg^{-1}). This is also shown in quantitatively in Figure 49. It is known from literature that Mn ion dissolution has a severe

detrimental effect due to a SEI disruption pathway [81, 82, 124, 129] , therefore Mn cells producing the most gas is not surprising.

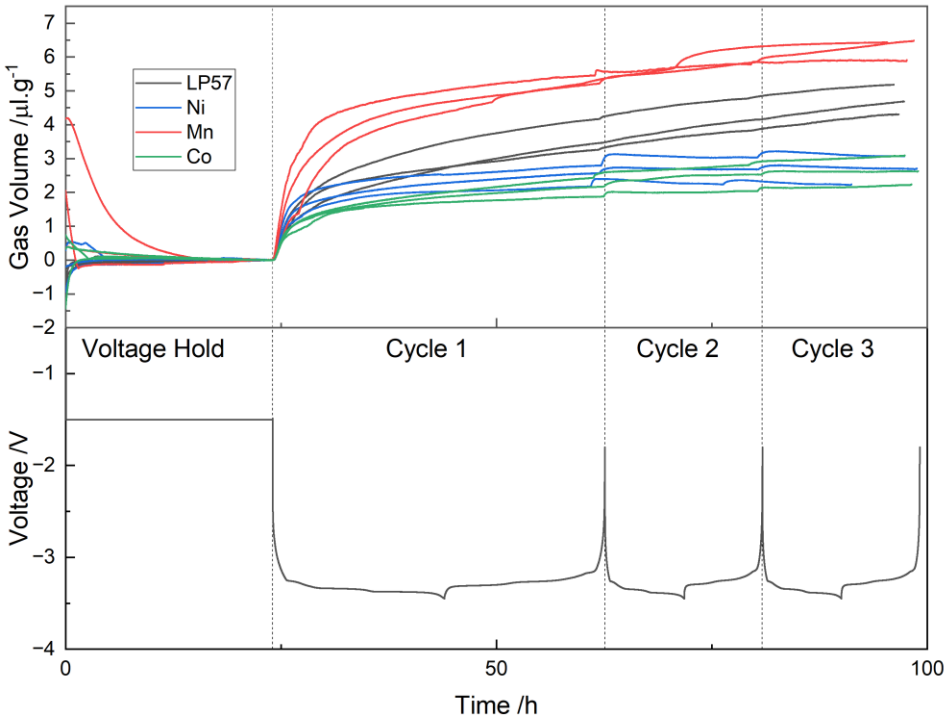

Figure 48 – Comparison of gas volumes generated in transition metal doped electrolyte LFP vs graphite full cells with baseline LP57 cells. Voltage vs time graph for baseline LP57 cell 211 below for cycling protocol reference.

However, the pathway in theory should also occur for Ni and Co ions, resulting in increased gas evolution within the first cycle (compared to the baseline), however this is not the case. Clearly, Mn possesses properties that allow it to be much more potent with regards to gas evolution reactions in comparison to Ni and Co, or Ni and Co are able to suppress the gas evolution reactions that occur. Komaba et al. investigated the influence of the same transition metal ions in graphite vs lithium cell with $LiClO_4$ electrolyte solution containing transition metal additives, where they found that Mn had the most significant impact on the electrochemical performance, followed by cobalt and Ni, and attributed this to the differences in redox potentials between Mn/Mn^{2+} (1.87 V vs. Li/Li^+), Co/Co^{2+} (2.77 V vs. Li/Li^+), and Ni/Ni^{2+} couples (2.80 V vs. Li/Li^+), causing different degrees of electrolyte decomposition [131]. This trend seen in their work is in line with what we observe in this chapter where Mn ions generate the most gas followed by Ni and Co generating similar amounts.

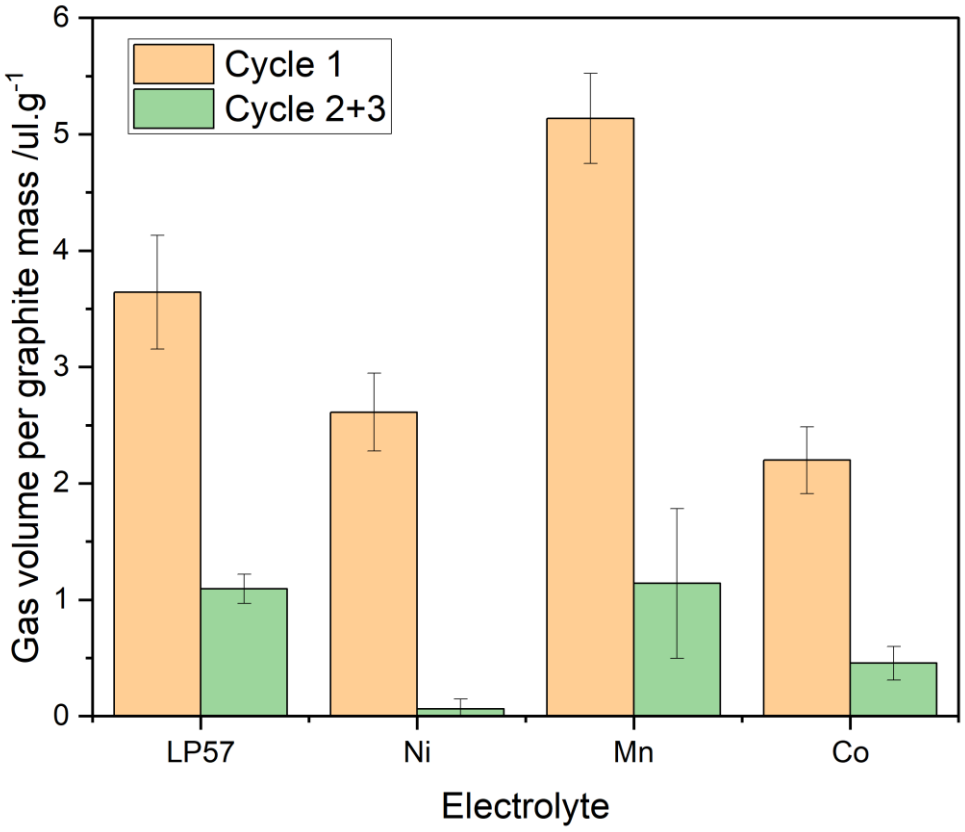

Figure 49 – Comparison of average total gas volumes during each cycle between transition metal doped electrolyte LFP vs graphite full cells with baseline LP57 cells. Errors calculated from standard deviation in 3 repeats per electrolyte.

Gas evolution behaviour in cycles 2+3 show interesting trends, where Mn generated the greatest gas volumes, which were comparable to the baseline cells, with Mn cells producing 1.14 ±0.64 μlg^{-1} and baseline cells producing 1.09 ±0.13 μlg^{-1} of gas. This similarity implies that the SEI formed with Mn ion dissolution has similar capabilities of preventing electrolyte decomposition to the baseline cell and thus similar amounts of gas produced. Ni and Co cells both reduced the amount of gas produced in cycle 2+3, Ni producing 0.06 ±0.08 μlg^{-1} and Co producing 0.45 ±0.14 μlg^{-1}. Ni and Co both reducing the amount of gas produced in comparison to Mn is expected especially when we consider the redox potentials of the transition metal couples, where Mn^{2+} is more readily reduced. However, it is unexpected that the Ni to have such a significant reduction in gas evolution in comparison to Co. It is currently unclear what the exact cause of this is, however, a possible explanation may be due to gas consumption reactions that may be caused by the presence of Ni and to some extent Co.

Figure 50 compares the first cycle discharge capacity and Figure 51 compares the first cycle coulombic efficiencies between the transition metal doped cells. These two graphs provide a good overview on the relative impact of transition metal dissolution on the electrochemical performance of the cell, specifically with respect to the SEI formation reaction during cycle 1.

Importantly, Figure 50 shows the discharge capacity within each cell category, with the baseline electrolyte (LP57 in the figure) having the highest capacity in all three cycles in comparison to the transition metal ion cells (baseline achieving 347.0 ±1.9 $mAhg^{-1}$). Addressing cycle 1, Mn has the lowest first cycle discharge capacity (329.4 ±6.5 $mAhg^{-1}$), with an interesting trend of the capacity value being below that of its own subsequent cycle 2+3 capacities (331.0 ±5.1 $mAhg^{-1}$ in cycle 2 and 330.9 ±5.1 $mAhg^{-1}$ in cycle 3). This behaviour is not observed for the Ni and Co cells. Ni cells achieved 340.2 ±1.6 $mAhg^{1-}$ in cycle 1, 333.2 ±6.1 $mAhg^{-1}$ in cycle 2, and 332.4 ±6.6 $mAhg^{-1}$). Co cells achieved 343.8 ±3.7 $mAhg^{-1}$ in cycle 1, 334.2 ±4.3 $mAhg^{-1}$ in cycle 2, and 334.3 ±4.6 $mAhg^{-1}$ in cycle 3. The Ni and Co cells instead follow the expected trend of cycle 1 having the greatest discharge capacity, which is expected as cycle 1 is operating at a lower C-rate. This low first cycle discharge capacity for Mn cells correlates well with what is observed in the gas evolution data, where the increased gas evolution during cycle 1 signifies a significant disruption to the SEI formation reaction, leading to a disruption to the lithium intercalation reaction and therefore resulting in less lithium available to be extracted in the discharge step. Ni and Co cells are relatively similar in their cycle 1 discharge capacities, with both cells achieving >340 $mAhg^{-1}$. Co cells have marginally improved discharge capacity over Ni cells (343.8 ±3.7 $mAhg^{-1}$ and 340.3 ±1.6 $mAhg^{-1}$ respectively) which corroborates well with the gas evolution data, where similar trends are observed i.e. Ni cells produces marginally more gas in cycle 1 than Co cells. Examining the coulombic efficiencies in cycle 1 as shown in Figure 51, we see that all the transition metal cells show similar values, with a difference of approximately 1-3% between the cells. Mn having a marginally lower efficiency of 87.8 ±0.4% matches well with expectations as the increased gas evolution suggests a greater degree of side reactions occurred.

Electrochemical behaviour in cycles 2+3 become a lot more homogenised, with all three transition metal cells having relatively similar discharge capacity values (all cells achieved >330 $mAhg^{-1}$), very similar coulombic efficiencies (all cells achieved >97%). In all three transition metal cells (Ni, Mn, Co), it seems that the SEI layer formed was efficient enough to prevent further reactions with the electrolyte, as evidenced by the very high coulombic efficiencies. The discharge capacities, however, reveal that despite the SEI layer allowing a high coulombic efficiency to be achieved, the lithium intercalation reaction for all three transition metal cells were sub-optimal compared to the baseline. The SEI disruption pathway involving transition metal ions is thought to lead to side reactions that result in loss of capacity [83], thus it is possible that the pathway is the cause of the lower discharge capacities. It was expected that the electrochemical behaviour of Mn cells would still be markedly underperforming in cycles 2+3, however this is not the case, indicating the impact of transition metal dissolution is most crucial during cycle 1, prior to the SEI formation reaction. These electrochemical behaviours are also reflected in the gas evolution data,

where the greatest differences in gas evolution occur within cycle 1, with differences in cycles 2+3 being less prominent.

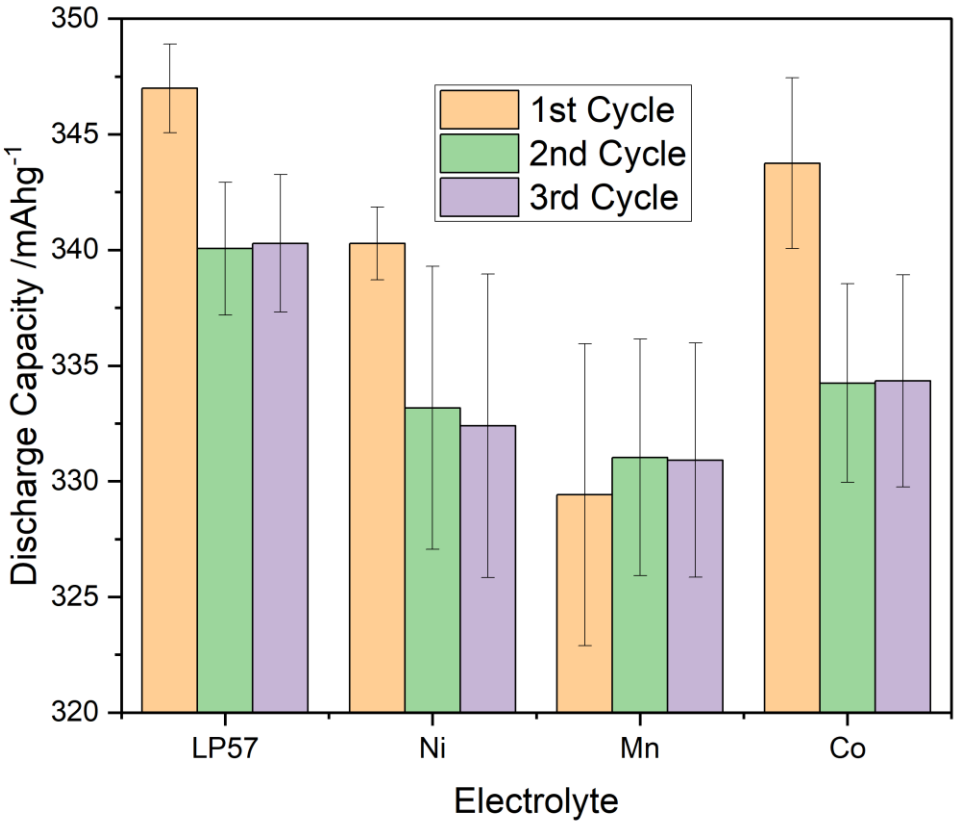

Figure 50 - Comparison of average discharge capacity per cycle between transition metal doped electrolyte LFP vs graphite full cells with baseline LP57 cells. Errors calculated from standard deviation in 3 repeats per electrolyte.

When comparing these electrochemical and gas evolution results to literature, there is a clear correlation where Mn^2 is often shown to be significantly more impactful than Ni and Co. For example, Solchenbach et.al demonstrated that the gas evolution from Mn dissolution was significantly higher than from Ni dissolution, where they postulate that the diffusion of Ni^{2+} to the graphite surface is slower or the electron transfer within the SEI occurs less readily [83]. Furthermore, Wandt et.al. used operando XAS to find that the found that Mn^{2+} ions were readily reduced to Mn^0 whilst it was possible for Ni and Co to remain in the 2+ state [85], which is also in line with the theory that differences in redox potentials between Mn/Mn^{2+}, Co/Co^{2+} and Ni/Ni^{2+} couples causes different degrees of electrolyte decomposition [131]. Clearly, Mn ions is more susceptible to reduction which may result in increased gas evolution reactions and subsequently a decrease in electrochemical performance.

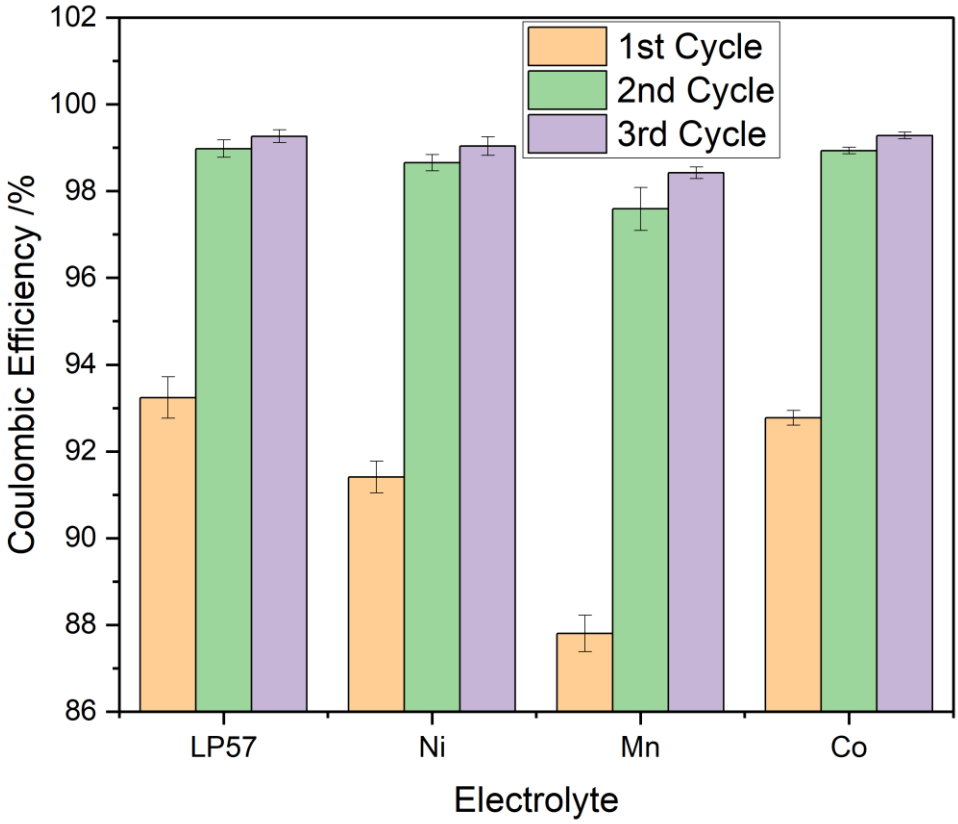

Figure 51 - Comparison of average coulombic efficiency per cycle between transition metal doped electrolyte LFP vs graphite full cells with baseline LP57 cells. Errors calculated from standard deviation in 3 repeats per electrolyte.

3.7 Summary

Here, in this chapter, transition metal ions (Ni, Mn, Co) were artificially added to the baseline LP57 electrolyte of LFP vs graphite full Swagelok pressure cells. The subsequent impact of the transition metal ion dissolution was investigated by examining the gas evolution and electrochemical behaviour during the cycling of the cells.

From these investigations, it was determined that all 3 transition metal ions had a notable impact on both the gas evolution during the SEI formation reaction and later stages of cycling. Furthermore, the electrochemical performance of the cell was also affected by the dissolution of transition metal ions.

However, the nature of the impact differs, especially with Mn, where the detrimental effect is considerably more drastic in comparison to Ni and Co. The presence of Mn both significantly increased the amount of gas produced during cycle 1, but also causes substantial loss in first cycle discharge capacity. Clearly, Mn ions being present within the electrolyte, disrupts the SEI formation reaction, such that further electrolyte components can be reduced at the graphite

surface, causing the increased gas evolution and loss of first cycle discharge capacity. This in line with what has been observed in literature.

The impact of Ni and Co dissolution seems to be quite similar to one another, with both transition metal ions having similar gas evolution behaviour to the baseline during the initial stages of cycling, but then having less gas evolved in later stages of cycling compared to the baseline. This suggests that the SEI formed in the presence of Ni and Co seemingly has advantageous properties, as it can prevent further reduction of electrolyte components after the SEI has been formed. The given hypothesis is that the presence of Ni and CO facilitates an additional non-gas evolving electrochemical reaction, yielding a product that accumulates into the SEI layer, improving its passivating properties. The electrochemical data further solidifies this theory as we do observe a marginal decrease in first cycle discharge capacity and first cycle efficiency, indicating that there are further side reactions occurring during the initial stages of cycling.

It is theorised that the Mn dissolution has a drastically increased impact on the cell performance due to its ability to readily undergo further side reactions, causing irreversible capacity loss and further gas evolution. Finding ways to limit these side reactions with Mn is crucial to improving cell systems where Mn dissolution can occur.

In summary, the work done in this chapter has given a good overview on the impact of transition metal dissolution, and its effect on gas evolution and electrochemical performance. The results here will be used in the following chapters as a comparative point.

Chapter 4 Investigation Into the Effects of Electrolyte Additives on Gas Evolution Properties of Graphite Electrodes

4.1 Context

The impact of different electrolyte additives can often vary, as many of them operate via different reaction pathways due to their different chemistries. Elucidating the nature of these reaction pathways and their relative impact on the cell is very important for future work such as formulating new electrolytes to assist with new issues.

Within this section, the effects of different electrolyte additives on the gas evolution behaviour of LFP vs graphite cells will be investigated.

4.2 Gas Evolution Behaviour with the Introduction of VC Additive

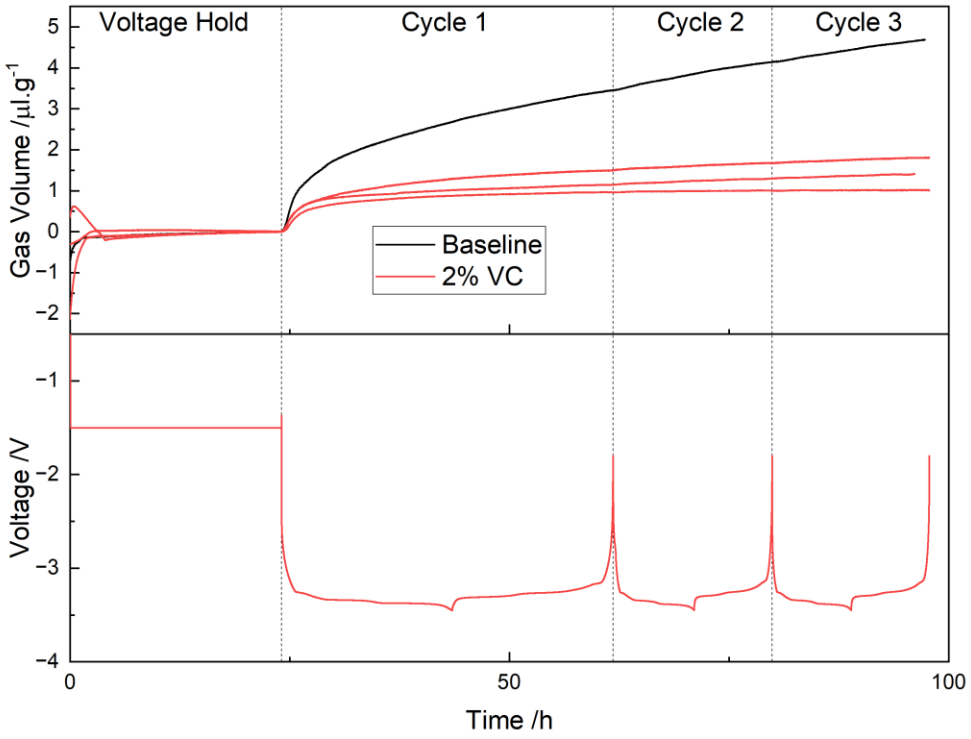

Figure 52 - Gas volumes generated in 2% VC doped electrolyte LFP vs graphite full cells (3 cells) with baseline LP57 cell 211 for comparison. Voltage vs time graph for 2% VC doped cell 236 below for cycling protocol reference.

Figure 52 shows the pressure measurement data from a 2% cell (baseline cell with the addition of 2 wt.% Vinylene Carbonate or VC) is overlaid with the baseline cell data, with electrochemical cycling data from the 2% VC cell stacked below. Here in this figure, 2% VC displays its ability to suppress the amount of gas evolution in all cycles, where in cycle 1, 1.17 ±0.29 μlg^{-1} of gas evolved (baseline: 3.64 ±0.49 μlg^{-1}), cycle 2+3 with 0.90 ±0.14 μlg^{-1} (baseline: 1.09 ±0.13 μlg^{-1}). From these values, it is clear that the presence of 2% VC has a significant effect on the gas evolution reactions that occur, which is in line with literature, where VC is known to preferentially react with the graphite surface prior to the electrolyte components, creating an SEI layer with improved properties [91, 132]. VC preferentially reacting at the graphite surface would mean that a protective layer would be formed, prior to the reduction of the electrolyte components, resulting in less gaseous products being formed, thus less gas evolution in the initial cycles, as seen in cycle 1 in Figure 52. Furthermore, the improved properties of the SEI would also explain the observed gas evolution behaviour in cycle 2+3, where the improved passivating properties of the SEI layer would prevent further decomposition of the electrolyte, as evidenced by the decreased gas evolution in comparison to the baseline electrolyte.

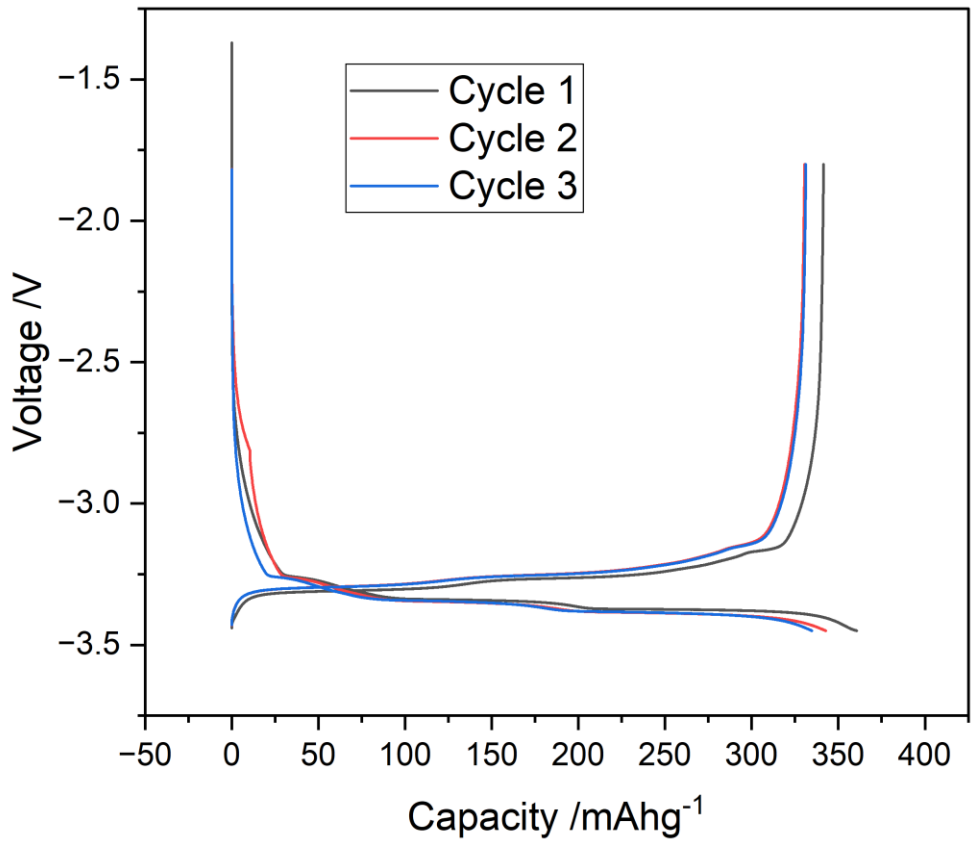

Figure 53 - Voltage vs capacity graph for a 2% VC doped electrolyte LFP vs graphite full cell (cell 236), showing a good profile that is very comparable with baseline LP57.

	Discharge Capacity /mAhg^{-1}			Coulombic Efficiency /%		
Electrolyte	Cycle 1	Cycle 2	Cycle 3	Cycle 1	Cycle 2	Cycle 3
Baseline	347.0 ± 1.9	340.1 ± 2.9	340.3 ± 3.0	93.2 ± 0.5	99.0 ± 0.2	99.3 ± 0.1
2% VC	344.5 ± 2.8	333.2 ± 2.3	331.2 ± 1.0	94.7 ± 0.2	98.5 ± 1.8	98.5 ± 0.5

Table 8 - Discharge capacity and Coulombic efficiency values per cycle for 2% VC additive doped electrolyte LFP vs graphite cell, with the baseline LP57 values for comparison. Errors calculated from the standard deviation of 3 repeats.

Figure 53 shows the voltage vs capacity graph for a 2% VC cell, where the expected capacity profile is shown, highlighting how the addition of VC does not significantly affect the operation of the cell. In cycle 2, we see a slight deviation from expectations, where the profile (red line) should be overlapped with cycle 3 profile (blue line). This deviation suggests a side reaction occurred, as shown by the slightly increased charge capacity.

Table 8 summarises the electrochemical data from the VC cell, where during cycle 1, a first cycle discharge capacity of 344.5 ±2.8 mAhg^{-1}, and a first cycle coulombic efficiency of 94.7 ±0.2%. The electrochemical performance of VC cells seemed to show a small decrease in first cycle discharge capacity (difference of ~2.5 mAhg^{-1}) but an increase in first cycle coulombic efficiency (difference of ~1.5%). This is unexpected as decreases in first cycle discharge capacity is normally associated with side reactions which would also be reflected in a decrease in coulombic efficiency. It is currently unclear why this is the case.

This decrease in first cycle discharge capacity compounded with the gas evolution behaviour in suggests that the VC is electrochemically reacting at the graphite surface but not generating gas, the loss in discharge capacity is likely caused by the presence of additional side reactions or the reduction of VC. Lundström et al. investigated the possible reaction pathways for VC reduction at the graphite surface, where they found that the polymerisation of VC is the likely reaction pathway, which itself does not generate gas [133].

In cycle 2+3 in Table 8, we see that the cell achieves a discharge capacity of 333.2 ±2.3 mAhg^{-1} and 331.2 ±1.0 mAhg^{-1} The discharge capacity of both cycle 2+3 for the VC cell is interestingly lower than that of the baseline cell, which is unexpected as the VC additive is known in literature for improving the performance of the cell, especially in later cycles. Due to the cycling protocols, it is possible that the benefits of the VC additives cannot be observed within the few cycles within our protocol. As shown in literature, VC provides improvement to long term capacity retention rather than immediate increases in achievable discharge capacity value [90-92, 95].

Therefore, observing a small decrease in discharge capacity in comparison to the baseline, does not necessarily indicate that VC is a poor performing additive but rather it is a trade-off where the benefits come from later cycles.

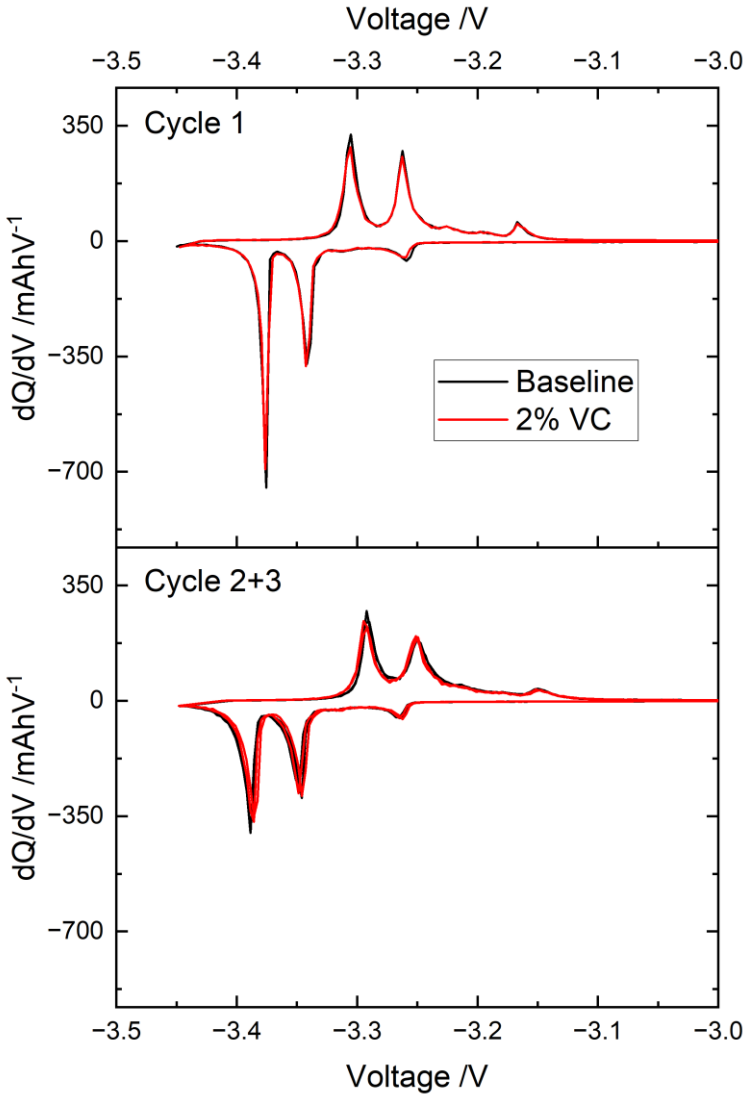

Figure 54 - dQ/dV vs voltage graph for 2% VC doped LP57 electrolyte LFP vs graphite full cell (Cell 236) compared with baseline LP57 cell 211.

The small decrease in coulombic efficiency is also observed in cycles 2+3, where VC cells have efficiencies of 98.5 ±1.8% and 98.5 ±0.5%. This could possibly represent additional side reactions occurring at the graphite surface. However, from the gas evolution behaviour seen in Figure 52, it is more likely that the VC is still preferentially reacting at the graphite surface rather than the electrolyte, as the gas evolution remains lower than the baseline cell. If we assume the reduction of VC does not generate gas, as described by Lundström [133], whilst the reduction of electrolyte components does produce gas, then the preferential reaction of VC over other electrolyte components would mean a decreased gas evolution, which is what is observed in the gas evolution behaviour shown in Figure 52.

The dQ/dV analysis for VC cells can be seen in Figure 54, where the position of the three expected peaks is near identical between VC cells and baseline cells, indicating that the presence of VC within the SEI does not have a significant impact on the lithium intercalation/extraction mechanism.

4.3 Gas Evolution Behaviour with the Introduction of LFO Additive

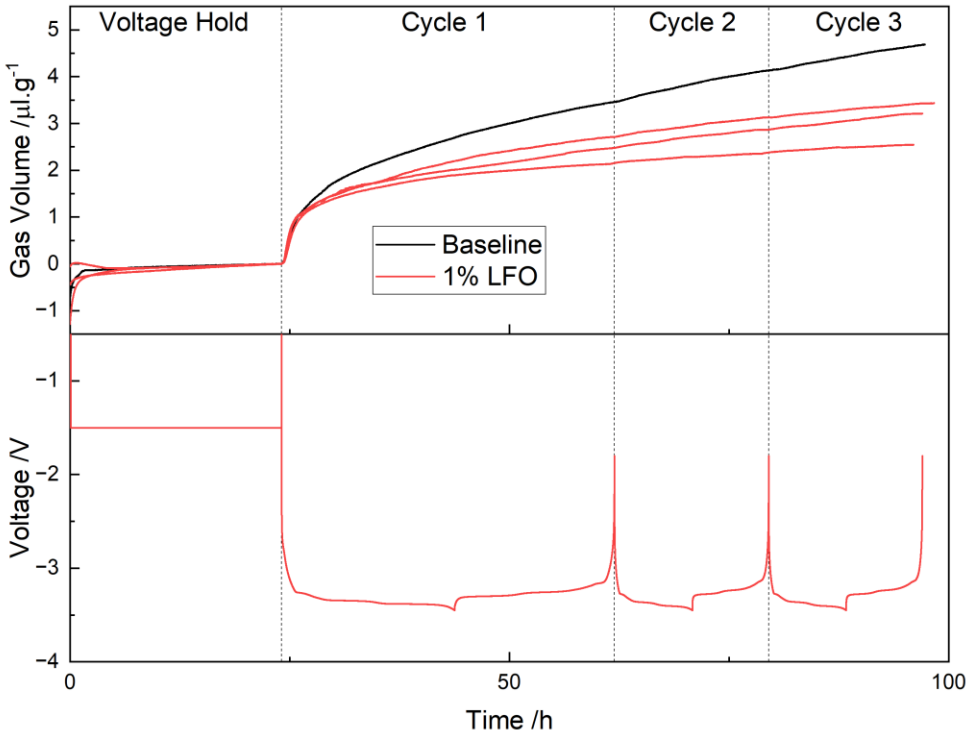

Figure 55 - Gas volumes generated in 1% LFO doped electrolyte LFP vs graphite full cells (3 cells) with baseline LP57 cell 211 for comparison. Voltage vs time graph for 1% LFO doped cell 313 below for cycling protocol reference

Figure 55 shows the gas evolution behaviour of LFO cells, where the LFO cell has 2.44 ± 0.29 μlg^{-1} of gas in cycle 1 and 0.62 ±0.18 μlg^{-1} in cycle 2+3. Within cycle 1, the LFO cell performs very similarly to the baseline cell during the initial stages of cycle 1, indicating that the SEI formation reaction is generating a similar amount of gas. The deviation between the cells occurs after this initial stage, where the LFO cell exhibits a flatter plateau. This flatter plateau supports what is seen in literature, where a decrease in gas volume is expected due to the improved properties of the SEI. This trend continues into cycle 2+3 where we see a small decrease in gas evolved (difference of ~0.47 μlg^{-1}) when compared to the baseline cell, once again supporting the theory of a more resilient SEI that is preventing further reactions of electrolyte components at the graphite surface. This matches well with literature, where work by Ma et al. showed that the use

of 1% LFO decreased gas evolution in NMC532/graphite pouch cells with 1.2M $LiPF_6$ in EC/EMC electrolyte [109].

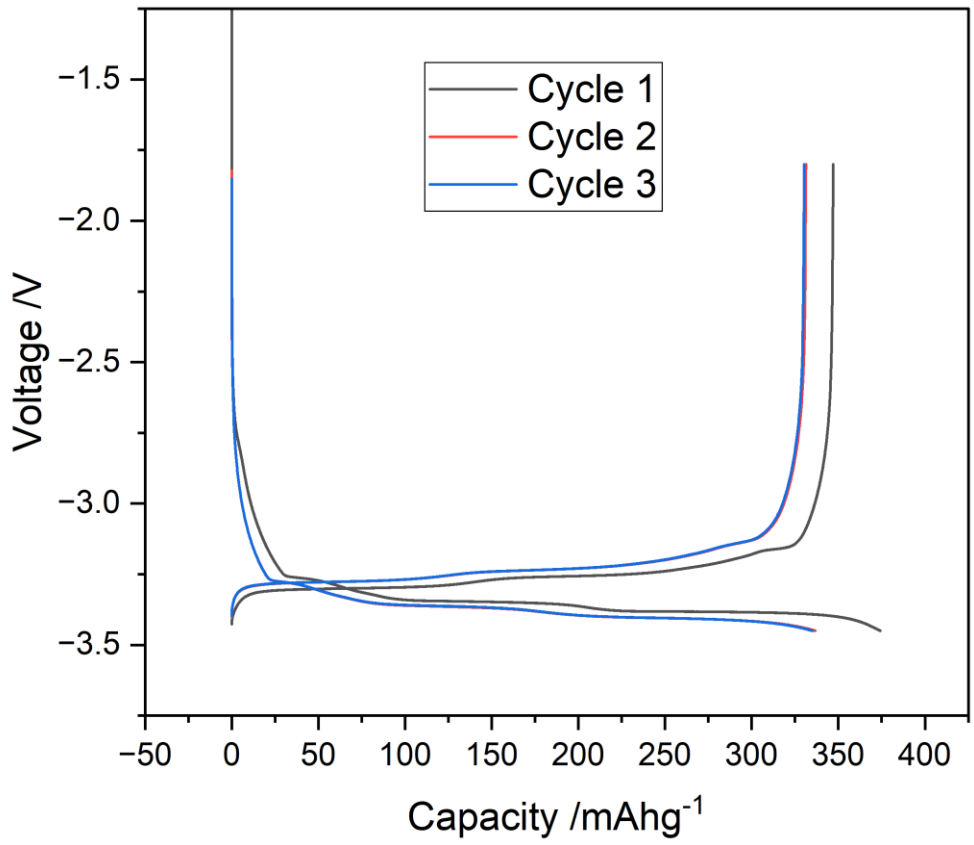

Figure 56 - Voltage vs capacity graph for a 1% LFO doped electrolyte LFP vs graphite full cell (cell 313).

	Discharge Capacity /mAhg^{-1}			Coulombic Efficiency /%		
Electrolyte	Cycle 1	Cycle 2	Cycle 3	Cycle 1	Cycle 2	Cycle 3
Baseline	347.0 ± 1.9	340.1 ± 2.9	340.3 ± 3.0	93.2 ± 0.5	99.0 ± 0.2	99.3 ± 0.1
1% LFO	344.7 ± 3.5	333.6 ± 2.9	333.3 ± 3.0	94.0 ± 0.6	99.0 ± 0.2	99.2 ± 0.2

Table 9 - Discharge capacity and Coulombic efficiency values per cycle for 1% LFO doped electrolyte LFP vs graphite cell, with the baseline LP57 values for comparison. Errors calculated from the standard deviation of 3 repeats.

Figure 56 shows the voltage vs capacity graph for an LFO cell, where the expected profile is shown. No significant differences in shape of the profile between LFO cells and baseline cells were observed. The addition of LFO does not seem to have a significantly detrimental effect on the electrochemical performance of the cell.

From Table 9, the LFO cell obtained a first cycle discharge capacity of 344.7 ±3.5 $mAhg^{-1}$ and a coulombic efficiency of 94.0 ±0.6%. The electrochemical performance of LFO only shows marginal differences to the baseline cell in cycle 1, which matches well with the similarity in first cycle gas evolution behaviour (during the initial stages), indicating no drastic differences between the gas evolution reactions caused by the introduction of the LFO additive. The comparable first cycle discharge capacity indicates that the lithium intercalation mechanism occurring at this C-rate was not impeded by the addition of the LFO, furthermore, the first cycle coulombic efficiency also being very comparable implies that no further side reactions were present. Clearly the reduction of the LFO at the graphite surface and the subsequent SEI layer formed did not have an extensive impact on the first cycle performance of the cell.

The cycle 2+3 electrochemical data in Table 9, the LFO cell show a decreased discharge capacity in both cycles in comparison to the baseline cell, 333.6 ±2.9% and 333.3 ±3.0% for cycles 2 and 3 respectively, whilst still maintaining comparable coulombic efficiencies, 99.0 ±0.2% and 99.2 ± 0.2%. The very high coulombic efficiency values indicate that there is no significant influence of unwanted side reactions that are occurring during cycle 2+3, therefore the explanation for the lower discharge capacity must be due to the ability of the graphite to intercalate and extract lithium ions. It is reasonable to assume that, comparatively to the baseline cell, the SEI formed under the presence of LFO may inhibit the intercalation of lithium ions into the graphite surface, thus decreasing the amount of lithium ions extracted during the discharge phase which results in a lower capacity value. It is known from literature that LFO has long term cycling ability of the cell and may not be evident in the early stages of cycling [106, 107, 109], therefore, to see the advantages of the LFO, cycling beyond our current protocols is necessary. Thus, whilst the decreased discharge capacity in these initial 3 cycles can be seen as detrimental, the long-term impact of LFO additive can still be advantageous.

Examination of the dQ/dV analysis as shown in Figure 57, illustrates that LFO cells having decreased peak heights in both the charging and discharging peaks during all three cycles, which possibility explains the small decrease in discharge capacity in cycle 1, and to a greater extent, the decrease in discharge capacity in cycle 2+3. The peak positions remain fairly similar between the LFO cells and the baseline cells, indicating that the conductivity of the SEI layer formed remains fairly similar. This difference in peak heights but similarity in peak positions could be explained by less lithium utilised for intercalation therefore lower capacities, but the SEI conductivity properties remain the same thus the same peak positions.

When cross examining the electrochemical results with the gas evolution data, it is clear from the decreased gas evolution in cycles 2+3, that the properties of the SEI layer has changed

with the presence of LFO, becoming more resilient to gas evolving reactions. It seems reasonable that whilst the new SEI has obtained advantageous properties, it cannot be ruled out that it hasn't also obtained unfavourable properties too, such as decreased lithium-ion conductivity.

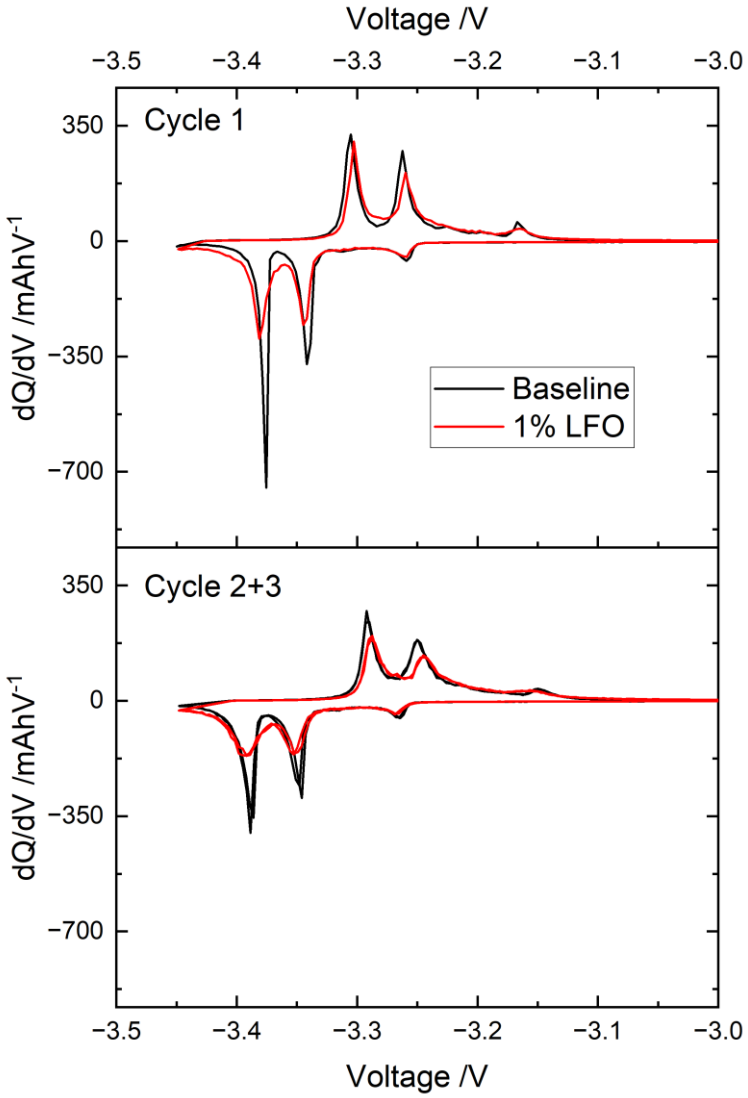

Figure 57 - dQ/dV vs voltage graph for 1% LFO doped LP57 electrolyte LFP vs graphite full cell (Cell 313) compared with baseline LP57 cell 211.

4.4 Gas Evolution Behaviour with the Introduction of DTD Additive

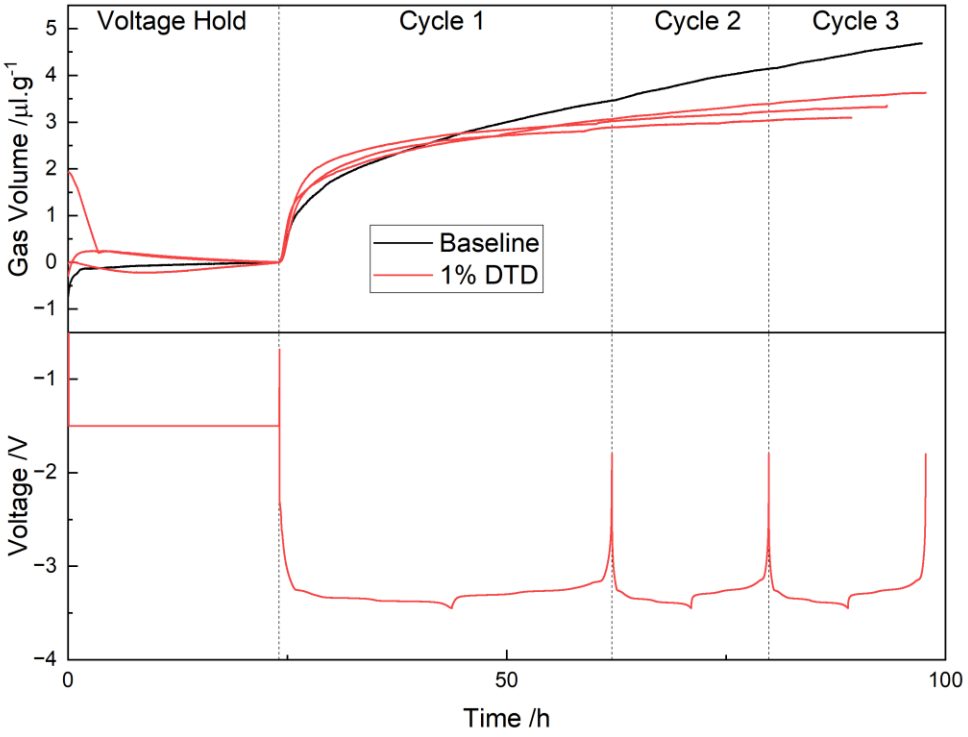

Figure 58 - Gas volumes generated in 1% DTD doped electrolyte LFP vs graphite full cells (3 cells) with baseline LP57 cell 211 for comparison. Voltage vs time graph for 2% VC doped cell 288 below for cycling protocol reference.

In Figure 58, DTD cells have a very similar gas evolution profile to the baseline cell, with the DTD cell producing 2.95 ±0.14 μlg^{-1} of gas in cycle 1 (baseline: 3.64 ± 0.49 μlg^{-1}), with a marginal difference arising in cycle 2+3, where the DTD cell produces 0.41 ±0.14 μlg^{-1} of gas (baseline: 1.09 ±0.13 μlg^{-1}). DTD is expected to react in a similar manner to VC, where it preferentially reacts at the graphite surface prior to the electrolyte compounds to form an improved SEI layer [134] . Despite this similarity, the gas evolved during cycle 1 does not seem to be significantly reduced with the presence of DTD, implying that either the electrolyte compounds continue to be reduced at the surface, or that the reduction of DTD compounds also generates gaseous products to a degree like that of the baseline cell. A decrease in gas evolution is only observed at the end of cycle 1 and during cycle 2+3, highlighting the improved performance of the SEI layer where further gas evolution reactions are inhibited, which is line with the expectation of a more stable and protective SEI layer. The gas evolution behaviour for LFO cells matches well with literature where Xia et al. showed that the addition of DTD additive to NMC111 vs graphite cells led to increased gas evolution during formation that marginally exceeded the control electrolyte, followed by a small decrease in gas evolution (cell volume decreased) [99]. Here, it is possible that the preferential reduction of DTD at the graphite surface prevented the gas evolution caused by

electrolyte decomposition, however the reduction of DTD is thought to produce compounds that can later generate gas [134], thus resulting in no net gain or loss of gas volume.

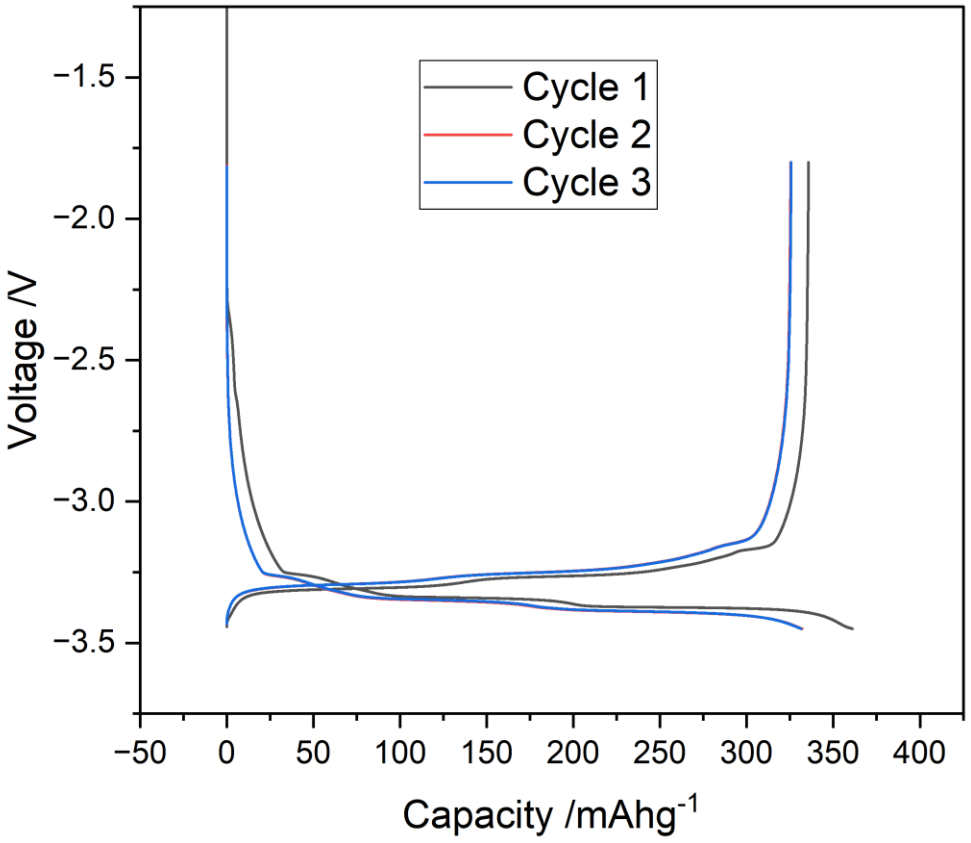

Figure 59 - Voltage vs capacity graph for a 1% DTD doped electrolyte LFP vs graphite full cell (cell 288).

	Discharge Capacity /mAhg^{-1}			Coulombic Efficiency /%		
Electrolyte	Cycle 1	Cycle 2	Cycle 3	Cycle 1	Cycle 2	Cycle 3
Baseline	347.0 ± 1.9	340.1 ± 2.9	340.3 ± 3.0	93.2 ± 0.5	99.0 ± 0.2	99.3 ± 0.1
1% DTD	331.6 ± 9.7	318.4 ± 14.2	318.6 ± 13.6	92.2 ± 1.0	98.3 ± 0.4	98.6 ± 0.5

Table 10 - Discharge capacity and Coulombic efficiency values per cycle for 1% DTD doped electrolyte LFP vs graphite cell, with the baseline LP57 values for comparison. Errors calculated from the standard deviation of 3 repeats.

Figure 59 shows the voltage vs capacity graph of a DTD cell, where the expected graph profile is shown, indicating that the addition of DTD does not significantly impact the operation of the cell.

When examining the discharge capacities of the DTD cell in Table 10, we see that the DTD cell shows a lower cycle 1 discharge capacity of 331.6 ±9.7 $mAhg^{-1}$ (decrease of ~15.4 $mAhg^{-1}$ compared to baseline) , as well as lower discharge capacities in cycle 2+3 of 318.4 ±14.2 $mAhg^{-1}$ and 318.6 ±13.6 $mAhg^{-1}$ respectively (decrease of ~21.6 $mAhg^{-1}$ compared to baseline in both cycles) . The presence of DTD seems to reduce the amount of lithium available for extraction in the discharge step, the cause of this is unclear. It is possible that the SEI formed under the presence of DTD, whilst being stable and protective, may have decreased ionic conductivity therefore less lithium is intercalated into the graphite during the charging step.

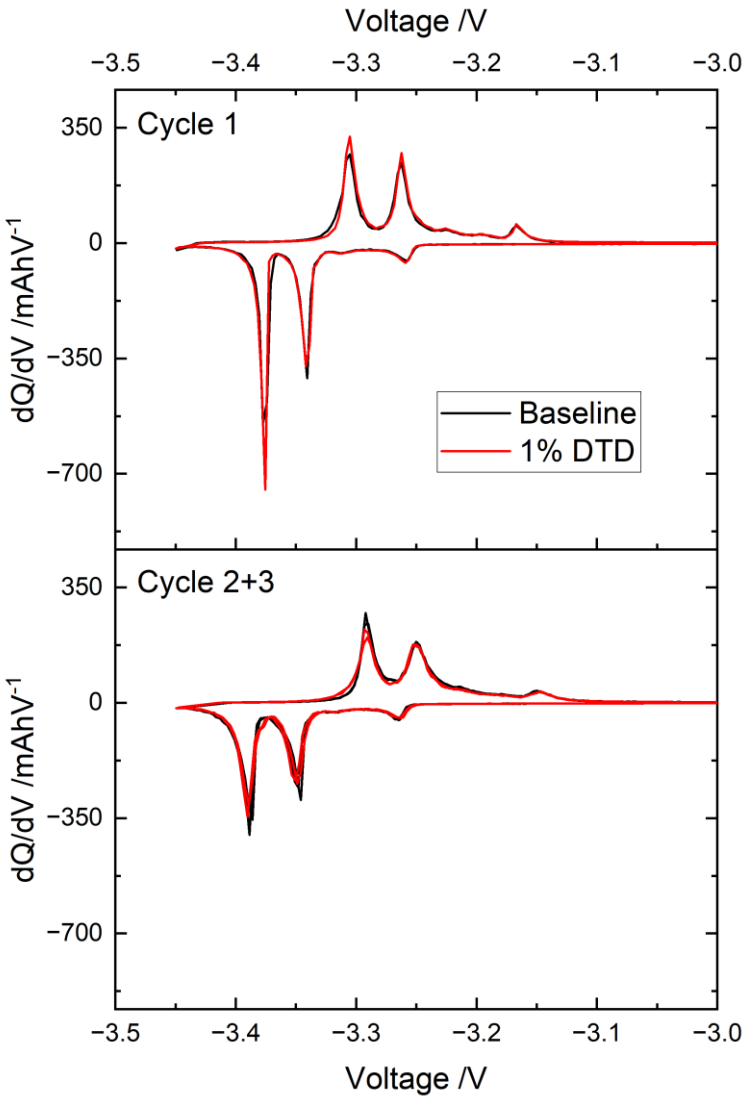

Figure 60 - dQ/dV vs voltage graph for 1% DTD doped LP57 electrolyte LFP vs graphite full cell (Cell 288) compared with baseline LP57 cell 211.

This is theory is further reinforced when examining the coulombic efficiencies of the DTD cell, as shown in Table 10. DTD achieves an efficiency of 92.2 ±1.0% in cycle 1, 98.3 ±0.4% and 98.6 ±0.5% in cycles 2+3 respectively, which is very similar to the baseline cell values (less than 1% difference). The similarity in coulombic efficiencies between these cells indicates that the DTD cell

is not introducing any new side reactions that contribute to the charge or discharge capacities, as this would result in a decrease in coulombic efficiencies in comparison to the baseline cell. This trend is particularly important in cycles 2+3, where the SEI formation reaction is no longer as prevalent, therefore a near 100% coulombic efficiency is expected, where most of the capacity gained during the charge step is expected to be discharged in the discharge step. This is what we observe in the electrochemical data, indicating the intercalation/extraction of lithium is operating without the presence of significant side reactions. Instead, a decreased ionic conductivity in the SEI, as described above, would explain the trends seen in cycle 2+3.

The dQ/dV analysis for DTD cells can be seen in Figure 60, where the position of the three expected peaks is near identical between DTD cells and baseline cells. This contradicts our previous theory that the SEI layer may have decreased ionic conductivity as this would result in a peak shift being present. Clearly another factor is involved in reducing the decreased discharge capacity.

4.5 Gas Evolution Behaviour with the Introduction of VC and DTD Additives

Figure 61 shows the gas evolution behaviour of DTD+VC cells, with the DTD+VC cells producing 1.94 ±0.29 μlg^{-1} amounts of gas in cycle 1, and 0.15 ±0.08 μlg^{-1} in cycle 2+3. From these figures, DTD+VC shows a decreased amount of gas evolved in cycle 1 in comparison to the baseline cells (~1.70 μlg^{-1}) indicating that the presence of the additive combination is effective in reducing the amount if gas evolution during the SEI formation reaction. Furthermore, the decrease in gas evolution in cycle 2+3 indicates that the SEI formed with the reduction products of both VC and DTD is more effective at preventing further electrolyte decomposition than the baseline.

This is in line with literature, where we expect DTD+VC combination to generate a slightly decreased amount of gas compared to the baseline [99]. This gas evolution suppression continues during the later stages of cycle 1 and throughout cycles 2+3, as shown by the very flat plateau and the low amounts of gas evolved for each cycle, highlighting the modified SEI's ability to prevent further electrolyte reductions at the graphite surface.

Figure 62 shows the voltage vs capacity graph for a DTD+VC cell, where the graph profile does not exhibit any abnormalities, therefore shows that the addition of DTD+VC does not significantly impede the cell's ability to undergo electrochemical cycling.

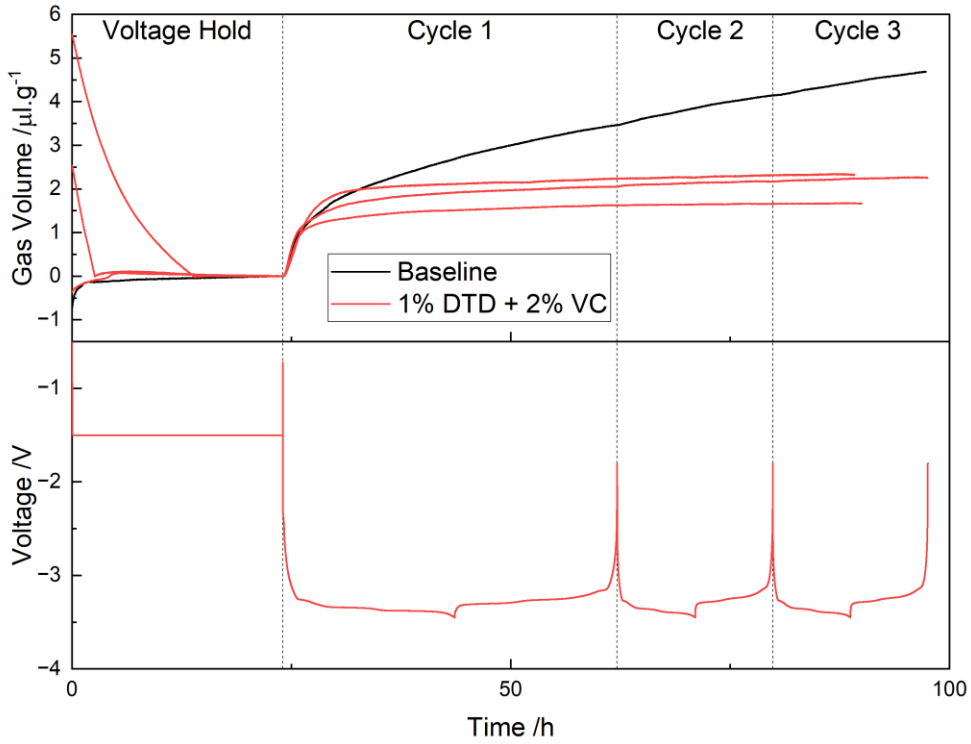

Figure 61 - Gas volumes generated in 1% DTD + 2% VC doped electrolyte LFP vs graphite full cells (3 cells) with baseline LP57 cell 211 for comparison. Voltage vs time graph for 1% DTD + 2% VC doped cell 299 below for cycling protocol reference.

Table 11 shows the discharge capacities and coulombic efficiencies from the DTD+VC cells, where the DTD+VC cell shows a slightly lower cycle 1 discharge capacity of 340.7 ±4.6mAhg^{-1}, which is ~6.3 mAhg^{-1} less than the baseline cells. Clearly the presence of DTD+VC is disturbing the lithium intercalation/extraction reaction during the first cycle; examining the first cycle coulombic efficiency, the DTD+VC cell shows a very similar value to the baseline cell, DTD+VC: 93.5 ±1.3% and baseline: 93.2 ±0.5%, indicating that no significant additional side reactions are occurring. The combination of a lower discharge capacity with a similar coulombic efficiency implies that the loss of discharge capacity is likely due to the modified SEI once again not being able to facilitate lithium intercalation/extraction in the same manner as the baseline cell's SEI. This again could be attributed to comparatively poorer ionic conductivity properties within the modified SEI layer. From the gas evolution data, it is clear that the SEI layer has been successfully modified, as evidenced by the decreased gas evolution in all three cycles, therefore it is possible that the new SEI layer may also have the trade-off where an increase in electrolyte decomposition resilience comes with a lower ionic conductivity.

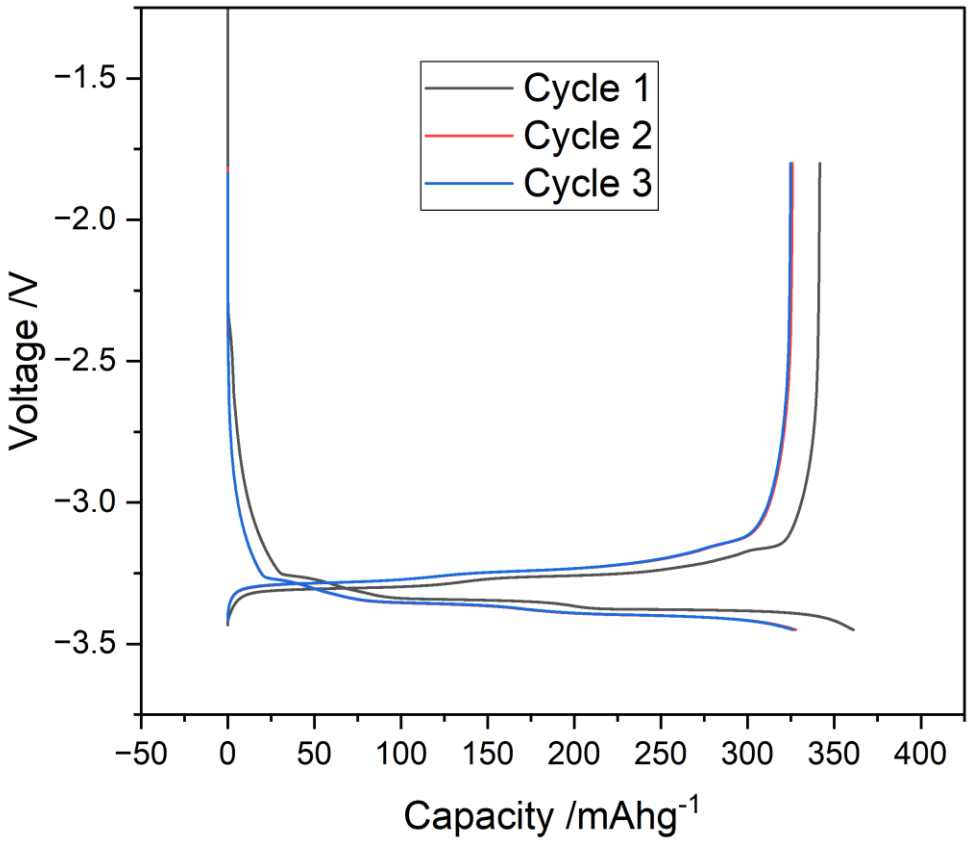

Figure 62 - Voltage vs capacity graph for a 1% DTD + 2% VC doped electrolyte LFP vs graphite full cell (cell 299).

	Discharge Capacity /mAhg^{-1}			Coulombic Efficiency /%		
Electrolyte	Cycle 1	Cycle 2	Cycle 3	Cycle 1	Cycle 2	Cycle 3
Baseline	347.0 ± 1.9	340.1 ± 2.9	340.3 ± 3.0	93.2 ± 0.5	99.0 ± 0.2	99.3 ± 0.1
1% DTD + 2% VC	340.7 ± 4.6	328.1 ± 7.7	327.6 ± 8.1	93.5 ± 1.3	99.0 ± 0.4	99.2 ± 0.4

Table 11 - Discharge capacity and Coulombic efficiency values per cycle for 1% DTD+ 2% VC doped electrolyte LFP vs graphite cell, with the baseline LP57 values for comparison. Errors calculated from the standard deviation of 3 repeats.

When examining the cycle 2+3 in Table 11, this trend continues, where the discharge capacities are lower than the baseline counterpart. DTD+VC cells had 328.1 ± 7.7 mAhg^{-1} and 327.6 ±8.1 mAhg^{-1} (difference of ~12 mAhg^{-1} in comparison to baseline). The addition of the DTD+VC additives may have caused side reactions that reduced the discharge capacities within the cell. Analysis of the corresponding coulombic efficiency however does not match the discharge capacities for cycle 2+3, where they are very similar to the baseline cell values. DTD+VC

cells had 99.0 ±0.4% and 99.2 ±0.4%. The pressure measurements match the coulombic efficiency well as we see the gas evolution is suppressed within cycle 2+3 very effectively, indicating a lack of side reactions, thus supporting our theory of the modified SEI layer being more resilient but also possessing less ionic conductivity.

The dQ/dV analysis for DTD+VC cells can be seen in Figure 63, where we see a slight peak shift in cycle 1 between DTD+VC cells and the baseline, and a significant peak shift in cycles 2+3. This is interesting as the dQ/dV analysis for DTD cells and VC cells did not show any noticeable peak shifts, yet the combination of the two additives subsequently causes a peak shift, indicating an increase in resistance in the SEI layer which supports the observations in the discharge capacity and coulombic efficiency.

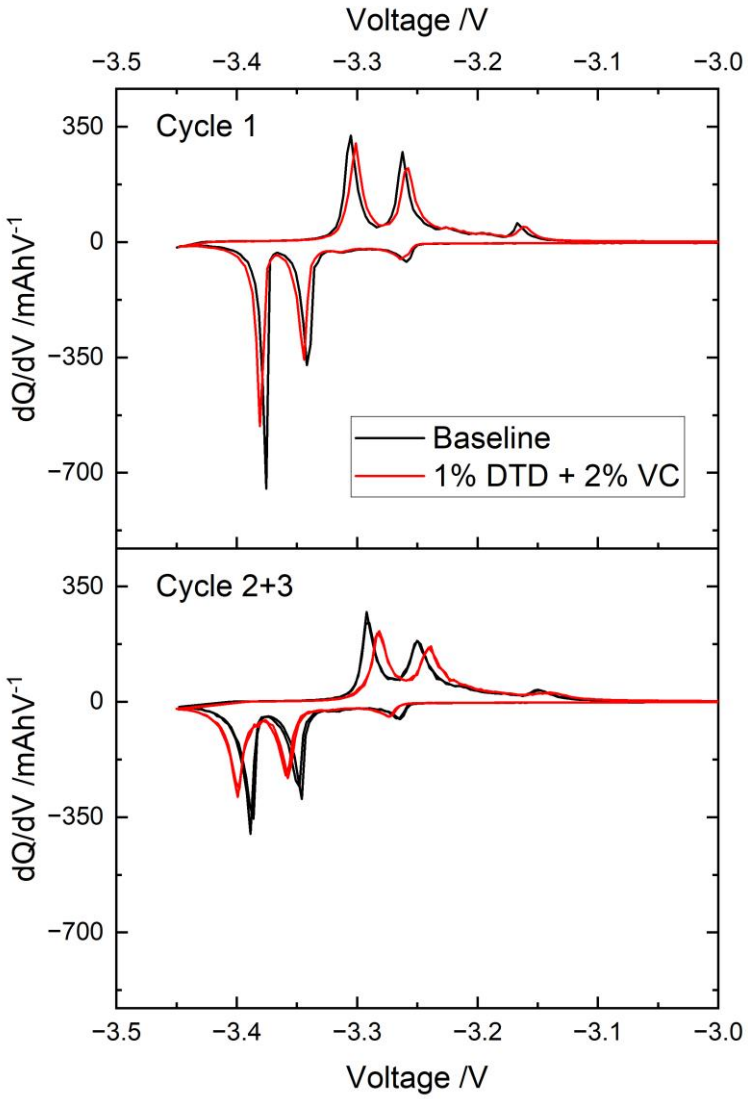

Figure 63 - dQ/dV vs voltage graph for 1% DTD + 2% VC doped LP57 electrolyte LFP vs graphite full cell (Cell 299) compared with baseline LP57 cell 211.

4.6 Comparison of Gas Evolution Behaviour of the Electrolyte Additives

Figure 64 and Figure 65 compares the gas evolution data from all the investigated additives, with the electrochemical cycling data of the baseline cell for reference. From this, we firstly observe that all the electrolyte additives are able to suppress the amount of gas produced during cycling.

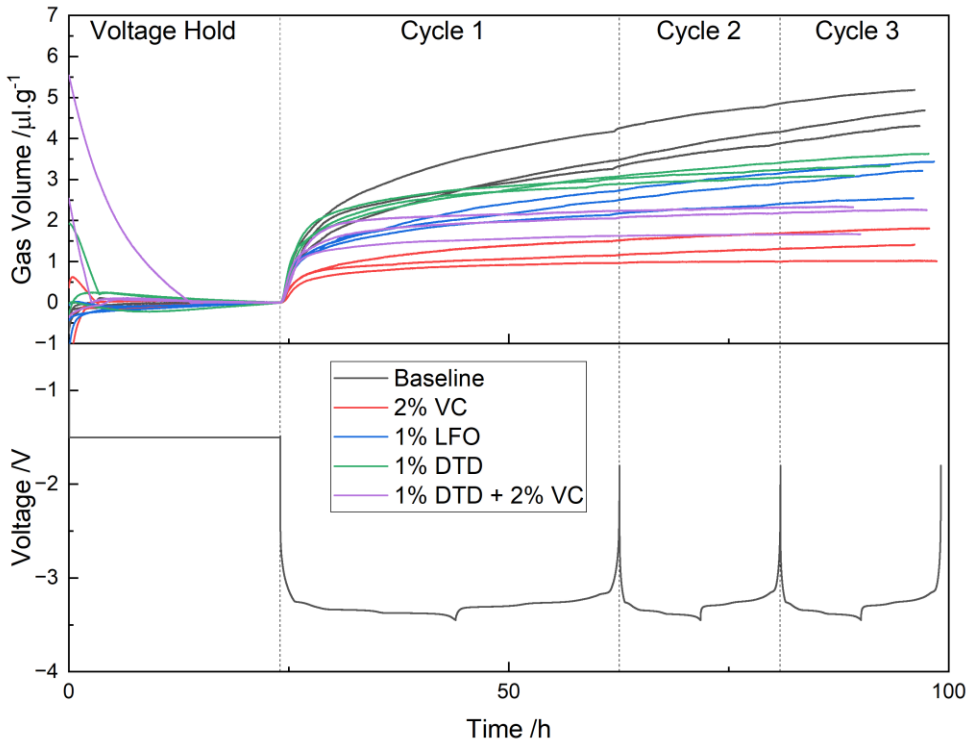

Figure 64 - Comparison of gas volumes generated in additive doped electrolyte LFP vs graphite full cells with baseline LP57 cells. Voltage vs time graph for baseline LP57 cell 211 below for cycling protocol reference.

When comparing the gas evolution data from cycle 1 between the additives, VC seems to be the best in reducing gas evolution generating 1.17 ±0.29 μlg^{-1} of gas during cycle 1. This is especially clear during the SEI formation stage, as evidenced by a significantly smaller sharp initial increase in pressure. Clearly the presence of the VC additive is very influential on the SEI formation reaction and is able to suppress the reduction of electrolyte components more so than the other additives. This is unsurprising as VC has long been the industry standard as an electrolyte additive and is already widely used.

DTD +VC was then the next best performing additive with respect to reducing gas evolution during cycle 1 producing 1.94 ±0.29 μlg^{-1}. Similar to VC, it is seen again that the incorporation of the DTD+VC additive is able to reduce the amount of gas generated during the SEI formation reaction, more so than DTD and LFO cells. DTD and VC are expected to have opposing effects on

the gas evolution behaviour [99], where DTD is expected to generate gas during cycle 1 in comparison to the baseline, whilst VC is meant to reduce the amount of gas produced. Interestingly, the combination of the additives results in a net reduction of gas evolution, indicating that the gas suppression ability of VC outweighs the gas produced from DTD reduction.

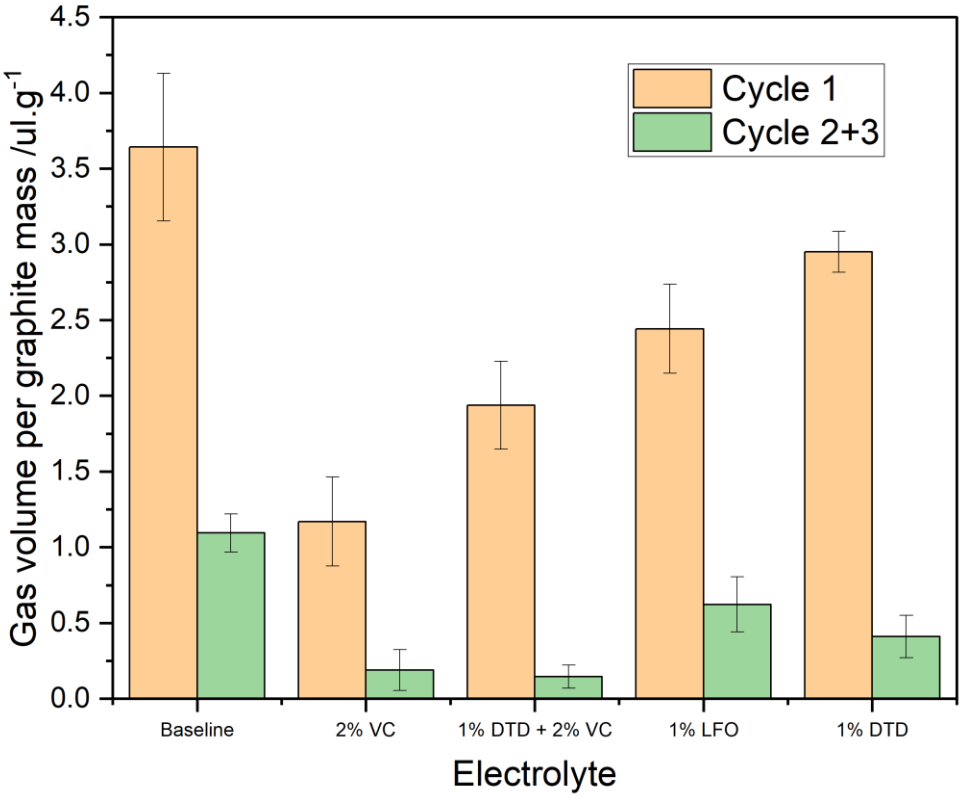

Figure 65 - Comparison of average total gas volumes during each cycle between additive doped electrolyte LFP vs graphite full cells with baseline LP57 cells. Errors calculated from standard deviation in 3 repeats per electrolyte.

LFO cells, during cycle 1, produced 2.44 ±0.29 μlg^{-1} amount of gas, which is more than VC and DTD+VC cells and less than DTD cells. As described in the introduction, SEI layers formed without the use of additives typically contain $Li_xPO_yF_z$ compounds [107]; by adding LFO additive to the electrolyte, it is possible to increase the $Li_xPO_yF_z$ content within the SEI which has shown to reduce gas evolution and improve cycling performance [109]. This is markedly different to how VC and DTD operate, where their reduction products introduce entirely new components to the SEI layer.

DTD cells (without the VC), during cycle 1, produced 2.95 ±0.14 μlg^{-1} of gas, which is the most out of all the electrolyte additives. This is expected as according to literature DTD is the only additive to generate additional gas volumes in comparison to the baseline [99].

Once again, from examining the gas evolution data in cycle 2+3 from Figure 64 and Figure 65, it is clear that all the electrolyte additive cells were capable of forming a stable SEI layer that could reduce gas evolution in comparison to the baseline.

From the cycle 2+3 data, VC and DTD+VC show a similar gas volume evolved, where VC cells produced 0.19 ±0.14 μlg^{-1} of gas and DTD+VC produced 0.15 ±0.08μlg^{-1}. This is interesting as the cycle 1 gas evolution data suggests that the difference in gas suppression abilities of the SEI layer was substantial between the additives, however gas evolution in cycle 2+3 suggests that the fully formed SEI layers are equally capable of preventing EC decomposition once fully formed. Clearly in the case of VC and DTD+VC cells, the choice of additive is more impactful in the initial SEI formation reaction rather than later on, where the SEI has been fully formed. To investigate this further, it is important to cross-examine this data with DTD cells to gain a better understanding of the relative impact of each additive. DTD cells, in cycle 2+3, produced 0.41 ±0.14 μlg^{-1} amount of gas, which is more than both the VC and DTD+VC cells, mirroring the behaviour seen in cycle 1. This once again suggests that the DTD reduction products are less effective than the VC reduction products at preventing further gas evolution. This behaviour correlates well with our expectations, since the addition of DTD is expected to increase gas evolution in comparison to VC [99] and DTD reduction products may also further react at the graphite surface to generate additional gas [134].

The cycle 2+3 gas evolution data for LFO showed that the cells produced 0.622 ±0.18 μlg^{-1} of gas, which is greater than all the other additives. The increased gas volume is expected when compared with VC and DTD+VC as this mimics the behaviour observed in cycle 1, however when comparing to DTD cells, LFO now produces more gas during these later cycles. This implies that LFO whilst better at reducing gas evolution during the SEI formation reaction, creates an SEI layer that is less effective at preventing further reaction of electrolyte components at the graphite surface. This however is a tentative theory, as mentioned earlier, the differences in gas volumes between the cells are quite small in comparison to cycle 1, therefore the differences in values may not be indicative of what is occurring.

When considering what is occurring mechanistically between the additive choices and how it affects the gas evolution behaviour, it is important to firstly consider at which potential they are reduced. EC is a key electrolyte component that is reduced at the graphite surface to form the SEI, this occurs at <0.8V vs Li/Li^+ [133]. VC is reduced at >1V vs Li/Li^+ [133] and DTD is reduced >0.9V vs Li/Li^+ [134], meaning both will preferentially react at the graphite surface prior to EC. By reacting at the graphite surface prior to EC, it prevents the gas evolution that would otherwise occur from the reduction of EC. This was seen in the VC cells where in cycle 1 the gas evolution was significantly

lower. Whilst DTD also preferentially reacted before EC, the reaction pathway of DTD is expected to generate gas which is why we see no reduction in gas evolution for DTD cells during cycle 1. The reduction of LFO overlaps with EC reduction potentials at 0.6 V vs Li/Li^+ [106] therefore will likely be reduced at the same time as EC. Thus, LFO cells are expected to generate more gas than VC and DTD+VC cells as it is unable to preferentially react and form an SEI layer prior to the EC reduction.

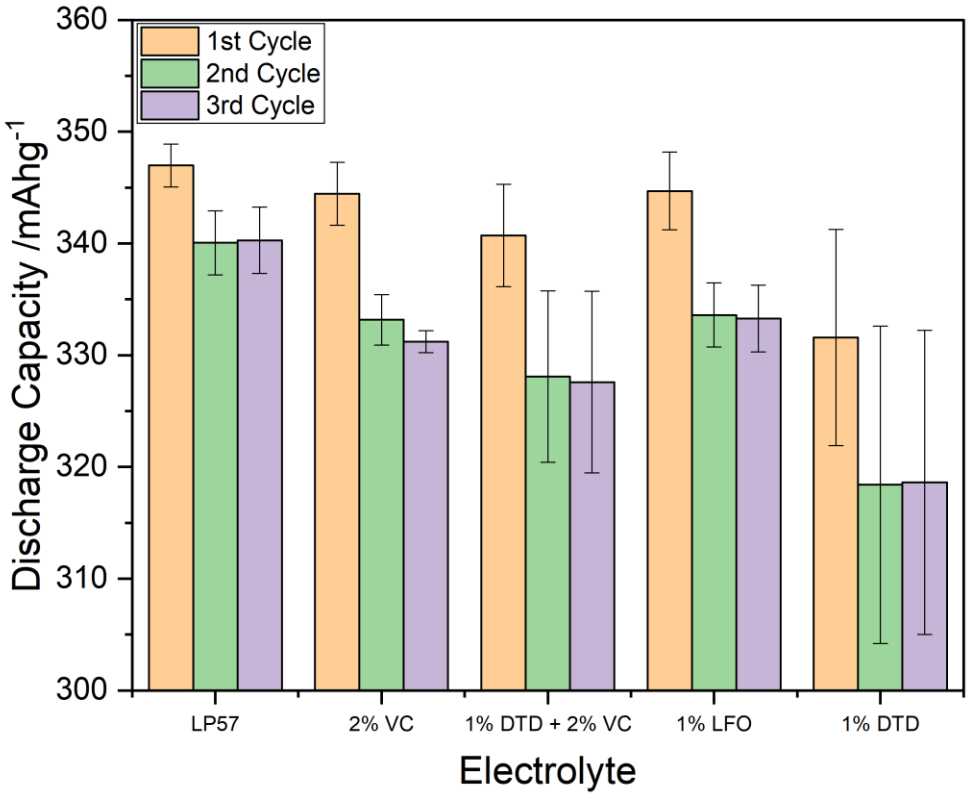

Figure 66 - Comparison of average discharge during each cycle between additive doped electrolyte LFP vs graphite full cells with baseline LP57 cells. Errors calculated from standard deviation in 3 repeats per electrolyte.

Secondly, it is important to consider the reduction products of the additives that will make up the SEI layer on the graphite surface. VC is thought to polymerise upon reduction to form poly(VC) compounds and Li_2CO_3 [135]. DTD undergoes a two-step reduction where DTD is first reduced to LiDTD and then undergoes a second reduction causing the ring-opening of LiDTD to form $LiO_2SOCH_2CH_2Oli$ (Li_2DTD) which can spontaneously decompose or react to give a variety of compounds [106]. Finally, LFO is thought to be reduced to create inorganic compounds that contain P and F as Li_3PO_4 and LiF [106]. The reduction products are important in determining gas evolution behaviour in later stages of cycling as they will determine the robustness of the SEI layer and its ability to suppress further decomposition of the electrolyte components. The composition of the SEI and its effect on gas evolution is still very much unclear and remains a complex mystery,

however, there is a clear difference in impact between the additives on the SEI layer and therefore the difference in SEI composition remains an important topic.

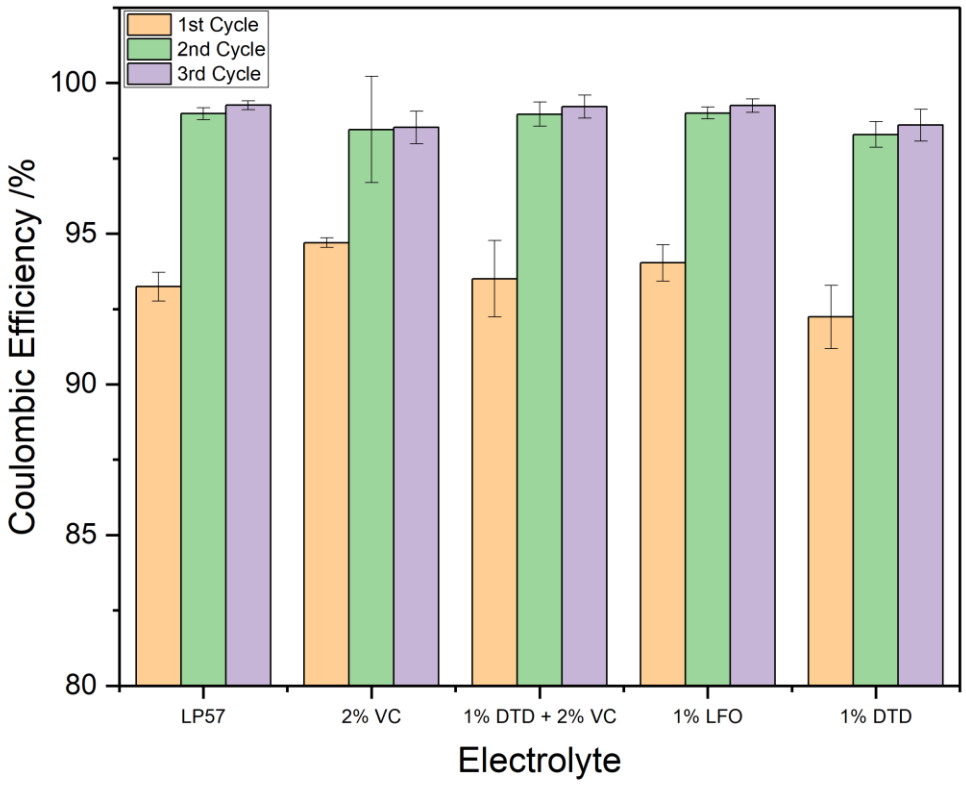

Figure 67 - Comparison of average coulombic efficiency during each cycle between additive doped electrolyte LFP vs graphite full cells with baseline LP57 cells. Errors calculated from standard deviation in 3 repeats per electrolyte.

When analysing cycle 1 discharge capacities in Figure 66, VC, DTD+VC, and LFO show very comparable values of 344.5 ±2.8 $mAhg^{-1}$, 340.7 ±4.6 $mAhg^{-1}$, and 344.70 ±3.5 $mAhg^{-1}$ respectively, all of which are very similar the baseline cell of 347.0 ± 1.9 $mAhg^{-1}$, indicating that SEI formed in the presence of these additives do not seem to have an adverse effect on intercalation of lithium ions into the graphite at this stage of the cycling. This result is unexpected as the gas evolution data suggests that the SEI formation reaction is significantly different between the additives which in theory should lead to a difference in electrochemical performance, but the discharge capacity indicate that despite the differences in gas evolution, the lithium intercalation reactions for these additives remain similar.

Literature has shown that in the case of these additives, it often takes many cycles before the differences between electrochemistry can be observed [102, 136], therefore the cycling protocol within this project may not be adequate for examining electrochemical performance differences.

The only exception being the DTD cells, where discharge capacities in all cycles seem to be slightly lower than the other additives, for example in cycle 1 DTD achieves 331.6 ±9.7 $mAhg^{-1}$ which is ~15 $mAhg^{-1}$ less than the baseline. This correlates well with the gas evolution data, where the increased gas evolution during all cycles can be attributed to a poorly formed SEI layer. This further reinforces the theory that DTD is less effective in creating a stable and passivating SEI layer, at least in comparison to VC and DTD+VC cells, as this poor performing SEI layer would result in increased decomposition of EC molecules at the graphite surface, causing an increase in gas evolution and a decrease in discharge capacity.

When examining the discharge capacities in cycle 2+3 from Figure 66, we see that all the additives show a decreased discharge capacity, with DTD having the lowest. VC having 333.2 ± 2.3 $mAhg^{-1}$ and 331.2 ± 1.0 $mAhg^{-1}$, LFO having 333.6 ± 2.9 $mAhg^{-1}$ and 333.3 ± 3.0 $mAhg^{-1}$, DTD having 318.4 ± 14.2 $mAhg^{-1}$ and 318.6 ± 13.6 $mAhg^{-1}$, DTD+VC having 328.1 ± 7.7 $mAhg^{-1}$ and 327.6 ± 8.1 $mAhg^{-1}$. The difference in discharge capacity in cycle 2+3 is most likely due to the different reactions that are occurring with the additives and subsequently the different SEI layer composition that is formed, which would then impact the lithium intercalation/extraction mechanism resulting in different discharge capacities.

Figure 67 shows the coulombic efficiency per cycle for each additive. It is clear that the difference in coulombic efficiency between additives is relatively small, with each additive having 1-2% difference between them in all cycles. For cycle 1, VC achieves 93.2 ± 0.5%, LFO achieves 94.0 ± 0.6, DTD achieves 92.2 ± 1.0, and DTD+VC achieves 93.5 ± 1.3. In cycle 2 and 3, VC achieves 98.5 ± 1.8% and 98.5 ± 0.5%, LFO achieves 99.0 ± 0.2% and 99.2 ± 0.2%, DTD achieves 98.3 ± 0.4% and 98.6 ± 0.5%, and DTD+VC achieves 99.0 ± 0.4% and 99.2 ± 0.4%. Furthermore, all additives have relatively similar coulombic efficiencies compared to the baseline, indicating that the presence of the additives do not invoke any additional unwanted side reactions at any stage of the cycling.

4.7 Summary

In this chapter, 3 additive candidates were added to the baseline LP57 electrolyte, which were then used in LFP vs graphite full Swagelok pressure cells, where the gas evolution and electrochemical behaviour during the cycling of these cells were investigated.

From these investigations, all 3 additives were found to be able to reduce gas evolution in comparison to the baseline LP57 cells. However, each additive had distinctly different impacts, not only on the gas evolution behaviour but also the electrochemical performance.

VC was found to be the most effective additive for reducing gas evolution, especially during the SEI formation reaction. Interestingly, the co-addition of DTD seemed to increase the gas volumes produced during cycling. This matches what was seen in literature as DTD is expected to generate gasses during the formation cycle. DTD and LFO alone seem to be less effective in general, with DTD generating the most gas in cycle 1 and LFO generating the most gas in cycles 2+3. It is likely that the difference in SEI composition caused by the different additives also has an effect on the gas evolution behaviour, where all 3 electrolyte additives showed different gassing behaviours in all cycles.

There are small differences in discharge capacity and coulombic efficiencies between the additives, indicating that the different SEI compositions also impact the electrochemical performance. DTD was found to perform marginally worse than the other additives, both in discharge capacity and coulombic efficiency. These differences however are relatively small therefore it is difficult to draw definitive conclusions from them. It may be possible that the differences between the additives is not well represented in our cycling protocols.

There is a disconnect between the gas evolution data and the electrochemical data can be explained by the different reaction pathways of the electrolyte additives. Previously, EC within the electrolyte would be reduced at the graphite surface thus generating gas and consuming charge, therefore a clear correlation between increased gas evolution would mean decreases in cell performance. However, with the introduction of the additives, where they have additional reactions that may not produce gas (such as the polymerisation of VC), the correlation between consuming charge and generating gas is no longer true.

Overall, this chapter has given key insight on the relative impact of the 3 additive candidates on the gas evolution and electrochemical behaviour, thus allowing these results to be used as a reference point for further work in this project.

Chapter 5 Investigation Into the Effects of Electrolyte Additives with the Co-Addition of Manganese Ions on Gas Evolution Properties of Graphite Electrodes

5.1 Context

As discussed previously, NMC cathode materials are prone to degradation which can lead to transition metal dissolution, leading to Ni, Mn, Co ions being present within the electrolyte and subsequently on the graphite surface [11, 85, 118]. In chapter 3, it was determined that Mn ion dissolution had the most significant impact, with drastically increased gas volumes produced and substantial decrease in electrochemical performance. Furthermore, we have previously noted that the use of additives is common within industry to help improve the performance of lithium-ion batteries, with different additive choices resulting in different effects[10, 86, 137]. In chapter 4, different electrolyte additives were investigated and found that VC, DTD, DTD+VC, and LFO additives were all capable of reducing the gas volume produced during cycling.

Here in this chapter, the SEI stabilising effects of the choice additives will be investigated specifically with the presence of Mn ions dissolved into the electrolyte. The additive's ability to suppress the negative impact of Mn dissolution will be examined and compared, with a focus on the behaviour during the SEI formation stage of cycling.

Additionally, a previous study showed that the presence of VC lessened the disruption of the graphite SEI caused by Mn, as revealed by a reduction in the associated gas formation [83]. In this work, the study of additives with the co-addition of Mn, is done again with VC and extended to two other classes of additives (DTD and LFO), which are also known to enhance performance [102, 138]. The results provide new understanding of the SEI stabilising properties of the additives in the presence of SEI-disrupting transition metal ions, thus bringing new insights towards the rational development of additive combinations for high performance batteries.

5.2 Gas Evolution Behaviour with the Introduction of VC Additive with the Co-Addition of Manganese Ions

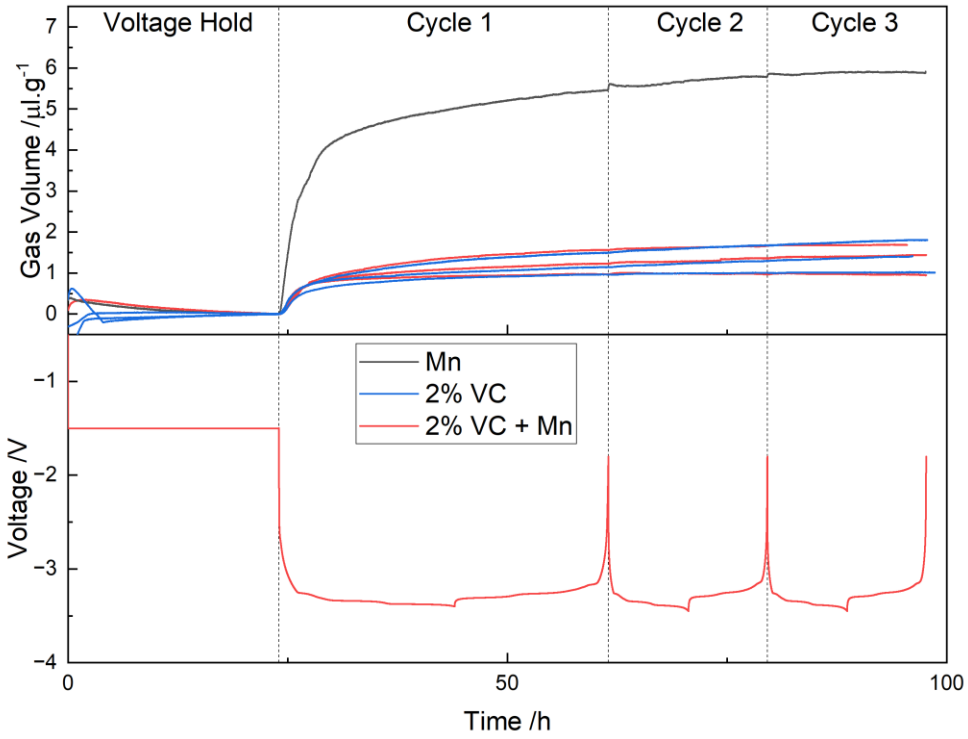

Figure 68 - Gas volumes generated in 2% VC + Mn and 2% VC doped electrolyte LFP vs graphite full cells (3 cells) with baseline Mn cell 276 and for comparison. Voltage vs time graph for 2% VC + Mn doped cell 262 below for cycling protocol reference.

Figure 68 compares the gas evolution behaviour between Mn, VC and VC+Mn cells, with the electrochemical cycling data for VC+Mn shown for reference. Firstly, when examining cycle 1 gas volumes, it is clear that the addition of VC to Mn doped cells is very effective in suppressing gas evolution, especially during the SEI formation stage. VC+Mn cells show very low gas volumes produced 1.26 ±0.29 µlg-1 of gas compared to Mn cells which produced 5.14 ±0.49 µlg-1, where without the presence of VC, the volume of gas produced is increased ~400%. When considering the theorised mechanism for increased gas evolution due to Mn dissolution (as discussed in section 1.3.3), the extra gasses generated originate from the reduction of either LEDC or EC molecules when in contact with Mn^0. From this, it seems probable that during cycling, the VC is preferentially reduced at the graphite surface, creating new products that are incorporated into the SEI layer, changing the SEI layer composition. This new composition could result in less LEDC being in contact with the Mn^0 therefore subsequently leading to less gaseous products generated. Additionally, if the Mn^0 is then surrounding by compounds that are unable to be reduced, then the Mn^0 would also be prevented from coming into contact with EC molecules within the electrolyte, further reducing the amount of gas that would otherwise be produced. This two-fold

effect of VC would explain this drastic difference in gas evolution behaviours between Mn and VC+Mn cells during cycle 1.

During cycle 2+3, the VC+Mn once again shows its effectiveness in reducing the amount of gas produced, producing 0.10 ±0.12 μlg^{-1} of gas, which is ~1 μlg^{-1} less than Mn cells. This reduction in gas volumes produced supports the theory described above, where the Mn^0 is being prevented from reacting with LEDC and EC after the SEI formation.

Another interesting observation can be seen when examining the small jumps previously seen in the chapter 3, where all transition metal cells exhibited small pressure jumps at the start of the charging step in each cycle, which was thought to be again due to the reduction of LEDC or EC when in contact with reduced Ni/Mn/Co. However here, the co-addition of VC seems to have eliminated this feature completely from the pressure measurement data, supporting the theory that the SEI formed with VC is able to surround the transition metal and prevent the reduction of LEDC and EC.

These gas evolution behaviours match well with literature as the reduction of VC at the graphite surface leads to poly(VC) compounds and Li_2CO_3 as the main solid reaction products [133]. As the VC preferentially reacts prior to EC, it means that it is more likely that the Mn is surrounded by VC reduction products rather than LEDC (EC reduction product).

Finally, comparing VC+Mn cells to VC cells, the differences between the gas volumes is negligible in all cycles, indicating very similar gassing reactions between the cells. This identical gas evolution behaviour suggests that the presence of VC in the electrolyte is enough to completely and totally prevent the increased gas evolution caused by Mn.

Examining Figure 69, we can see the voltage vs capacity graph for a VC+Mn cell, where it is clear that the presence of Mn ions in the cell system has caused the electrochemical profile to deviate from the baseline profile. Cycle 1 discharge profile clearly shows a significant reduction in capacity.

From Table 12, we compare the first cycle discharge capacity of VC+Mn cells to Mn cells, with VC+Mn achieving 330.0 ± 3.1 $mAhg^{-1}$ in cycle 1, 334.0 ±3.6 $mAhg^{-1}$ in cycle 2 and 334.4 ±4.0 $mAhg^{-1}$ in cycle 3, compared to Mn with 329.4 ±6.5 $mAhg^{-1}$, 331.0 ±5.1 $mAhg^{-1}$, 330.9 ±5.1 $mAhg^{-1}$ respectively. From this, we can see that the differences between the VC+Mn cells and Mn cells are very small, with differences in each cycle being <5 $mAhg^{-1}$. This electrochemical performance from VC+Mn cells does not match the beneficial gas evolution properties, as the addition of VC clearly is unable to suppress the negative impact of Mn ions on the discharge capacity. Another possible cause for this loss of cycle 1 discharge capacity may be due to the reduction of Mn^{2+} to Mn^0,

whilst the oxidation back to Mn^{2+} may be prevented by the addition of VC, it seems reasonable to assume that the Mn^{2+} is still in contact with the graphite surface, which means the VC is unable to prevent the Mn^{2+} from being reduced and consuming charge which could subsequently lead to unwanted side reaction, further consuming charge.

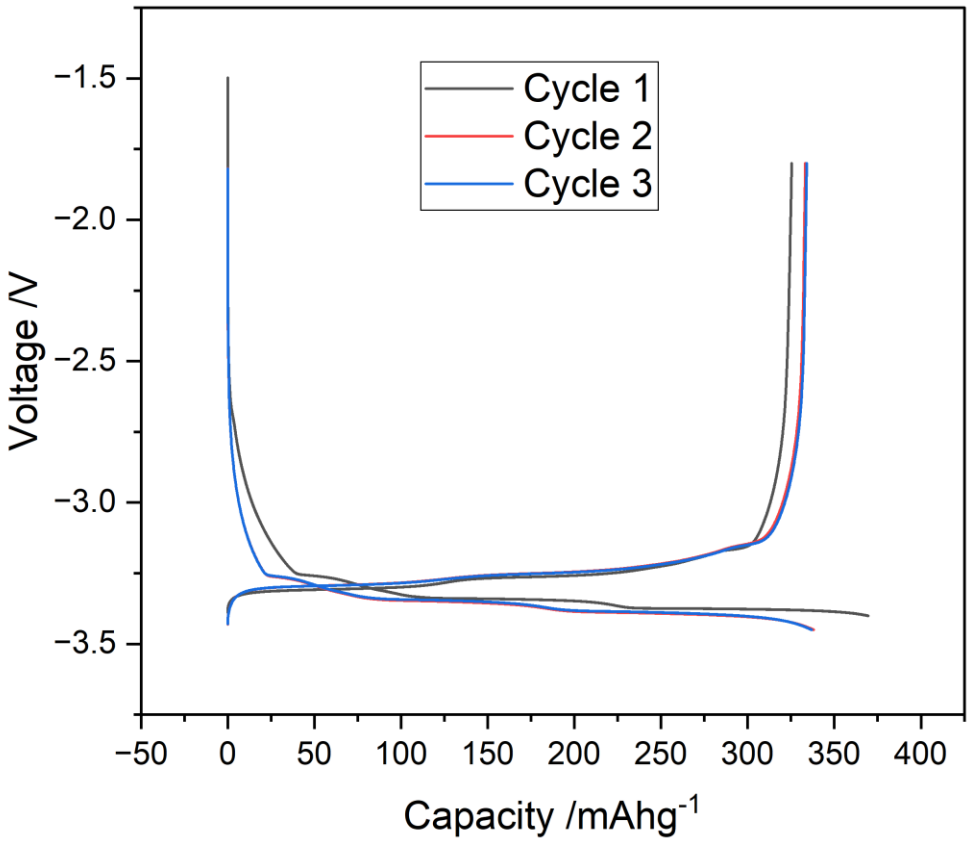

Figure 69 - Voltage vs capacity graph for a 2% VC + Mn doped electrolyte LFP vs graphite full cell (cell 262).

	Discharge Capacity /mAhg^{-1}			Coulombic Efficiency /%		
Electrolyte	Cycle 1	Cycle 2	Cycle 3	Cycle 1	Cycle 2	Cycle 3
Mn	329.4 ± 6.5	331.0 ± 5.1	330.9 ± 5.1	87.8 ± 0.4	97.6 ± 0.5	98.4 ± 0.1
2% VC	344.5 ± 2.8	333.2 ± 2.3	331.2 ± 1.0	94.7 ± 0.2	98.5 ± 1.8	98.5 ± 0.5
2% VC + Mn	330.0 ± 3.1	334.0 ± 3.8	334.4 ± 4.0	88.6 ± 0.5	98.7 ± 0.1	99.3 ± 0.1

Table 12 - Discharge capacity and Coulombic efficiency values per cycle for 2% VC + Mn doped electrolyte LFP vs graphite cell, with Mn and 2% VC doped cells values for comparison. Errors calculated from the standard deviation of 3 repeats.

In cycle 2+3 of Table 12, the discharge capacities VC+Mn and VC are very similar. VC+Mn cells 334.0 ± 3.8 $mAhg^{-1}$and 334.4 ± 4.0 $mAhg^{-1}$, and VC cells achieving 333.2 ± 2.3 $mAhg^{-1}$ and 331.2 ± 1.0 $mAhg^{-1}$. The difference between these cells is <3 $mAhg^{-1}$. VC+Mn and VC cells having similar discharge capacities aligns well with our hypothesis, as once the VC+Mn cell forms a stable SEI layer and reduces the Mn^{2+} to Mn^{0}, no further side reactions are expected to occur as the Mn^{0} cannot be oxidised back to Mn^{2+}. Assuming all the Mn^{2+} on the surface of the graphite is reduced in cycle 1, we would expect the continuation of the ordinary lithium intercalation/extraction mechanism that would occur in VC cells.

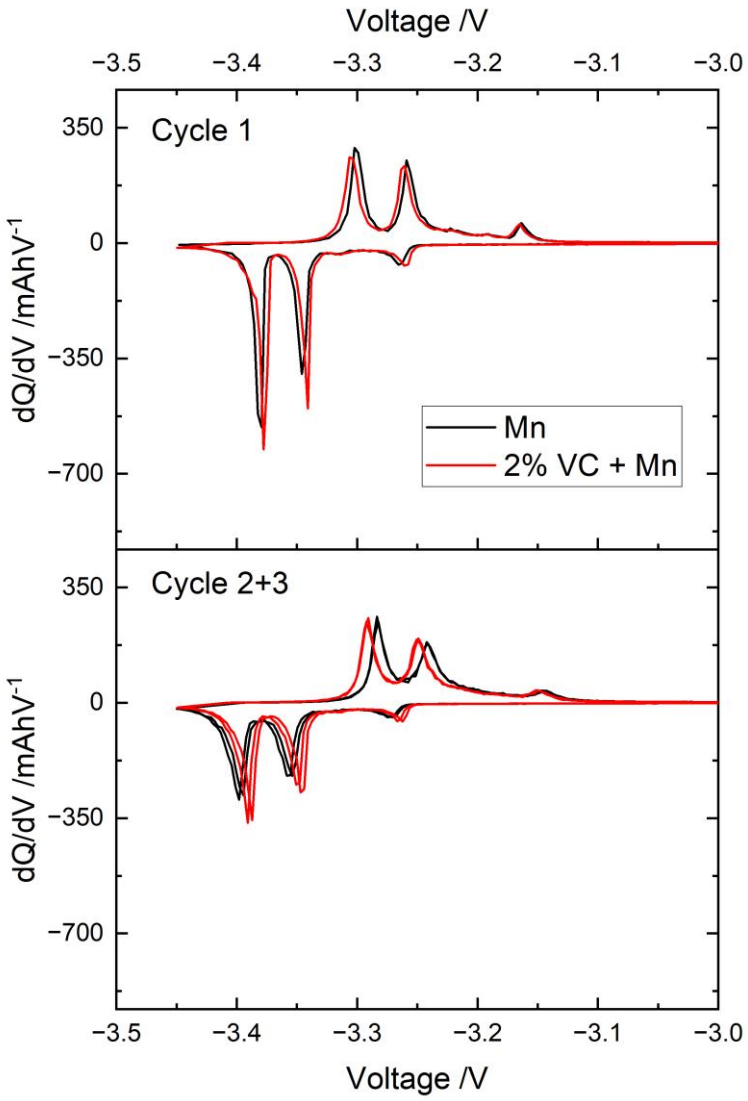

Figure 70 - dQ/dV vs voltage graph for 2% VC + Mn doped LP57 electrolyte LFP vs graphite full cell (Cell 262) compared with baseline LP57 cell 211.

Interestingly, the Mn cell also has similar cycle 2+3 discharge capacity values to the VC+Mn and VC cells, with Mn cells achieving 331.0 ± 5.1 $mAhg^{-1}$ and 330.9 ± 5.1 $mAhg^{-1}$, therefore <5 $mAhg^{-1}$ difference. This suggests that the main impact of Mn dissolution is within cycle 1 and that

over time a relatively stable SEI can still be formed, allowing the ordinary lithium intercalation/extraction to once again occur.

Table 12 shows the coulombic efficiencies in each cycle for the cells. The coulombic efficiency data mirrors the trends seen in the discharge capacities, where in cycle 1, Mn has 87.8 ± 0.4% and VC+Mn has 88.6 ± 0.5% both of which are lower than 2% VC cells which have 94.7 ± 0.2%. This decrease of ~7% coulombic efficiency in cycle 1 compared to VC cells without Mn indicates the presence of a side reaction which is most likely caused by the presence of Mn ions on the graphite surface. Furthermore, for Mn and VC+Mn cells, the efficiencies in cycle 2+3 return to approximately the same values achieved by VC cells, Mn with 97.6 ± 0.5% and 98.4 ± 0.1%, VC+Mn with 98.7 ± 0.1% and 99.3 ± 0.1%, compared to VC with 98.5 ± 1.8% and 98.5 ± 0.5% highlighting again that the biggest impact of Mn dissolution occurs mainly in cycle 1 when Mn ions are present on pristine graphite surface. High values of coulombic efficiency in cycles 2+3 for all cells indicate that the lithium intercalation/extraction is operating as normal with no significant disturbances.

The dQ/dV analysis for a VC+Mn cell can be seen in Figure 70, where the VC+Mn cells show a reduction in peak shift when compared to Mn cells, indicating that the presence of VC in the Mn doped electrolyte allows the formation of an SEI with decreased resistance compared to Mn without VC additive. The similar peak heights corroborate with the discharge capacity values, where there are negligible differences in peak heights between VC+Mn and Mn cells.

5.3 Gas Evolution Behaviour with the Introduction of LFO Additive with the Co-Addition of Manganese Ions

Figure 71 shows the comparison of gas evolution behaviour for Mn, LFO, and LFO+Mn cells, with LFO+Mn electrochemical cycling data below for reference. From this, LFO+Mn cells show that the LFO additive is successful in reducing the amount of gas generated during the SEI formation reaction in cycle 1, as shown by the smaller initial sharp increase in pressure and the lower total cycle 1 gas volume produced, LFO+Mn produced 2.44 ±0.29 μlg^{-1} compared to Mn producing 5.14 ±0.39 μlg^{-1}. This correlates well with expectations; the introduction of LFO into the electrolyte would result in the SEI composition having an increased amount of $Li_xPO_yF_z$ (from the reduction of LFO at the graphite surface)[106, 107], which would lead to less LEDC and EC coming in contact with Mn^0 due to the additional $Li_xPO_yF_z$ surrounding the transition metal, thus resulting in fewer gaseous products.

When inspecting cycle 2+3 in Figure 71, we see that the amount of gas produced in are LFO+Mn is quite comparable with Mn cells, where Mn cells only having marginally increased gas volumes. Mn cells produced 0.62 ±0.18 $\mu l g^{-1}$ in cycle 2+3, and LFO+Mn produced 0.64 ±0.24 $\mu l g^{-1}$. From this, it can be inferred that the SEI layer formed with LFO only provides a small improvement to its passivating ability, as similar amounts of EC are able to still be reduced during the later cycles to give gaseous products.

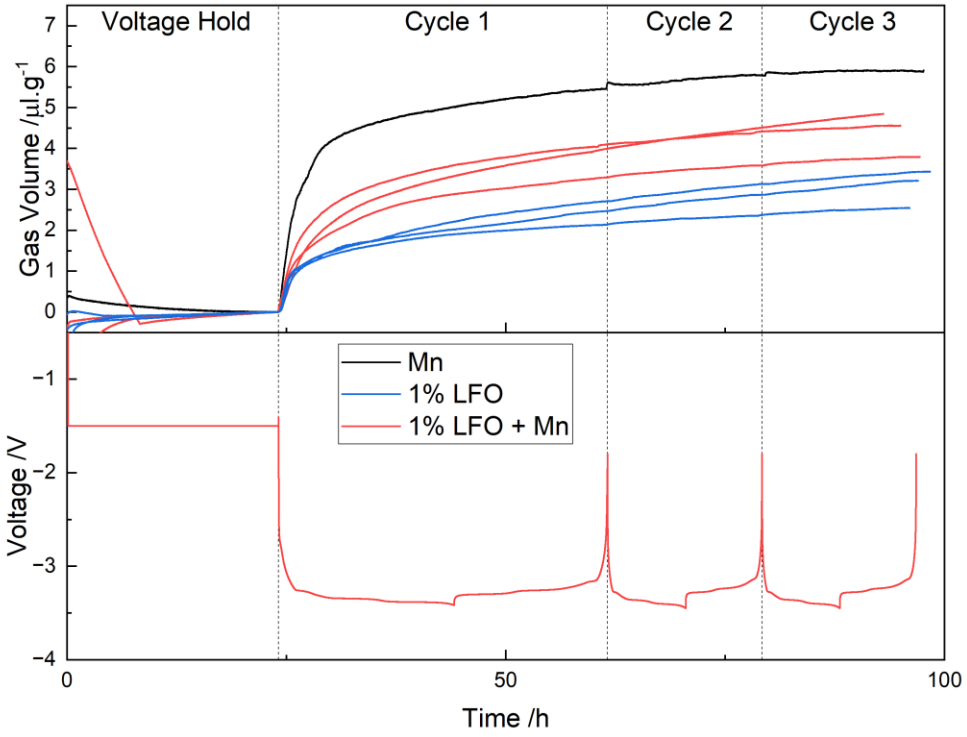

Figure 71 - Gas volumes generated in 1% LFO + Mn and 1% LFO doped electrolyte LFP vs graphite full cells (3 cells) with baseline Mn cell 276 for comparison. Voltage vs time graph for 2% VC + Mn doped cell 321 below for cycling protocol reference.

Again in Figure 71, when comparing Mn cells to LFO+Mn cells, presence of LFO seems to remove the small pressure jumps that are otherwise observed in Mn cells. This once again supports the hypothesis that if the Mn^0 is surrounded by stable compounds that are resistant to reduction, further EC/LEDC reduction cannot occur thus eliminating the gas evolution reactions that cause the pressure jumps at the start of the charging.

Further examining the gas evolution behaviour between LFO and LFO+Mn in Figure 71 highlights LFO's inability to completely prevent the impact of Mn dissolution, where in cycle 1, LFO+Mn exhibits a greater gas volume evolved. LFO+Mn produced 3.76 ±0.40 $\mu l g^{-1}$ and LFO only produced 2.44 ±0.29 $\mu l g^{-1}$. Whilst the increased $Li_xPO_yF_z$ content in the SEI layer is able to reduce the amount gas evolved, clearly some additional reductions of EC/LEDC still occur. The cycle 2+3 data for both cells remain very similar, with LFO+Mn producing 0.64 ±0.24 $\mu l g^{-1}$ and LFO

producing 0.62 ±0.18 μlg^{-1}, indicating that the passivating ability of the SEI, once fully formed, is not affected by the presence of Mn which is in line with expectations.

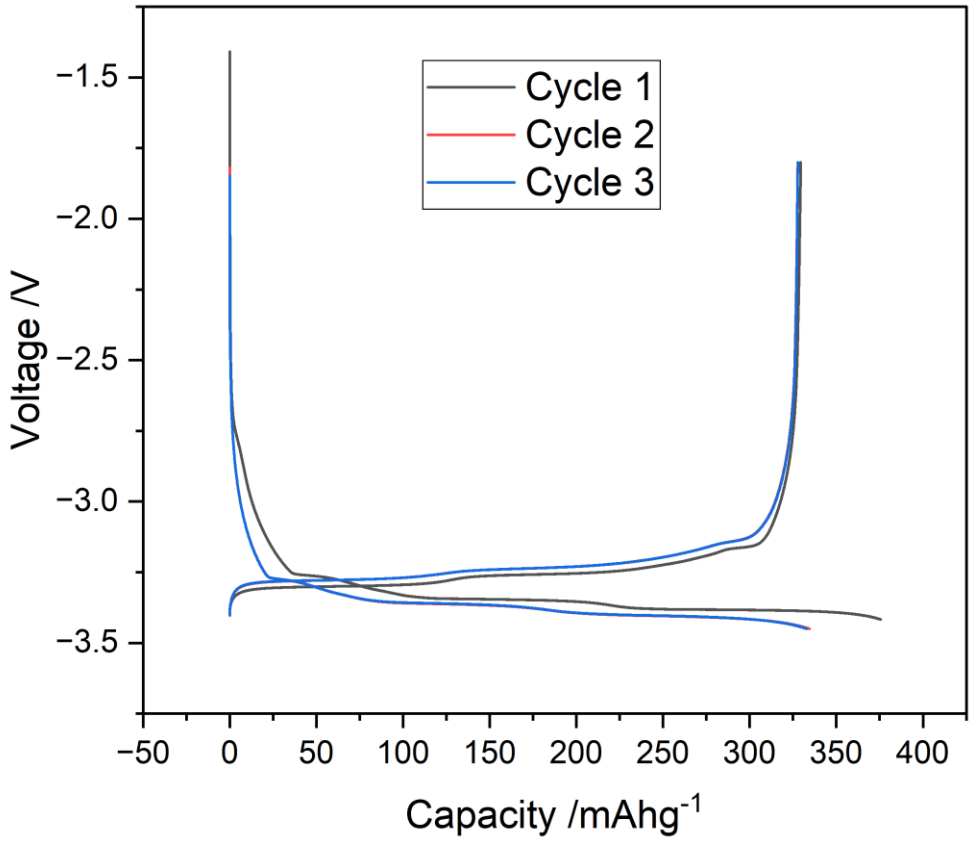

Figure 72 - Voltage vs capacity graph for a 1% LFO + Mn doped electrolyte LFP vs graphite full cell (cell 321).

	Discharge Capacity /$mAhg^{-1}$			Coulombic Efficiency /%		
Electrolyte	Cycle 1	Cycle 2	Cycle 3	Cycle 1	Cycle 2	Cycle 3
Mn	329.4 ± 6.5	331.0 ± 5.1	330.9 ± 5.1	87.8 ± 0.4	97.6 ± 0.5	98.4 ± 0.1
1% LFO	344.7 ± 3.5	333.6 ± 2.9	333.3 ± 3.0	94.0 ± 0.6	99.0 ± 0.2	99.2 ± 0.2
1% LFO + Mn	329.2 ± 2.7	331.2 ± 4.5	331.6 ± 4.7	87.9 ± 0.6	98.0 ± 0.1	98.6 ± 0.1

Table 13 - Discharge capacity and Coulombic efficiency values per cycle for 1% LFO + Mn doped electrolyte LFP vs graphite cell, with the Mn and 1% LFO cells values for comparison. Errors calculated from the standard deviation of 3 repeats.

Figure 72 shows the voltage vs capacity graph for an LFO+Mn cell, where the presence of Mn clearly has an effect on the electrochemistry of the cell. Despite the addition of the LFO additive, the cycle 1 discharge profile shows that the cell achieved lower discharge capacities.

From Table 13, we first compare the cycle 1 data between Mn and LFO+Mn cells. Mn has 329.4 ±6.5 $mAhg^{-1}$ and LFO+Mn has 329.2 ±2.7 $mAhg^{-1}$. These values are very similar between the cells, which reinforces the hypothesis that the presence of Mn ions at the graphite surface during cycle 1 leads to increased side reactions, thus causing a decreased discharge capacity. As Mn is not present in LFO cells, it is able to achieve much higher discharge capacities, LFO cells achieve 344.7 ±3.5 $mAhg^{-1}$ (~15 $mAhg^{-1}$ more than when Mn is present).

Discharge capacities in cycle 2+3 of Table 13 are very comparable between all three electrolyte systems, with Mn obtaining 331.0 ±5.1 $mAhg^{-1}$ and 330.9 ±5.0 $mAhg^{-1}$ for cycles 2+3 respectively, LFO with 333.6 ±2.9 $mAhg^{-1}$ and 333.3 ±3.0 $mAhg^{-1}$, and LFO+Mn with 331.2 ±4.5 $mAhg^{-1}$ and 331.6 ±4.7 $mAhg^{-1}$. This similarity in discharge capacities between the cells (<4$mAhg^{-1}$) matches well with the gas evolution data, with the trends seen in gas evolution during cycles 2+3 matching with the discharge capacities. This supports the theory that once a stable SEI is formed, the impact of Mn dissolution is reduced considerably, both electrochemically and in gas evolution.

Similarly, the coulombic efficiency data in Table 13 also mirror the discharge capacity trends, where cells Mn and LFO+Mn cells have comparable efficiencies in cycle 1 of 87.8 ±0.4% and 87.9 ±0.6% respectively, both of which are significantly lower than that in LFO cells which achieved 94.0 ±0.6 $mAhg^{-1}$. This decreased coulombic efficiency is expected due to the reduction of Mn^{2+} at the graphite surface. The electrons consumed during the reduction of Mn^{2+} would cause the charge capacity to increase, whilst the additional side reactions with Mn would lead to decreased discharge capacity. Coulombic efficiency data for cycle 2+3 see the values for all cells returning to above 96%. Mn with 97.6 ± 0.5% and 98.4 ± 0.1%, LFO with 99.0 ± 0.2% and 99.2 ± 0.2%, LFO+Mn with 98.0 ± 0.1% and 98.6 ± 0.1%.

The dQ/dV analysis shown in Figure 73, shows that the addition of LFO to Mn cells causes a very small degree of peak shift which is more prevalent in cycles 2+3, indicating that the SEI formed with LFO+Mn has increased resistance in comparison to the SEI formed with just Mn. The peak heights between LFO+Mn and Mn cells are relatively similar which matches the discharge capacity trends.

Clearly, there is a disconnect between the trends seen in the electrochemical data and the gas evolution data in cycle 1, where LFO is successful in reducing further gas evolution caused by the dissolution of Mn but is unable to prevent the detrimental effects on the discharge capacity

and coulombic efficiency. However, in cycle 2+3, the electrochemical and gas evolution data match well, where the impact of the Mn dissolution seems to be unaffected by the LFO additive.

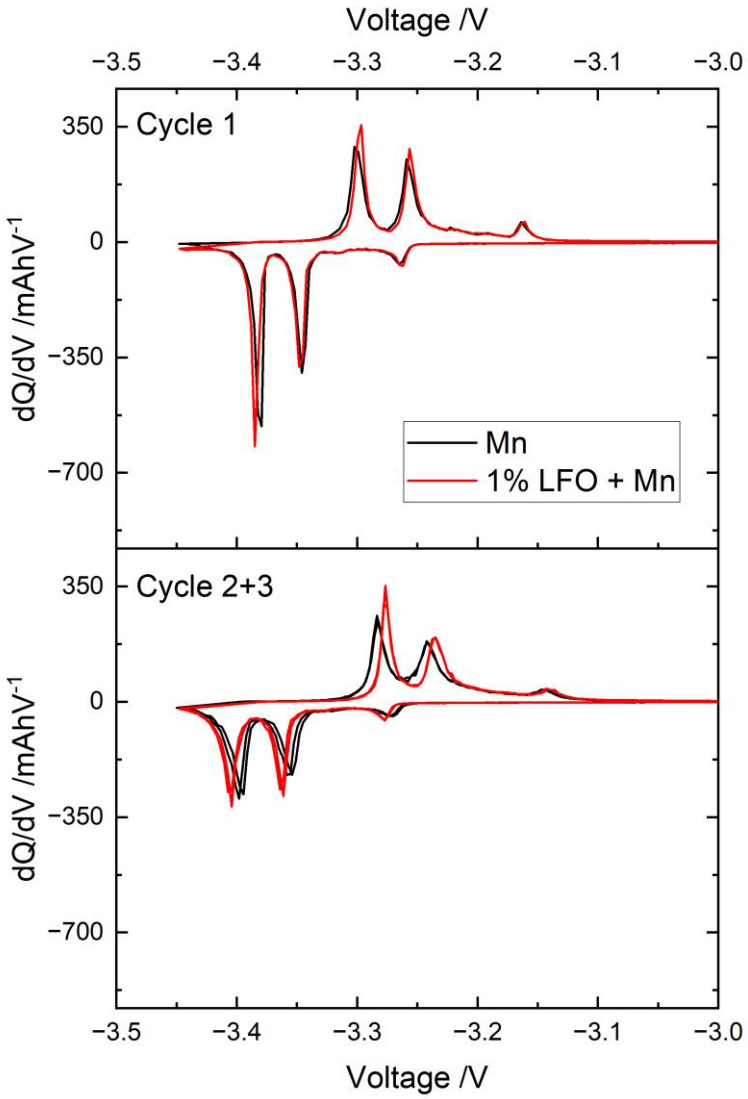

Figure 73 - dQ/dV vs voltage graph for 1% LFO + Mn doped LP57 electrolyte LFP vs graphite full cell (Cell 321) compared with baseline Mn cell 276.

5.4 Gas Evolution Behaviour with the Introduction of DTD + VC Additives with the Co-Addition of Manganese Ions

Firstly, it should be noted that experiments with the introduction of DTD additives with the co-addition of manganese ions were not conducted due to time constraints within the project. The decision was made to instead only investigate the DTD+VC additive combination as this exhibited more promising performance than just DTD.

Figure 74 compares the gas evolution data for Mn and DTD+VC+Mn cells. The gas evolution behaviour of DTD+VC+Mn shows that the incorporation of the additive blend is able to reduce the

amount gas evolution that occurs during cycle 1 in comparison to Mn cells, where DTD+VC+Mn cells produce 3.26 ±0.34 µlg^{-1} amount of gas compared Mn cells which produced 5.14 ±0.39 µlg^{-1} amount of gas. Clearly the reduction products of DTD+VC contribute to the formation of a stable SEI that suppresses the Mn ability to reduce LEDC/EC thus reducing the amount of gas produced.

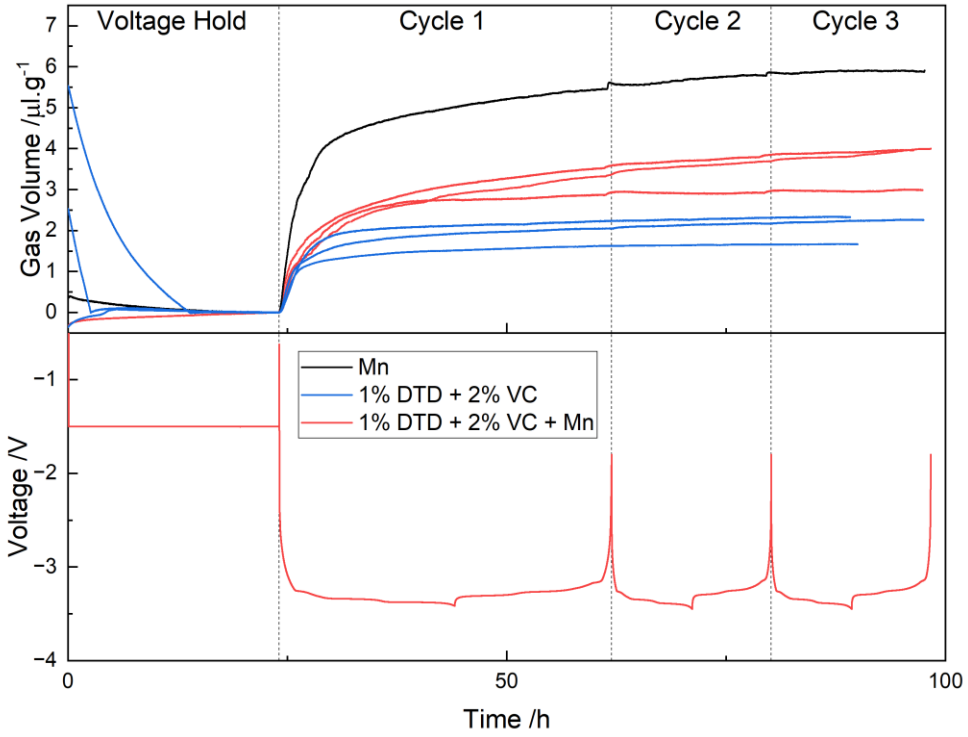

Figure 74 - Gas volumes generated in 1% DTD + 2% VC + Mn doped electrolyte LFP vs graphite full cells (3 cells) with baseline Mn cell 276 for comparison. Voltage vs time graph for 2% VC + Mn doped cell 304 below for cycling protocol reference.

Furthermore, when examining the cycle 2+3 data, we again see a reduced amount of gas evolution with the addition of DTD+VC, with DTD+VC+Mn cells produce 0.39 ±0.26 µlg^{-1} of gas and Mn cells produce 1.14 ±0.64 µlg^{-1} amount of gas. Indicating that the SEI formed with DTD+VC has properties that are able to suppress additional gassing reactions occurring in later cycles.

The gas evolution behaviour for DTD+VC+Mn correlated well with expectations as VC+Mn cells had already shown VC's ability to have a substantial impact on reducing gas evolution, therefore it was simply the case of how much gas is produced from the addition of DTD. Further discussion comparing DTD+VC+Mn to VC+Mn cells will be covered in the next section.

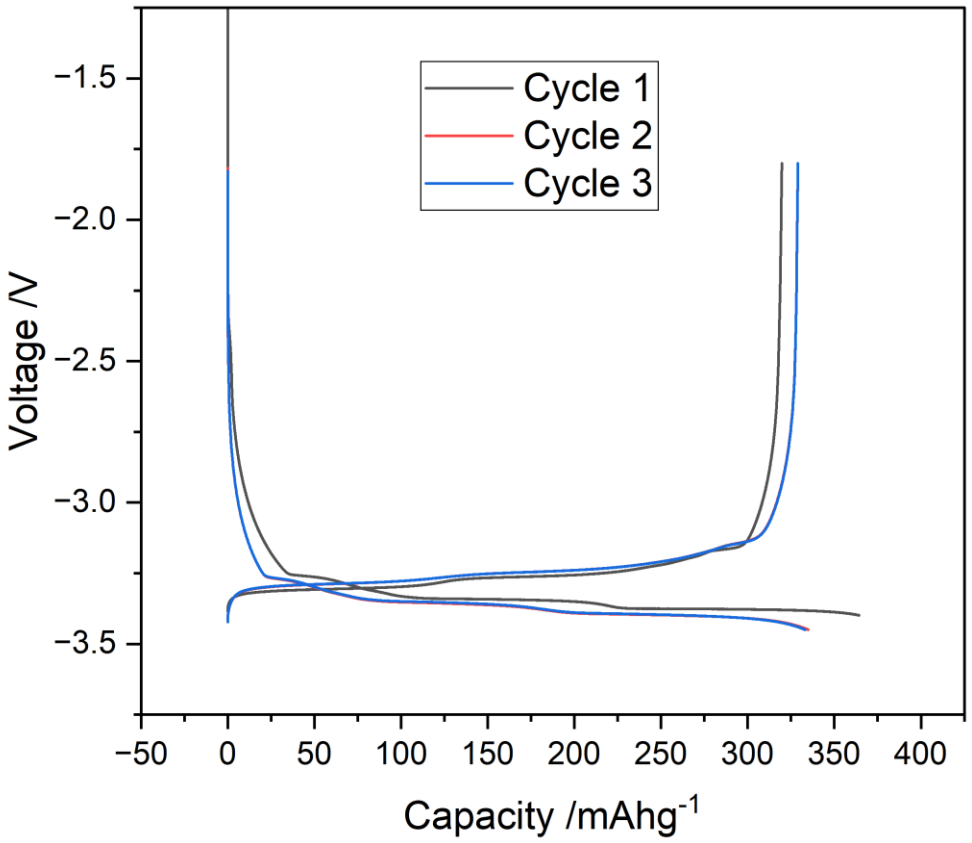

Figure 75 - Voltage vs capacity graph for a 1% DTD + 2% VC doped electrolyte LFP vs graphite full cell (cell 304).

	Discharge Capacity /mAhg^{-1}			Coulombic Efficiency /%		
Electrolyte	Cycle 1	Cycle 2	Cycle 3	Cycle 1	Cycle 2	Cycle 3
Mn	329.4 ± 6.5	331.0 ± 5.1	330.9 ± 5.1	87.8 ± 0.4	97.6 ± 0.5	98.4 ± 0.1
1% DTD + 2% VC	340.7 ± 4.6	328.1 ± 7.7	327.6 ± 8.1	93.5 ± 1.3	99.0 ± 0.4	99.2 ± 0.4
1% DTD + 2% VC + Mn	320.2 ± 5.2	324.9 ± 4.3	325.3 ± 4.3	89.7 ± 0.4	98.4 ± 0.3	98.9 ± 0.3

Table 14 - Discharge capacity and Coulombic efficiency values per cycle for 1% DTD + 2% VC + Mn doped electrolyte LFP vs graphite cell, with the Mn and 1% DTD + 2% VC cells values for comparison. Errors calculated from the standard deviation of 3 repeats.

When investigating the impact of the co-addition of Mn to the additive blend, it is important to cross examine with cells without the presence of Mn. Figure 74 show that the DTD+VC blend was unable to fully prevent the impact of Mn as it was unable to obtain gas

evolution behaviours similar to that of solely DTD+VC. In the DTD+VC cells in cycle 1, 1.94± 0.29 μlg^{-1} of gas was produced, which is ~1.32 μlg^{-1} less than DTD+VC+Mn cells. Additionally, the gas volumes produced in cycles 2+3 were lower in when Mn was not present, DTD+VC cells produced 0.15 ±0.08 μlg^{-1} of gas. This suggesting that the SEI layer formed with Mn is less robust than the SEI layer formed without Mn. From literature, it is thought that the reduction products of the DTD can undergo a wide variety of further reactions [134], therefore it may be possible that there DTD reduction products may also be able to react with the Mn^0, thus increasing the gas evolution in cycles 2+3.

Figure 75 shows the voltage vs capacity graph for DTD+VC+Mn cells, where we see the impact of Mn ions on the electrochemical profile. Clearly, the addition of DTD+VC additives was not enough to counteract the detrimental effect of Mn ions on the discharge capacity.

Table 14 allows the comparison of discharge capacities for the different electrolytes. From this table, we see that the DTD+VC+Mn cell actually achieves a slightly lower average cycle 1 discharge capacity in comparison to Mn cells, with DTD+VC+Mn cells at 320.2 ±5.2 $mAhg^{-1}$ and Mn cells at 329.4 ±6.5 $mAhg^{-1}$. This is unexpected as the discharge capacity is thought to be limited by the side reaction of Mn^{2+} reduction, therefore both cells should achieve similar discharge capacities as they are limited by the same reaction. However, when considering the experiments conducted in chapter 4, we observed that the addition of DTD to the baseline electrolyte also lowered the first cycle discharge capacity, so perhaps the same case here, where the reduction of DTD causes additional loss of discharge capacity, independent to the impact of Mn ions.

The discharge capacities for cycle 2+3, shown in Table 14, reiterate the hypothesis that the Mn is significantly more impactful in cycle 1 rather than later cycles. DTD+VC+Mn cells achieve capacities of 324.9 ±4.3 $mAhg^{-1}$ and 325.3 ±4.3 $mAhg^{-1}$ for cycles 2+3 respectively, whilst Mn cells achieved comparable values of 331.0 ±5.1 $mAhg^{-1}$ and 330.9 ±5.1 $mAhg^{-1}$. Both of these values are very comparable to DTD+VC cells which achieved 328.1 ±7.7 μlg^{-1} and 327.6 ±8.1 μlg^{-1}, indicating the standard operation of the lithium insertion/extraction reaction for all cells.

The coulombic efficiency data is presented in Table 14, showing a deviation from the trend observed in the discharge capacity behaviour, where the coulombic efficiency for the DTD+VC+Mn cell is slightly higher than the Mn cell. DTD+VC+Mn obtaining 89.7 ±0.4% and Mn obtaining 87.8 ±0.4%. This small increase in coulombic efficiency indicates that the difference between the discharge capacity and the charge capacity is smaller. If we assume that all of the discharge capacity is due to the lithium extraction, the difference between the discharge capacity and the charge capacity represents the unwanted side reactions that incur additional recorded capacity. Therefore, the increased coulombic efficiency in conjunction with the decreased

discharge capacity indicates that the decreased lithium extraction is not due to unwanted side reactions occurring on the graphite surface. The exact reason for this is unclear, however a possible explanation could be that the use of DTD+VC combination depletes the available lithium within the cell, therefore less lithium is able to be intercalated into the graphite structure, thus explaining the decreased side reactions since no additional reactions are occurring. We also know that the reduction of DTD leads to products that can undergo further reactions in the SEI and at the graphite surface [134], therefore it may be possible that these further reactions are responsible for the small disparity in coulombic efficiency.

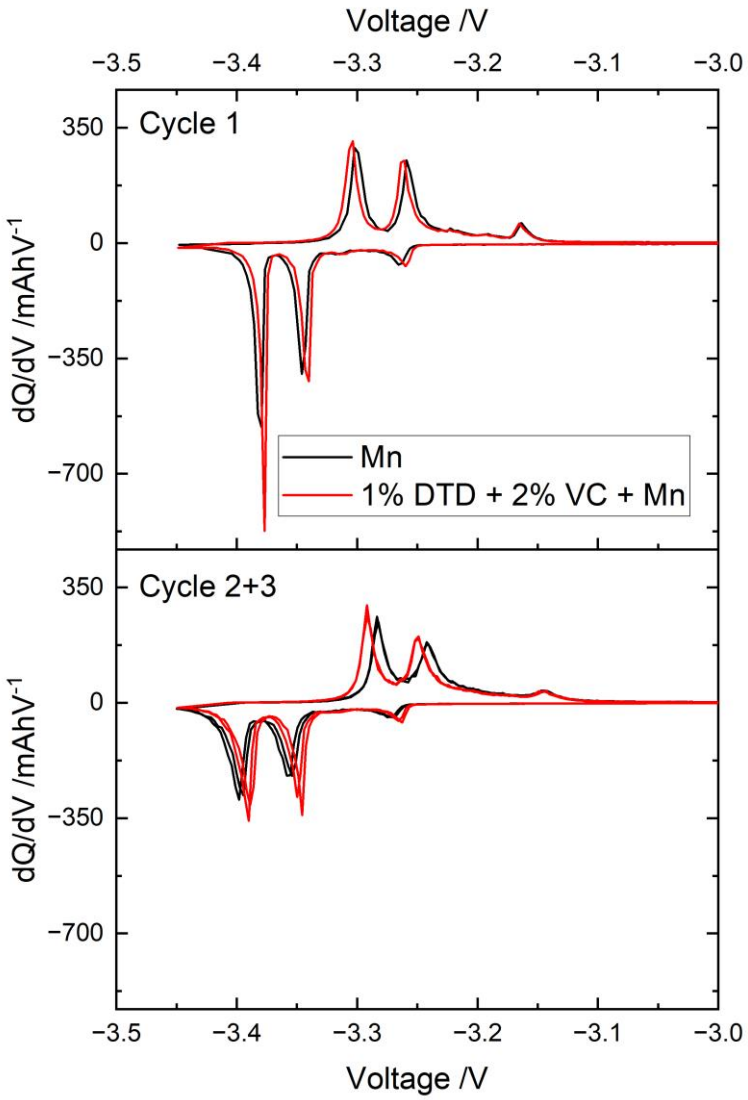

Figure 76 - dQ/dV vs voltage graph for 1% DTD + 2% VC doped LP57 electrolyte LFP vs graphite full cell (Cell 304) compared with baseline LP57 cell 211.

The coulombic efficiency in cycle 2+3 of Table 14 match expectations very well, with all three electrolytes returning to >97%. Mn with 97.6 ± 0.5% and 98.4 ± 0.1%, DTD+VC with 99.0 ± 0.4% and 99.2 ± 0.4%, DTD+VC+Mn with 98.4 ± 0.3% and 98.9 ± 0.3%. This again supports our hypothesis that Mn dissolution is more impactful in early stages of cycling when the Mn ion is

present on pristine graphite surface, and that once the SEI is formed, the degree of side reactions caused by Mn is significantly reduced.

dQ/dV analysis of DTD+VC+Mn cells can be seen in Figure 76, where the addition of DTD+VC additive blend to Mn doped electrolyte has shown to decrease peak separation in cycle 1 and to a greater extent in cycle 2+3. This implies that the addition of the DTD+VC additive blend is able to decrease the resistance of the SEI layer.

The electrochemistry does match well with the gas evolution data, especially with regards to the impact of Mn dissolution not being completely negated by the introduction of the DTD+VC combination. This is shown in cycle 1 through increased gas evolution and also in the decreased electrochemical performance of DTD+VC+Mn cells when compared to DTD+VC cells. Furthermore, the differences in discharge capacity, coulombic efficiency and gas evolution in cycles 2+3 are all relatively small in comparison to cycle 1, which highlights how a stable SEI prevents any considerable changes in electrochemical or gas evolution behaviour.

5.5 Comparison of Gas Evolution Behaviour of the Electrolyte Additives with the Co-Addition of Manganese Ions

Figure 77 compares the gas evolution data for all of the electrolyte additives with the co-addition of Mn ions. Firstly, comparing VC+Mn cells to DTD+VC+Mn cells reveals that the addition of DTD, similar to the results presented in chapter 4, is actually detrimental to the gas evolution during cycle 1. VC+Mn cells produced 1.26 ±0.29 μlg^{-1} and DTD+VC+Mn produced 3.26 ±0.34 μlg^{-1}. VC cells exhibited lower gas volumes, thus indicating that combining VC with DTD is actually disadvantageous, as VC alone is much more effective. This is in part due to the DTD reduction pathway generating gasses through the further reaction of the DTD reduction products [134]. As the reduction of DTD and the presence of Mn ions both cause gas evolution, it is difficult to definitely determine to what extent each factor contributes to the increased gas evolution. Looking at the difference in cycle 1 gas evolution between VC and DTD+VC cells in Chapter 3, we see that DTD+VC cells have ~0.77 μlg^{-1} more than VC cells. If we attribute this solely to the gas evolution caused by DTD reduction, we expect similar difference between VC+Mn and DTD+VC+Mn. However, the difference between VC+Mn and DTD+VC+Mn is ~2.00 μlg^{-1} which is significantly greater than cells without Mn in Chapter 3. It is likely that the interaction between Mn ions and the additives is also contributing to further gas evolution. As both the VC and DTD additives operate by introducing new compounds into the SEI layer by reduction at the graphite surface, it stands to reason that the VC products seemingly allow the formation of an improved SEI layer and that the introduction of DTD products can almost be seen as a contaminate, interfering with the

operation of the VC SEI layer. Clearly, an SEI layer formed with only the addition of VC is significantly better than an SEI with the addition of DTD, allowing drastic reduction gas evolution during cycle 1.

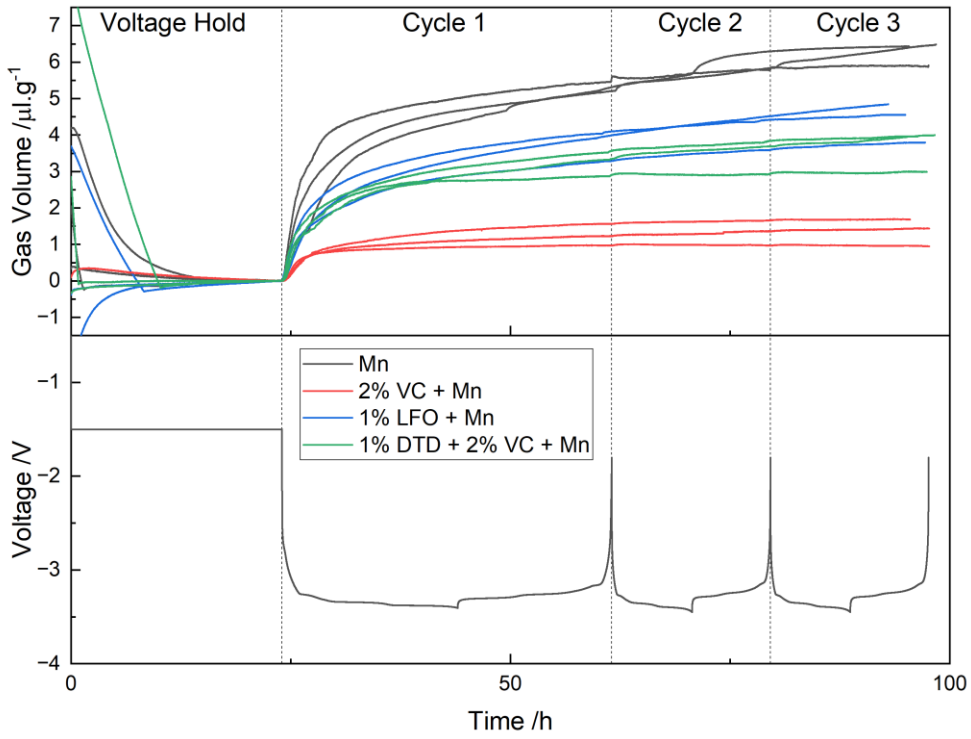

Figure 77 - Comparison of gas volumes generated in additive + Mn doped electrolyte LFP vs graphite full cells with baseline LP57 cells. Voltage vs time graph for baseline LP57 cell 211 below for cycling protocol reference.

When assessing the cycle 1 gas evolution behaviour for LFO+Mn cells, we see that it generates the largest volume of gas out of the three electrolyte additives. LFO+Mn cells produced 3.76 ±0.40 µlg^{-1} of gas, which is over double the amount seen in VC+Mn cells and is a slight increase (~0.5 µlg^{-1}) from DTD+VC+Mn cells. This correlates quite well with the experiments seen in chapter 4, where in the absence of Mn ions, LFO cells also generated the most gas in cycle 1 out of all of the electrolyte additives. Therefore, it can be deduced that the introduction of LFO reduction products (mainly $Li_xPO_yF_z$) is not as effective as the VC or DTD+VC reduction products with regards to reducing gas evolution during the SEI formation reaction. Additionally, LFO is the only additive that was not preferentially reduced at the graphite surface prior to electrolyte components [106], therefore it stands to reason that the LFO was unable to prevent the LEDC from being formed and coming in contact with the Mn^0 on the graphite surface, thus leading to greater gas evolution during cycle 1.

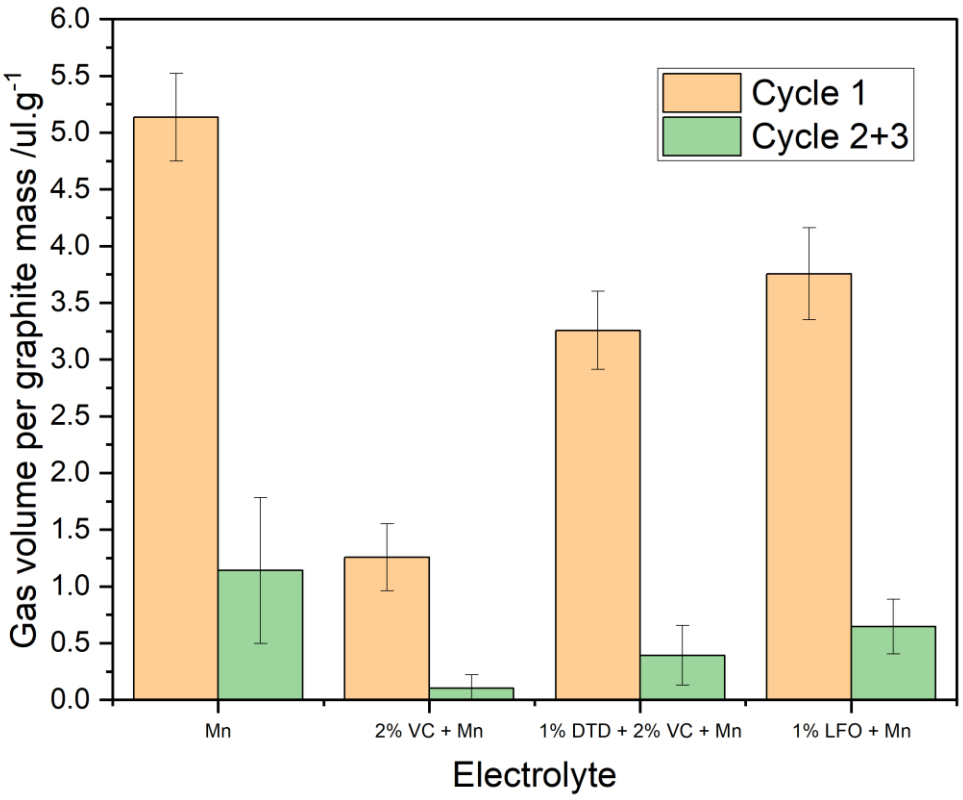

Figure 78 - Comparison of average total gas volumes during each cycle between additive + Mn doped electrolyte LFP vs graphite full cells with baseline LP57 cells. Errors calculated from standard deviation in 3 repeats per electrolyte.

Gas evolution data in cycle 2+3, as shown in Figure 77, reiterates the trends seen in the cycle 1 data. VC+Mn cells produced 0.10 ±0.12 μlg^{-1}, DTD+VC+Mn produced 0.39 ±0.26 μlg^{-1}, and LFO+Mn produces 0.64 ±0.24 μlg^{-1}, where again VC+Mn cells have substantially lower total gas volume, DTD+VC+Mn is the next best performing, with LFO having the greatest total gas volume. It should be noted that the difference in cycle 2+3 gas evolution between DTD+VC+Mn and LFO+Mn is only marginal, suggesting that the SEI formed with DTD+VC additives is only a slight improvement on the SEI formed with LFO.

Furthermore, the addition of all of the additives seems to prevent or decrease the magnitude of the pressure jumps that were previously present at the start of the charging steps of each cycle (discussed in chapter 3). This is linked to the fact that the additives help form a stable and robust SEI layer that can prevent further gassing events by inhibiting the Mn^0 from reducing LEDC/EC.

All three electrolytes have varying impacts on the gas evolution behaviour during cycling; however, it is clear that the incorporation of the additives, regardless of choice, is beneficial for the cell as they all are able to reduce the volume of gas produced during cycling.

When comparing the cycle 1 discharge capacities in Figure 79, we see that DTD+VC+Mn cells have the lowest values of 320.2 ±5.2 $mAhg^{-1}$, with VC+Mn having 330.0 ±3.1 $mAhg^{-1}$ and similarly LFO+Mn having 344.7 ±3.5 $mAhg^{-1}$. Evidently, the addition of DTD cells seems to be the cause of the reduced capacity (in comparison to solely VC), again reinforcing our theory that DTD reduction products undergo further electrochemical reactions that consumes charge and thus increases the irreversible capacity loss. When examining the VC+Mn and LFO+Mn, we see that they possess very similar cycle 1 discharge capacities, implying that the additives have similar impacts on the short-term electrochemistry of the cells.

The incorporation of additives is not expected to decrease the performance of the cell however in the case of DTD+VC+Mn cells we see that not only does it have the lowest cycle 1 discharge capacity, but it is also actually lower than that of the Mn Cell. A possible explanation is that in addition to the Mn^{2+} reduction reaction reducing the discharge capacity, there may also be an additional reaction involving the DTD, that may further reduce the discharge capacity. This explanation matches the expectation discussed in Chapter 4, where the reduction of DTD itself does not produce gas, however its products may undergo further electrochemical reactions [134].

Cycle 2+3 discharge capacities for VC+Mn cells and LFO+Mn cells were very similar. VC+Mn achieved 334.0 ± 3.8 $mAhg^{-1}$ and 334.4 ± 4.0 $mAhg^{-1}$, and LFO+Mn achieved 331.2 ± 4.5 $mAhg^{-1}$ and 331.6 ± 4.7 $mAhg^{-1}$. For VC+Mn and LFO+Mn cells, it's clear that the Mn dissolution is more impactful in early stages of cycling, especially during the SEI formation reaction, however once a stable SEI layer is formed, the lithium intercalation/extraction reaction continues as normal. The reaction products of both these additives evidently are able to prevent the Mn^0 from reducing LEDC/EC in later stages of cycling.

DTD+VC+Mn cells is also showing a slightly lower discharge capacity in cycles 2+3, achieving 324.9 ± 4.3 $mAhg^{-1}$ and 325.3 ± 4.3 $mAhg^{-1}$. However, if our theory of irreversible capacity loss due to further reactions of DTD reduction products is correct, then this lower discharge capacity in cycles 2+3 can be expected, as less lithium is available for intercalation into the graphite surface even in later stages of cycling. Our investigations in chapter 4 support this theory further, as we see the average discharge capacity in all cycles are lower when DTD is present even in the absence of Mn.

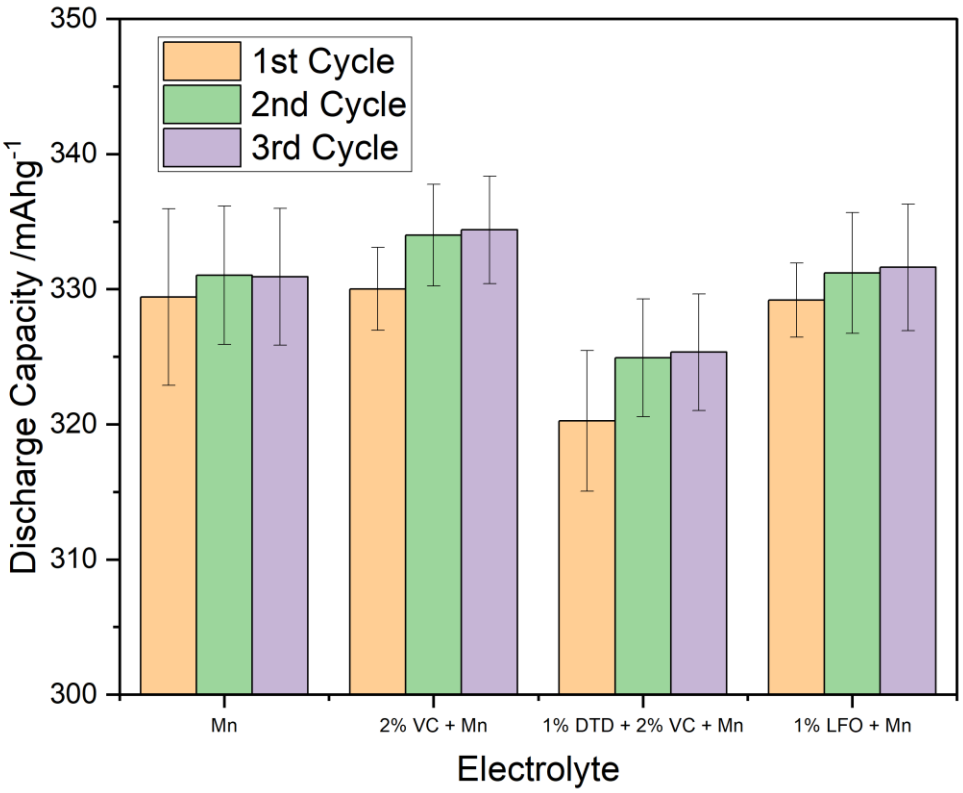

Figure 79 – Comparison of average discharge during each cycle between additive + Mn doped electrolyte LFP vs graphite full cells with baseline LP57 cells. Errors calculated from standard deviation in 3 repeats per electrolyte.

Ther coulombic efficiency for the cells, shown in Figure 80, follow a similar trend to the discharge capacity data. Where the cycle 1 coulombic efficiency for VC+Mn and LFO+Mn is very similar to one another, whilst DTD+VC+Mn cells being different, having a slightly higher cycle 1 efficiencies. VC+Mn having 88.6 ±0.5%, LFO+Mn having 87.9 ±0.6%, and DTD+VC+Mn having 89.7 ±0.4%. The behaviour seen in VC+Mn and LFO+Mn supports the hypotheses given in the discharge capacity discussions, where VC and LFO additives have differing effects on gas evolution but seemingly less so on the electrochemical performance, highlighting that the gas suppressing properties of the SEI are drastically changed with the choice of reduction products, but does not seemingly impact the conductivity properties. The increased cycle 1 efficiency for DTD+VC+Mn is interesting as this behaviour was not observed for the DTD+VC cells without Mn dissolution. In the case where Mn was not present, DTD+VC cells had comparable efficiencies with VC and LFO, possibly indicating an interaction between Mn and DTD, changing the nature of the lithium intercalation/extraction reaction.

Coulombic efficiencies in cycle 2+3 are very similar amongst all the electrolyte additives, again supporting the hypothesis that Mn is most impactful in early stages of cycling. VC+Mn achieves 98.7 ± 0.1% and 99.3 ± 0.1%, LFO+Mn achieves 98.0 ± 0.1% and 98.6 ± 0.1%, and

DTD+VC+MN achieves 98.4 ± 0.3% and 98.9 ± 0.3%. The different SEI compositions are all able to suppress further unwanted side reactions that occur during later stages of the cycling, thus giving the high coulombic efficiencies in cycle 2+3.

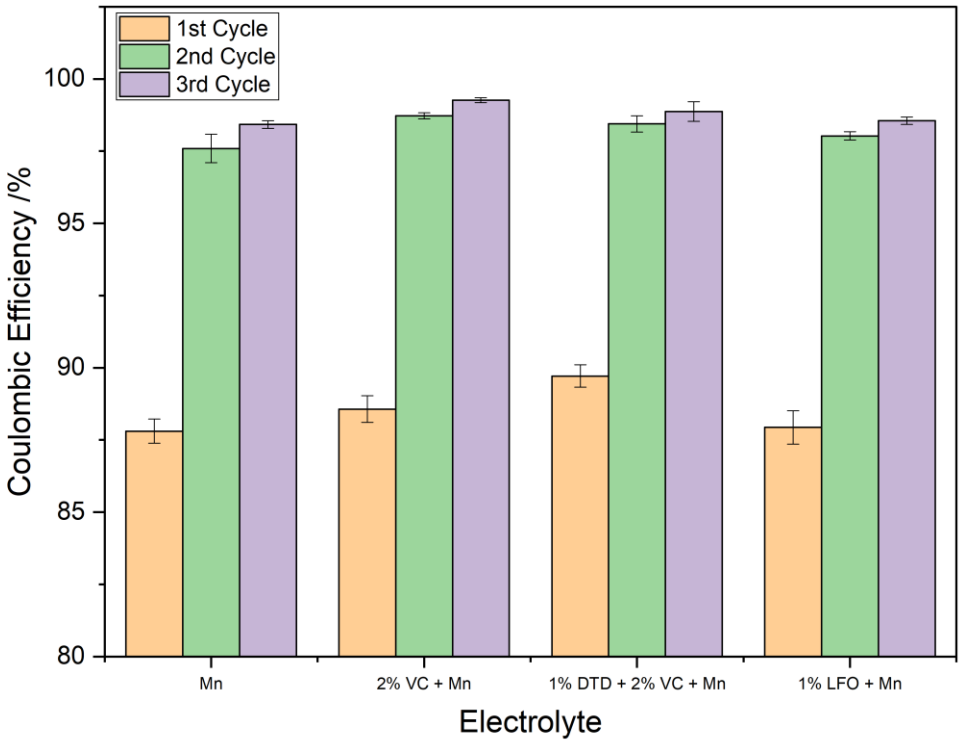

Figure 80 - Comparison of average coulombic efficiency during each cycle between additive + Mn doped electrolyte LFP vs graphite full cells with baseline LP57 cells. Errors calculated from standard deviation in 3 repeats per electrolyte.

When considering all the electrochemical data together, it is clear that all the electrolyte additive choices were unable to prevent the detrimental effects of Mn dissolution, namely the impacts on the cycle 1 discharge capacity and coulombic efficiency. This is in line with expectations as Mn^{2+} ions cannot be prevented from being reduced at the graphite surface, thus causing the prevention of additional side reactions is not possible.

The electrochemical data for cells with electrolyte additives with the co-addition of Mn is relatively independent of the corresponding gas evolution data. For example, from the gas evolution data, the VC+Mn cells show a substantial improvement over LFO+Mn cells and DTD+VC+Mn cells, however the electrochemical performances are all relatively similar with any differences being very minor. A possible explanation for this is that the sensitivity of equipment, duration of cycling, and sample size all play a role in this disconnect between gas evolution and electrochemical performance. The pressure measurements conducted with the modified Swagelok cell allows extremely sensitive measurements, where very small increases in gas volumes can be detected, therefore even small differences in gas evolution behaviour can be

observed. Conversely, the differences in electrochemical performance between the electrolytes is expected only to be visible in long term cycling protocols, therefore only very significant differences in electrochemical performance are visible within this project. Finally, each cell system tested only utilised 3 repeats, therefore if a single cell behaves slightly abnormally, it can impact the averaged results. If all three of these factors are addressed in future work, it may be possible to better correlate the electrochemical data with the gas evolution data.

5.6 Summary

In this chapter, the three additive candidates were added to LP57 electrolyte with the co-addition of Mn ions. These electrolytes were then used to cycle LFP vs graphite full Swagelok pressure cells to investigate the gas evolution and electrochemical behaviours for these systems. The goal was to determine the relative impact of the electrolyte additives and whether they were able to prevent the negative effects of Mn dissolution.

From this investigation, it was determined that all 3 additive candidates were able to reduce gas evolution in cells containing Mn dissolution. Where VC was determined to be the most effective at reducing gas evolution relative to Mn cells, so much so that it was indistinguishable from VC cells without Mn dissolution. DTD+VC and LFO produced comparable amounts of gas but both were also able to reduce the degree of gas evolution in comparison to Mn cells.

Gas evolution during cycle 1 is thought to be primarily determined by the reduction of EC and/or LEDC through contact with Mn^0, where the SEI formation reaction is crucial in reducing the amount of gas produced. From this, we can assume that the VC reduction products are superior to DTD and LFO reduction products with respect to forming a suitable SEI layer capable of passivating Mn^0. DTD and VC are thought to preferentially react at the graphite surface prior to EC, therefore preventing LEDC from being formed thus lowering the gas volume produced. Since LFO reacts at the same time as EC, LEDC cannot be prevented from being formed and would then come in contact with Mn^0.

Gas evolution during cycle 2+3 is likely to be determined by the passivating property of the SEI formed, where its ability to prevent further gassing reactions at the graphite surface or with Mn^0 would determine the gas volumes produced. From the data presented in this chapter, VC once again helps form the most robust SEI, with DTD+VC and LFO performing relatively similarly.

Cycle 1 electrochemical performance seems to be limited by the presence of Mn ions, where regardless of additive choice, the cycle 1 discharge capacity and efficiency remain lower than cells without Mn dissolution. Mn^{2+} is already on the surface of the graphite prior to the

formation of the SEI, which means that the additive cannot prevent contact between the Mn^{2+} and graphite surface, therefore all additives are unable to suppress Mn^{2+} reduction. This is why the cycle 1 discharge capacities are relatively similar across all the additives and with Mn cells. This is also reflected in the coulombic efficiency, where in cycle 1, cells containing Mn dissolution show lower efficiencies. As the reduction of Mn^{2+} is independent from the choice of additive and is not a gassing reaction, the cycle 1 electrochemical performance is not expected to have a good correlation with the gas evolution data, i.e. trends in discharge capacity do not match trends of gas evolution.

In cycle 2+3, the electrochemical performance starts to differ between electrolytes, with VC having the greatest discharge capacities, then LFO then DTD+VC. As the SEI is fully formed, the discharge capacity is determined by the quality of the SEI and how well it passivates side reactions. Therefore, the additive that is more effective at preventing side reactions also possesses the greatest discharge capacities, which is what is observed in the data. The coulombic efficiency in cycle 2+3 are relatively similar with only minor differences, indicating similar operations of lithium intercalation and extraction. The behaviour observed in the discharge capacities matches relatively well with what is observed with the gas evolution, for example VC prevents the most side reactions therefore has the most discharge capacity and the least gas evolution.

Finally, the DTD+VC additive combination was not as effective as VC despite possessing the same quantity of VC, where it produced more gas and had lower discharge capacities than VC. This indicates the presence of DTD can be considered detrimental to the effectiveness of VC. An explanation for this may be that firstly, the reduction of DTD causes irreversible capacity loss, and secondly, the reduction products of DTD may undergo further reactions that generate additional gas.

To summarise, this chapter successfully examined the impact of additives on cells with the co-addition Mn, where the relative performance of the 3 additive candidates were compared, in which VC was determined to be the most effective at reducing the detrimental impact of Mn dissolution.

Chapter 6 Project Conclusion and Further Work

This project has successfully shown the ability of simply modified Swagelok cells to conduct operando detection of gas evolution from lithium-ion batteries. Through an extensive process of numerous methodology optimisations, consistent and reliable electrochemical and pressure measurement results were able to be obtained. These optimisations were validated through the combination of half cells, full cells, and pressure adapted cells, all showing the data that correlates well with literature and expectations. Clearly, this easily accessible, highly adaptable method of gas analysis is a valuable technique.

Using these developed methods, graphite vs LFP cells with various electrolyte formulations were examined, where specific focus was given to analysing the effect of dissolved transition metal ions (nickel, manganese, and cobalt, which are produced in the degradation of NMC electrodes), the effect of electrolyte additives, and the combination of both.

From these experiments it was found that transition metal ions had a clear detrimental impact on both the gas evolution behaviour and the electrochemical performance of the cell, implying that the SEI layer is being disrupted by the presence of transition metal ions in the electrolyte. Manganese had the most pronounced impact, generating a dramatic increase in gas evolution compared to the nickel and cobalt, and was extremely detrimental to the electrochemical performance, markedly decreasing the first cycle coulombic efficiency. These results matched well with literature as the manganese is predicted to cause catalytic breakdown of the SEI. Interestingly, nickel and cobalt both exhibited decreased total gas evolution but did show signs of increased gas evolution during later cycling, revealing the instability of the SEI in the presence of all studied transition metal ions.

The three electrolyte additive candidates (VC, DTD/VC, and LFO) were then screened for their ability to prevent gas evolution both with and without the presence of manganese dissolution. VC was found to be considerably more effective than both DTD/VC and LFO at reducing gas evolution during cycling.

Interestingly, the addition of additives to both LP57 and LP57 with dissolved manganese did not have a significant effect on the electrochemical performance of the cells. This is attributable to the fact that the additives are not able to produce a strong and stable enough graphite SEI that is undisrupted by the presence of manganese ions. Even with additives, manganese ions produce a low coulombic efficiency that reveals that a large portion of the charge capacity is spent in an irreversible reaction (e.g., SEI formation).

The development of better additive formulations could be guided by the understanding of the reaction mechanism that can be achieved by combining various characterisation techniques, among which, the operando study of gas evolution, with techniques like those here presented, brings an important piece of information since key reactions of SEI formation involve the formation of gases.

Given more time, further work could have been done to supplement the data given in this project. Examples of this include:

- Testing DTD+Mn cells to see if DTD alone would have decreased the gas evolution caused by Mn ions.
- Longer cycling protocols in order to observe possible differences in electrochemical performance between the additives.
- Introducing Mn ions into the cell system after the formation of the SEI to investigate whether the detrimental impact would still be present.
- Using NMC811 vs graphite full cells to compare real transition metal dissolution and artificially adding transition metal salt.
- Utilise mass spectrometry techniques such as OEMS to elucidate the exact identity of the gas products.

Appendix

Temperature correction of operando pressure measurements

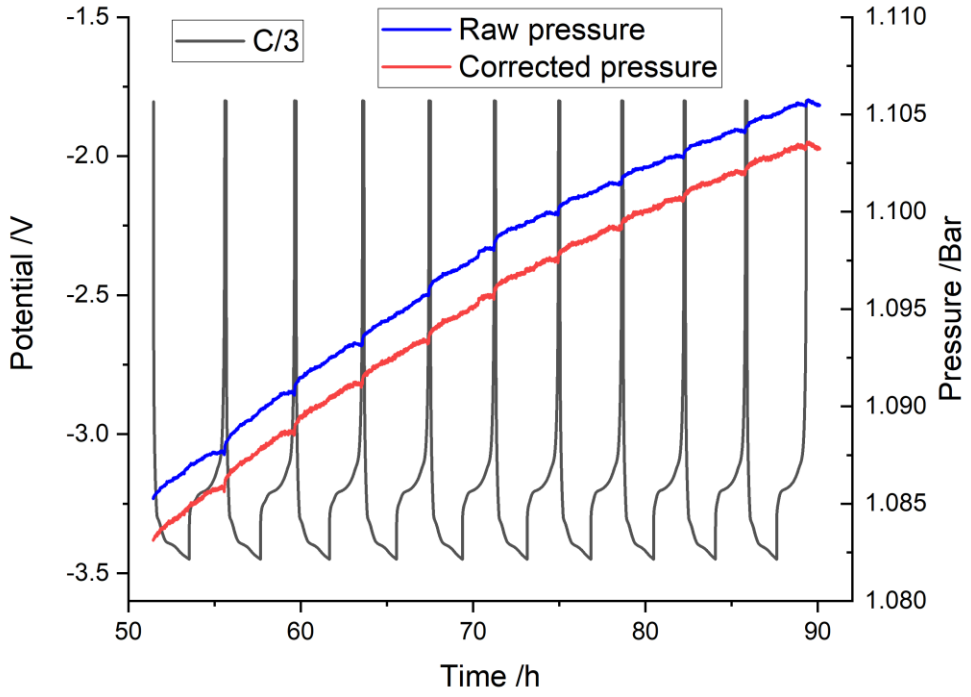

Figure 81 - Pressure measurement data corrected to account for temperature changes.

Figure 81 shows examples of pressure measurement data with and without temperature corrections, where the impact of temperature variations is quite minimal but should still be considered.

Headspace volume calculations

Firstly, the headspace volume set-up is arranged so that the reference transducer and the bottle are attached. Using this set-up, the volume of the reference transducer can be determined. This is done by using the following equation based on Boyles Law:

$$(P_{1\ Trans+Valve} * V_{Trans+Valve}) + (P_{1\ Bottle+tubing} * V_{Bottle+tubing}) = P_{System} * (V_{Bottle+tubing} + V_{Trans+valve})$$

Where $V_{trans+Valve}$ represents the unknown volume of the reference transducer.$P_{1\ Trans+Valve}$ represents known initial pressure of the reference transducer, $P_{1\ Bottle+Tubing}$ represents the known initial pressure of the bottle, $V_{Bottoe+Tubing}$ represents the known volume of the bottle, P_{system} represents the final pressure of the set-up. By following the steps outlined in section 2.2.6.1, it is

possible to gain the known values described above and calculate the volume of the reference transducer.

Once the reference transducer volume is known, the bottle is removed and replaced with another component of unknown volume. The equation is adjusted to give:

$$(P_{1\ Trans+Valve} * V_{Trans+Valve}) + (P_{1\ Unkown} * V_{Unkown}) = P_{System} * (V_{Unkown} + V_{Trans+valve})$$

Where the $P_{1\ Unkown}$ and V_{Uknown} represent the initial pressure of the unknown volume component and the volume of the unknown component respectively. Again, the above steps can be repeated to find the unknown volume of any component.

It is important to note that the unknown volume transducer and cell also include a tubing volume which can be deduced as the tubing measurements are known by measuring the physical dimensions.

Electrolyte formulation

All electrolyte was prepared on the day of use to avoid degradation of the electrolyte during long term storage. All electrolyte preparation was done in 38 ml aluminium bottles (95.5 %) that were thoroughly rinsed with ethanol to ensure minimal contaminants were present.

Transition metal salt electrolytes were prepared by dissolving the salts in the stock LP57 electrolyte, with the target concentration being 10 mM. The mass of transition metal and volume of LP57 electrolyte is shown here:

- Ni – 55.7 mg dissolved in 9 mL LP57.
- Mn – 55.37 mg dissolved in 9 ml LP57.
- Co – 55.73 mg dissolved in 9 ml LP57.

The transition metal salt would typically fully dissolve after 30 minutes.

Electrolyte formulations containing additives were prepared by again dissolving the additive solids in the stock LP57 electrolyte, except for 2% VC which was also available as a pre-prepared stock electrolyte formulation. The target concentrations for these electrolytes were 1% wt. To achieve this, ~ 0.1g of additive solids were first added to the aluminium bottle, LP57 (or 2% VC) electrolyte was then pipetted into the aluminium bottle until the total mass was ~10g. The LFO additive solids proved to be quite difficult to dissolve under normal conditions, therefore a stirrer plate was employed to dissolve the solid.

Additive and manganese electrolyte formulations simply combined the two protocols together, where the manganese dissolved electrolyte was first prepared in a separate aluminium bottle in excess, which would then be pipetted into the aluminium bottle containing the additive solid (again 2% VC being the exception).

List of References

1. M. Winter, B. Barnett and K. Xu, *Chem Rev*, 2018, **118**, 11433-11456.
2. N. S. Choi, Z. Chen, S. A. Freunberger, X. Ji, Y. K. Sun, K. Amine, G. Yushin, L. F. Nazar, J. Cho and P. G. Bruce, *Angew Chem Int Ed Engl*, 2012, **51**, 9994-10024.
3. N. Nitta, F. Wu, J. T. Lee and G. Yushin, *Materials Today*, 2015, **18**, 252-264.
4. C. Liu, Z. G. Neale and G. Cao, *Materials Today*, 2016, **19**, 109-123.
5. Y. Ding, R. Wang, L. Wang, K. Cheng, Z. Zhao, D. Mu and B. Wu, *Energy Procedia*, 2017, **105**, 2941-2952.
6. A. Guéguen, D. Streich, M. He, M. Mendez, F. F. Chesneau, P. Novák and E. J. Berg, *Journal of The Electrochemical Society*, 2016, **163**, A1095-A1100.
7. Y. P. Wu, E. Rahm and R. Holze, *Journal of Power Sources*, 2003, **114**, 228-236.
8. H. Cheng, J. G. Shapter, Y. Li and G. Gao, *Journal of Energy Chemistry*, 2021, **57**, 451-468.
9. Q. Wang, L. Jiang, Y. Yu and J. Sun, *Nano Energy*, 2019, **55**, 93-114.
10. A. M. Haregewoin, A. S. Wotango and B.-J. Hwang, *Energy Environ. Sci.*, 2016, **9**, 1955-1988.
11. J. A. Gilbert, I. A. Shkrob and D. P. Abraham, *Journal of The Electrochemical Society*, 2017, **164**, A389-A399.
12. A. K. Padhi, K. S. Nanjundaswamy and J. B. Goodenough, *Journal of The Electrochemical Society*, 1997, **144**, 1188-1194.
13. Z. Yang, Y. Dai, S. Wang and J. Yu, *Journal of Materials Chemistry A*, 2016, **4**, 18210-18222.
14. D. Y. W. Yu, K. Donoue, T. Inoue, M. Fujimoto and S. Fujitani, *Journal of The Electrochemical Society*, 2006, **153**.
15. A. Yamada, S. C. Chung and K. Hinokuma, *Journal of The Electrochemical Society*, 2001, **148**.
16. D. Doughty and E. P. Roth, *Electrochemical Society Interface*, 2012, **21**, 37-44.
17. B. Scrosati and J. Garche, *Journal of Power Sources*, 2010, **195**, 2419-2430.
18. J. M. Tarascon and M. Armand, *Nature*, 2001, **414**, 359-367.
19. D. Morgan, A. Van der Ven and G. Ceder, *Electrochemical and Solid-State Letters*, 2004, **7**.
20. S. Scaccia, M. Carewska, P. Wisniewski and P. P. Prosini, *Materials Research Bulletin*, 2003, **38**, 1155-1163.

21. G. X. Wang, L. Yang, S. L. Bewlay, Y. Chen, H. K. Liu and J. H. Ahn, *Journal of Power Sources*, 2005, **146**, 521-524.

22. V. Etacheri, R. Marom, R. Elazari, G. Salitra and D. Aurbach, *Energy & Environmental Science*, 2011, **4**.

23. B. Michalak, H. Sommer, D. Mannes, A. Kaestner, T. Brezesinski and J. Janek, *Sci Rep*, 2015, **5**, 15627.

24. A. Manthiram and J. B. Goodenough, *Nature Energy*, 2021, **6**, 323-323.

25. Y. Huang, *Interdisciplinary Materials*, 2022, **1**, 323-329.

26. T. Ohzuku and Y. Makimura, *Chemistry Letters*, 2001, **30**, 642-643.

27. F. Calvão, C. E. A. McDonald and M. Bolay, *The Extractive Industries and Society*, 2021, **8**.

28. B. K. Sovacool, *The Extractive Industries and Society*, 2019, **6**, 915-939.

29. H.-J. Noh, S. Youn, C. S. Yoon and Y.-K. Sun, *Journal of Power Sources*, 2013, **233**, 121-130.

30. I. Belharouak, Y. K. Sun, J. Liu and K. Amine, *Journal of Power Sources*, 2003, **123**, 247-252.

31. W.-S. Yoon, C. P. Grey, M. Balasubramanian, X.-Q. Yang, D. A. Fischer and J. McBreen, *Electrochemical and Solid-State Letters*, 2004, **7**.

32. B. Xu, D. Qian, Z. Wang and Y. S. Meng, *Materials Science and Engineering: R: Reports*, 2012, **73**, 51-65.

33. A. Manthiram, B. Song and W. Li, *Energy Storage Materials*, 2017, **6**, 125-139.

34. M. Li and J. Lu, *Science*, 2020, **367**, 979-980.

35. J. K. Ngala, N. A. Chernova, M. Ma, M. Mamak, P. Y. Zavalij and M. S. Whittingham, *Journal of Materials Chemistry*, 2004, **14**.

36. K. S. Lee, S. T. Myung, K. Amine, H. Yashiro and Y. K. Sun, *Journal of The Electrochemical Society*, 2007, **154**.

37. J. Xiao, N. A. Chernova and M. S. Whittingham, *Chemistry of Materials*, 2008, **20**, 7454-7464.

38. S. Liu, L. Xiong and C. He, *Journal of Power Sources*, 2014, **261**, 285-291.

39. N. L. P. Slowik, and C.-W. Hsu, 2020, DOI: 10.13140/RG.2.2.30613.35041.

40. Y. Xia, J. Zheng, C. Wang and M. Gu, *Nano Energy*, 2018, **49**, 434-452.

41. Q. Lin, W. Guan, J. Meng, W. Huang, X. Wei, Y. Zeng, J. Li and Z. Zhang, *Nano Energy*, 2018, **54**, 313-321.

42. R. Jung, M. Metzger, F. Maglia, C. Stinner and H. A. Gasteiger, *Journal of The Electrochemical Society*, 2017, **164**, A1361-A1377.

43. R. Jung, R. Morasch, P. Karayaylali, K. Phillips, F. Maglia, C. Stinner, Y. Shao-Horn and H. A. Gasteiger, *Journal of The Electrochemical Society*, 2018, **165**, A132-A141.

44. X. Ji and L. F. Nazar, *Journal of Materials Chemistry*, 2010, **20**.

45. P. G. Bruce, L. J. Hardwick and K. M. Abraham, *MRS Bulletin*, 2011, **36**, 506-512.

46. X. Zhang, A. Wang, X. Liu and J. Luo, *Acc Chem Res*, 2019, **52**, 3223-3232.

47. X. Q. Xu, X. B. Cheng, F. N. Jiang, S. J. Yang, D. Ren, P. Shi, H. Hsu, H. Yuan, J. Q. Huang, M. Ouyang and Q. Zhang, *SusMat*, 2022, **2**, 435-444.

48. X. Zhang, Y. Yang and Z. Zhou, *Chem Soc Rev*, 2020, **49**, 3040-3071.

49. S. J. An, J. Li, C. Daniel, D. Mohanty, S. Nagpure and D. L. Wood, *Carbon*, 2016, **105**, 52-76.

50. L. Wang, A. Menakath, F. Han, Y. Wang, P. Y. Zavalij, K. J. Gaskell, O. Borodin, D. Iuga, S. P. Brown, C. Wang, K. Xu and B. W. Eichhorn, *Nat Chem*, 2019, **11**, 789-796.

51. E. Peled and S. Menkin, *Journal of The Electrochemical Society*, 2017, **164**, A1703-A1719.

52. K. Xu, *Chem Rev*, 2004, **104**, 4303-4417.

53. S. K. Heiskanen, J. Kim and B. L. Lucht, *Joule*, 2019, **3**, 2322-2333.

54. B. Zhang, M. Metzger, S. Solchenbach, M. Payne, S. Meini, H. A. Gasteiger, A. Garsuch and B. L. Lucht, *The Journal of Physical Chemistry C*, 2015, **119**, 11337-11348.

55. M. Winter, *Zeitschrift für Physikalische Chemie*, 2009, **223**, 1395-1406.

56. A. J. Louli, L. D. Ellis and J. R. Dahn, *Joule*, 2019, **3**, 745-761.

57. C. Wang, C. Yang and Z. Zheng, *Advanced Science*, 2022, **9**.

58. W. Qi, J. G. Shapter, Q. Wu, T. Yin, G. Gao and D. Cui, *Journal of Materials Chemistry A*, 2017, **5**, 19521-19540.

59. F. Lepoivre, A. Grimaud, D. Larcher and J.-M. Tarascon, *Journal of The Electrochemical Society*, 2016, **163**, A923-A929.

60. S. E. Renfrew and B. D. McCloskey, *J Am Chem Soc*, 2017, **139**, 17853-17860.

61. A. A. Abd-El-Latif, C. J. Bondue, S. Ernst, M. Hegemann, J. K. Kaul, M. Khodayari, E. Mostafa, A. Stefanova and H. Baltruschat, *TrAC Trends in Analytical Chemistry*, 2015, **70**, 4-13.

62. E. Castel, E. J. Berg, M. El Kazzi, P. Novák and C. Villevieille, *Chemistry of Materials*, 2014, **26**, 5051-5057.

63. B. B. Berkes, A. Jozwiuk, H. Sommer, T. Brezesinski and J. Janek, *Electrochemistry Communications*, 2015, **60**, 64-69.

64. B. B. Berkes, A. Jozwiuk, M. Vracar, H. Sommer, T. Brezesinski and J. Janek, *Anal Chem*, 2015, **87**, 5878-5883.

65. A. Schiele, T. Hatsukade, B. B. Berkes, P. Hartmann, T. Brezesinski and J. Janek, *Anal Chem*, 2017, **89**, 8122-8128.

66. K. H. Lee, E. H. Song, J. Y. Lee, B. H. Jung and H. S. Lim, *Journal of Power Sources*, 2004, **132**, 201-205.

67. C. P. Aiken, J. Xia, D. Y. Wang, D. A. Stevens, S. Trussler and J. R. Dahn, *Journal of The Electrochemical Society*, 2014, **161**, A1548-A1554.

68. N. Ryall and N. Garcia-Araez, *Journal of The Electrochemical Society*, 2020, **167**.

69. V. Murray, D. S. Hall and J. R. Dahn, *Journal of The Electrochemical Society*, 2019, **166**, A329-A333.

70. B. D. McCloskey, D. S. Bethune, R. M. Shelby, G. Girishkumar and A. C. Luntz, *J Phys Chem Lett*, 2011, **2**, 1161-1166.

71. M. He, E. Castel, A. Laumann, G. Nuspl, P. Novák and E. J. Berg, *Journal of The Electrochemical Society*, 2015, **162**, A870-A876.

72. R. Bernhard, M. Metzger and H. A. Gasteiger, *Journal of The Electrochemical Society*, 2015, **162**, A1984-A1989.

73. M. Metzger, B. Strehle, S. Solchenbach and H. A. Gasteiger, *Journal of The Electrochemical Society*, 2016, **163**, A798-A809.

74. R. Petibon, L. M. Rotermund and J. R. Dahn, *Journal of Power Sources*, 2015, **287**, 184-195.

75. K. Xu and A. von Cresce, *Journal of Materials Chemistry*, 2011, **21**.

76. R. Marom, O. Haik, D. Aurbach and I. C. Halalay, *Journal of The Electrochemical Society*, 2010, **157**.

77. B. Rowden and N. Garcia-Araez, *Energy Reports*, 2020, **6**, 10-18.

78. R. Mogi, M. Inaba, Y. Iriyama, T. Abe and Z. Ogumi, *Journal of Power Sources*, 2003, **119-121**, 597-603.

79. I. Buchberger, S. Seidlmayer, A. Pokharel, M. Piana, J. Hattendorff, P. Kudejova, R. Gilles and H. A. Gasteiger, *Journal of The Electrochemical Society*, 2015, **162**, A2737-A2746.

80. R. Jung, F. Linsenmann, R. Thomas, J. Wandt, S. Solchenbach, F. Maglia, C. Stinner, M. Tromp and H. A. Gasteiger, *Journal of The Electrochemical Society*, 2019, **166**, A378-A389.

81. C. Delacourt, A. Kwong, X. Liu, R. Qiao, W. L. Yang, P. Lu, S. J. Harris and V. Srinivasan, *Journal of The Electrochemical Society*, 2013, **160**, A1099-A1107.

82. C. Zhan, J. Lu, A. Jeremy Kropf, T. Wu, A. N. Jansen, Y. K. Sun, X. Qiu and K. Amine, *Nat Commun*, 2013, **4**, 2437.

83. S. Solchenbach, G. Hong, A. T. S. Freiberg, R. Jung and H. A. Gasteiger, *Journal of The Electrochemical Society*, 2018, **165**, A3304-A3312.

84. C. Wang, L. Xing, J. Vatamanu, Z. Chen, G. Lan, W. Li and K. Xu, *Nat Commun*, 2019, **10**, 3423.

85. J. Wandt, A. Freiberg, R. Thomas, Y. Gorlin, A. Siebel, R. Jung, H. A. Gasteiger and M. Tromp, *Journal of Materials Chemistry A*, 2016, **4**, 18300-18305.

86. S. S. Zhang, *Journal of Power Sources*, 2006, **162**, 1379-1394.

87. D. H. Doughty, E. P. Roth, C. C. Crafts, G. Nagasubramanian, G. Henriksen and K. Amine, *Journal of Power Sources*, 2005, **146**, 116-120.

88. K. Abe, in *Electrolytes for Lithium and Lithium-Ion Batteries*, 2014, DOI: 10.1007/978-1-4939-0302-3_3, ch. Chapter 3, pp. 167-207.

89. Y. Wang, S. Nakamura, K. Tasaki and P. B. Balbuena, *J Am Chem Soc*, 2002, **124**, 4408-4421.

90. J. C. Burns, R. Petibon, K. J. Nelson, N. N. Sinha, A. Kassam, B. M. Way and J. R. Dahn, *Journal of The Electrochemical Society*, 2013, **160**, A1668-A1674.

91. D. Aurbach, K. Gamolsky, B. Markovsky, Y. Gofer, M. Schmidt and U. Heider, *Electrochimica Acta*, 2002, **47**, 1423-1439.

92. J. C. Burns, N. N. Sinha, D. J. Coyle, G. Jain, C. M. VanElzen, W. M. Lamanna, A. Xiao, E. Scott, J. P. Gardner and J. R. Dahn, *Journal of The Electrochemical Society*, 2011, **159**, A85-A90.

93. D. Xiong, J. C. Burns, A. J. Smith, N. Sinha and J. R. Dahn, *Journal of The Electrochemical Society*, 2011, **158**.

94. L. El Ouatani, R. Dedryvère, C. Siret, P. Biensan, S. Reynaud, P. Iratçabal and D. Gonbeau, *Journal of The Electrochemical Society*, 2009, **156**.

95. L. Chen, K. Wang, X. Xie and J. Xie, *Journal of Power Sources*, 2007, **174**, 538-543.

96. B. Mosallanejad, S. Sadeghi Malek, M. Ershadi, H. Sharifi, A. Ahmadi Daryakenari, F. Boorboor Ajdari and S. Ramakrishna, *Journal of Electroanalytical Chemistry*, 2022, **909**.

97. J. C. Burns, G. Jain, A. J. Smith, K. W. Eberman, E. Scott, J. P. Gardner and J. R. Dahn, *Journal of The Electrochemical Society*, 2011, **158**.

98. D. Y. Wang, N. N. Sinha, R. Petibon, J. C. Burns and J. R. Dahn, *Journal of Power Sources*, 2014, **251**, 311-318.

99. J. Xia, N. N. Sinha, L. P. Chen and J. R. Dahn, *Journal of The Electrochemical Society*, 2013, **161**, A264-A274.

100. X. Li, Z. Yin, X. Li and C. Wang, *Ionics*, 2013, **20**, 795-801.

101. A. Sano and S. Maruyama, *Journal of Power Sources*, 2009, **192**, 714-718.

102. L. Madec, J. Xia, R. Petibon, K. J. Nelson, J.-P. Sun, I. G. Hill and J. R. Dahn, *The Journal of Physical Chemistry C*, 2014, **118**, 29608-29622.

103. H. Zhao, S. Hu, Y. Fan, Q. Wang, J. Li, M. Yuan, X. Ma, J. Wang, H. Shao and Y. Deng, *Energy Storage Materials*, 2024, **65**.

104. T. Yang, W. Wang, S. Li, J. Lu, W. Fan, X. Zuo and J. Nan, *Journal of Power Sources*, 2020, **470**.

105. A. M. Andersson, D. P. Abraham, R. Haasch, S. MacLaren, J. Liu and K. Amine, *Journal of The Electrochemical Society*, 2002, **149**.

106. A. Wang, L. Wang, H. Liang, Y. Song, Y. He, Y. Wu, D. Ren, B. Zhang and X. He, *Advanced Functional Materials*, 2023, **33**.

107. G. Yang, J. Shi, C. Shen, S. Wang, L. Xia, H. Hu, H. Luo, Y. Xia and Z. Liu, *RSC Advances*, 2017, **7**, 26052-26059.

108. Q. Q. Liu, L. Ma, C. Y. Du and J. R. Dahn, *Electrochimica Acta*, 2018, **263**, 237-248.

109. L. Ma, L. Ellis, S. L. Glazier, X. Ma, Q. Liu, J. Li and J. R. Dahn, *Journal of The Electrochemical Society*, 2018, **165**, A891-A899.

110. C. Fongy, A. C. Gaillot, S. Jouanneau, D. Guyomard and B. Lestriez, *Journal of The Electrochemical Society*, 2010, **157**.

111. S. J. An, J. Li, Z. Du, C. Daniel and D. L. Wood, *Journal of Power Sources*, 2017, **342**, 846-852.

112. N. N. Sinha, J. C. Burns, R. J. Sanderson and J. Dahn, *Journal of The Electrochemical Society*, 2011, **158**.

113. Y.-Y. Wang, X.-Q. Zhang, M.-Y. Zhou and J.-Q. Huang, *Nano Research Energy*, 2023, **2**.

114. L. Guo, D. B. Thornton, M. A. Koronfel, I. E. L. Stephens and M. P. Ryan, *Journal of Physics: Energy*, 2021, **3**.

115. C. Fear, D. Juarez-Robles, J. A. Jeevarajan and P. P. Mukherjee, *Journal of The Electrochemical Society*, 2018, **165**, A1639-A1647.

116. J. E. Harlow, X. Ma, J. Li, E. Logan, Y. Liu, N. Zhang, L. Ma, S. L. Glazier, M. M. E. Cormier, M. Genovese, S. Buteau, A. Cameron, J. E. Stark and J. R. Dahn, *Journal of The Electrochemical Society*, 2019, **166**, A3031-A3044.

117. A. Eldesoky, M. Bauer, S. Azam, E. Zsoldos, W. Song, R. Weber, S. Hy, M. B. Johnson, M. Metzger and J. R. Dahn, *Journal of The Electrochemical Society*, 2021, **168**.

118. Z. Ruff, C. Xu and C. P. Grey, *Journal of The Electrochemical Society*, 2021, **168**.

119. E. Bjorklund, C. Xu, W. M. Dose, C. G. Sole, P. K. Thakur, T. L. Lee, M. F. L. De Volder, C. P. Grey and R. S. Weatherup, *Chem Mater*, 2022, **34**, 2034-2048.

120. W. M. Dose, I. Temprano, J. P. Allen, E. Bjorklund, C. A. O'Keefe, W. Li, B. L. Mehdi, R. S. Weatherup, M. F. L. De Volder and C. P. Grey, *ACS Appl Mater Interfaces*, 2022, **14**, 13206-13222.

121. H. Xu, Z. Li, T. Liu, C. Han, C. Guo, H. Zhao, Q. Li, J. Lu, K. Amine and X. Qiu, *Angew Chem Int Ed Engl*, 2022, **61**, e202202894.

122. S. Klein, P. Bärmann, O. Fromm, K. Borzutzki, J. Reiter, Q. Fan, M. Winter, T. Placke and J. Kasnatscheew, *Journal of Materials Chemistry A*, 2021, **9**, 7546-7555.

123. V. Meunier, M. L. De Souza, M. Morcrette and A. Grimaud, *Journal of The Electrochemical Society*, 2022, **169**.

124. H. Shin, Y. K. Lee and W. Lu, *Journal of Power Sources*, 2022, **528**.

125. A. Nazari, R. Emaeeli, S. Reza Hashemi, H. Aliniagerdroudbari and S. Farhad, *ASME Power Proceedings*, 2018, **51401**, Article 277477.

126. J. Kim, H. Ma, H. Cha, H. Lee, J. Sung, M. Seo, P. Oh, M. Park and J. Cho, *Energy & Environmental Science*, 2018, **11**, 1449-1459.

127. J. Li and A. Manthiram, *Advanced Energy Materials*, 2019, **9**.

128. Y. K. Lee, *Journal of Power Sources*, 2021, **484**.

129. H. Shin, J. Park, A. M. Sastry and W. Lu, *Journal of Power Sources*, 2015, **284**, 416-427.

130. T. Joshi, K. Eom, G. Yushin and T. F. Fuller, *Journal of The Electrochemical Society*, 2014, **161**, A1915-A1921.

131. S. Komaba, N. Kumagai and Y. Kataoka, *Electrochimica Acta*, 2002, **47**, 1229-1239.

132. H. Ota, Y. Sakata, A. Inoue and S. Yamaguchi, *Journal of The Electrochemical Society*, 2004, **151**.

133. R. Lundström, N. Gogoi, T. Melin and E. J. Berg, *The Journal of Physical Chemistry C*, 2024, **128**, 8147-8153.

134. D. S. Hall, J. P. Allen, S. L. Glazier, L. D. Ellis, L. Ma, J. M. Peters, I. G. Hill and J. R. Dahn, *Journal of The Electrochemical Society*, 2017, **164**, A3445-A3453.

135. P. G. Kitz, M. J. Lacey, P. Novák and E. J. Berg, *Journal of Power Sources*, 2020, **477**.

136. K.-E. Kim, J. Y. Jang, I. Park, M.-H. Woo, M.-H. Jeong, W. C. Shin, M. Ue and N.-S. Choi, *Electrochemistry Communications*, 2015, **61**, 121-124.

137. Y. Qian, S. Hu, X. Zou, Z. Deng, Y. Xu, Z. Cao, Y. Kang, Y. Deng, Q. Shi, K. Xu and Y. Deng, *Energy Storage Materials*, 2019, **20**, 208-215.

138. E. R. Logan, H. Hebecker, X. Ma, J. Quinn, Y. HyeJeong, S. Kumakura, J. Paulsen and J. R. Dahn, *Journal of The Electrochemical Society*, 2020, **167**.